HHS Public Access

Author manuscript

Biochim Biophys Acta. Author manuscript; available in PMC 2016 June 01.

Published in final edited form as:

Biochim Biophys Acta. 2015 June ; 1853(6): 1370–1394. doi:10.1016/j.bbamcr.2015.01.025.

Advanced Paramagnetic Resonance Spectroscopies of Iron-Sulfur Proteins: Electron Nuclear Double Resonance (ENDOR) and Electron Spin Echo Envelope Modulation (ESEEM)

George E. Cutsail III[‡], **Joshua Telser**[§], and **Brian M. Hoffman**[‡,*]

[‡]Department of Chemistry, Northwestern University, 2145 Sheridan Road, Evanston, IL, 60208 USA

Abstract

The advanced electron paramagnetic resonance (EPR) techniques, electron nuclear double resonance (ENDOR) and electron spin echo envelope modulation (ESEEM) spectroscopies, provide unique insights into the structure, coordination chemistry, and biochemical mechanism of Nature's widely distributed iron-sulfur cluster (FeS) proteins. This review describes the ENDOR and ESEEM techniques and then provides a series of case studies on their application to a wide variety of FeS proteins including ferredoxins, nitrogenase, and radical SAM enzymes.

Introduction

Iron-sulfur proteins share an important history with paramagnetic resonance techniques. Indeed, FeS proteins were first identified by Helmut Beinert with the use of electron paramagnetic resonance (EPR) spectroscopy. [1, 2] [3, 4] This review will assume some familiarity with the basics of EPR, and will thus focus on the advanced EPR techniques, electron nuclear double resonance (ENDOR) and electron spin echo envelope modulation (ESEEM) spectroscopies, and their contributions towards extending our understanding of the roles played by FeS proteins. These spectroscopic techniques were invented roughly concurrently with the discovery of FeS proteins (i.e., late 1950's – early 1960's), [3–6] and ENDOR was applied to two-iron ferredoxins (2Fe-Fds) not long thereafter. [7, 8]

This review first provides an overview of the multiple forms in which ENDOR and ESEEM spectroscopies are currently practiced, and then describes in detail specific cases where these techniques have yielded important insights into the structure and biochemical action of iron-sulfur proteins. The emphasis is on more recent work; however, as appropriate we will detail studies that, beginning in the 1980's, initiated the application of these techniques to FeS proteins, and that provide the foundation for recent studies.

[*]bmh@northwestern.edu.

[§]Permanent Address: Department of Biological, Chemical and Physical Sciences, Roosevelt University, Chicago, IL 60605, USA

The techniques of ENDOR and ESEEM spectroscopy aid in the understanding of various characteristics of metal ions and FeS clusters in biology such as: electronic and magnetic properties, enzyme mechanism, structure (coordination geometry, valence, and ligand identification with or without substrate/product/inhibitors) and protein dynamics. EPR spectra of metalloproteins are often too broad to resolve the interactions that contain the desired biochemical and physical information. In these cases, ENDOR and ESEEM spectroscopies provide this information at significantly higher resolution than from EPR alone.

The interactions of a metalloprotein's unpaired electron spin(s) (S) and a nuclear spin (I), are measured by their hyperfine couplings, denoted A. A large number of biochemically relevant nuclei have non-zero nuclear spin ($I > 0$) with examples arising from amino acid residues, cofactors, or substrates/inhibitors including naturally abundant isotopes such as: ^{1}H, ^{14}N, ^{19}F, ^{31}P, and those requiring isotopic enrichment such as: ^{2}H (D), ^{13}C, ^{15}N, ^{17}O, and ^{33}S. Many metallic elements have non-zero spin isotopes of which ^{57}Fe (I = 1/2, 2.2% abundance) is the most relevant here. For larger hyperfine couplings, or interactions where the intrinsic linewidth of the EPR spectrum is narrow, these electron-nuclear interactions can be directly observed in the EPR spectrum. An example is the observation of hyperfine coupling from ^{63,65}Cu (I = 3/2, together 100% abundance) in Type II copper centers, and even in this case, the coupling is resolved only in the $g_{\|}$ region. More often than not, and in particular in the case of iron-sulfur proteins, the EPR linewidth of metalloprotein centers is sufficiently broad that small but important electron-nuclear hyperfine couplings are unresolved. To determine these hyperfine couplings and identify the nuclei of origin requires ENDOR and ESEEM spectroscopies, which will be described in the next section. The hyperfine information gained may identify nuclei within the coordination sphere, characterize bonding structure, determine bond order, and estimate electron-nuclear spin distances. These complementary advanced EPR techniques each are capable of resolving hyperfine couplings; whereas ENDOR spectroscopy is able to detect a wide a range of hyperfine couplings, from as little as ~10^{-1} MHz up to > 10^{2} MHz, ESEEM techniques are typically limited to smaller hyperfine values, A < 10 MHz. Each technique can identify the nuclei present with ENDOR having the advantage of being broad-banded, but ESEEM spectroscopy has the advantage of being able to 'count' the number of equivalent nuclei (as in NMR).

Techniques

EPR

The electronic paramagnetic resonance (EPR) spectrum provides the first information associated with the Fe-S center: its electronic spin state ($S \geq 1/2$, with S = 1/2 and 3/2 being the most amenable to study), iron d orbital configuration, FeS cluster oxidation state, and general molecular framework of the FeS cluster is established, and described in more detail elsewhere. [9–11] This information arises from the associated electron energy levels and their interaction with an externally applied magnetic field. In recording an EPR spectrum, the magnetic field, **B**, is swept while a microwave field of fixed energy ($E = h\nu$; ν = frequency; typically ~9 GHz (X-band) or 35 GHz (Q-band)), is applied, and resonant

transitions occur at field positions characteristic to the electronic structure, which are described in terms of a **g** tensor (or matrix). In general, the three components of the **g** tensor (typically, g_x, g_y, g_z, or, if one is reluctant to choose a geometrical designation, g_1, g_2, g_3, or g_{min}, g_{mid}, g_{max}) depend on the electronic structure, electron spin interactions, and the relative orientation of the molecule within the magnetic field. The individual *g* values that make up the **g** tensor may be viewed as deviations of the unpaired electron(s) from that of a 'true' free electron without any other interactions, which is g_e = 2.00232…. These deviations result from the orbital aspects of the unpaired electron(s), which interact with the spin aspects of the electron. As the number of electrons in the paramagnetic center increases, these spin-orbital interactions increase, and are thus more significant for Fe-S clusters (*i.e.*, paramagnetic 3d ions) than for, say, organic radical species (paramagnetic 2s, 2p molecules).

ENDOR

The paramagnetic centers of Fe-S clusters in Nature create unique spectroscopic probes for both electronic and structural coordination characterization by EPR (discussed in detail elsewhere in this special issue) and electron nuclear double resonance (ENDOR) spectroscopies. [4, 12–16] In principle, any system with non-zero electron spin, $S > 0$, not only Kramers (*S* half-integer) but also non-Kramers states (*S* integer), can be EPR active and give advanced paramagnetic resonance responses. However, we focus here on what is perhaps the most common spin state in FeS proteins, and which is by far the most amenable to study by EPR and advanced techniques, namely $S = 1/2$. This unpaired electron spin of the Fe-S center paired with either its own iron nuclear spin(s), with spins of nuclei within the coordination sphere and of substrates/products/inhibitors allow one to generate a wealth of information for the Fe-S center. First, the electronic information of the iron ions may be determined through ENDOR hyperfine measurements of the ^{57}Fe nuclei. [17–20] This sole magnetically active isotope of iron is present in only 2.15% natural abundance, and thus, isotopic enrichment in ^{57}Fe is usually desirable. [1, 2] Secondly, one may answer the question of what atoms, either through natural abundance or isotopic labeling, are within the first and second coordination sphere of the Fe-S cluster. These include isotopes such as ^{1}H, ^{13}C, ^{15}N, ^{19}F, ^{31}P, ^{57}Fe (all $I = 1/2$), ^{2}H, ^{14}N (both $I = 1$), ^{33}S ($I = 3/2$), and ^{17}O, ^{95,97}Mo (all $I = 5/2$).

While the EPR spectrum provides us with much preliminary information, including an orientation frame with which to view our molecule, much of the information desired, namely the electron-nuclear hyperfine and quadrupole interactions are small in energy and thus unresolved within the broad linewidth of the FeS cluster's EPR spectrum. ENDOR spectroscopy, by virtue of the higher resolution and lower energy scale of the NMR experiment, directly measures these interactions governed by the nuclear spin Hamiltonian, H_N:

$$H_N = \underbrace{g_N \beta_N I \cdot \mathbf{B}}_{\text{nuclear Zeeman}} + \underbrace{S \cdot \mathbf{A} \cdot I}_{\text{hyperfine}} + \underbrace{I \cdot \mathbf{P} \cdot I}_{\text{quadrupole}} \quad (1)$$

where β_N is the Bohr magneton, which is a constant for all nuclei, g_N is the nuclear *g* value, unique to each isotope, *I* is the isotope's nuclear spin, and **B** is the magnetic field. The

orientation dependent hyperfine interaction, **A**, depends on the electronic spin, *S*, and the nuclear spin of the isotope being measured, *I*. For a given *S*, the quantized spin angular momentum levels are: $M_S = [-S, (-S+1), \ldots, 0, \ldots, (S-1), S]$, with an analogous situation for *I* ($M_I = [-I, (-I+1), \ldots, 0, \ldots, (I-1), I]$. Allowed EPR transitions involve a change in electronic spin level: $\Delta M_S = \pm 1$, $\Delta M_I = 0$, while ENDOR (i.e., NMR) transitions are: $\Delta M_S = 0$, $\Delta M_I = \pm 1$. Figure 1 outlines the allowed EPR and ENDOR transitions of an $S = 1/2$, $I = 1/2$ system, where solid lines *a* and *b* satisfy the $\Delta M_S = \pm 1$, $\Delta M_I = 0$ selection rule for EPR, while solid lines *c* and *d* satisfy the selection rules $\Delta M_S = 0$, $\Delta M_I = \pm 1$ for ENDOR spectroscopy. Lines *e* and *f* are $\Delta M_S = \pm 1$, $\Delta M_I = 1$ forbidden EPR transitions.

ENDOR spectra are collected at static magnetic fields, each field defining a single EPR resonance among all possible, fixing the nuclear Zeeman portion of the nuclear Hamiltonian. Nuclei at this fixed magnetic field will resonate at a Larmor frequency, ν_N, determined by: $h\nu_N = g_N\beta_N\mathbf{B}$, which scales with magnetic field, **B**. An unpaired electron spin creates an large internal field that perturbs any nearby magnetically active nuclear spins, much like the significantly smaller internal field interactions between nuclear spins created in traditional NMR experiments measured by their chemical shift. Just as a 500 MHz ^{1}H NMR spectrum measures the deviation of protons from their Larmor frequency, $\nu_N(^1\text{H}) = 500$ MHz, at a magnetic field of 120 kG (12 T), ENDOR will measure proton interactions with large electronic spins which increases the internal magnetic field felt by the surrounding nuclear spins. [16] For ENDOR, this internal field is measured as a hyperfine coupling interaction tensor, **A**. The observed ENDOR transitions may appear as Larmor centered, ν_N, split by the hyperfine coupling, *A*, when the internal field is smaller than the external field: $\nu_N > A/2$ – or – when the internal field is larger than external field $\nu_N < A/2$, the transitions with appear centered at half of the hyperfine coupling and split by $2\nu_N$. These two possibilities are given by the following (first-order) equation:

$$\nu_{\pm} = \left|\nu_n \pm \frac{A}{2}\right| \quad (2)$$

The right panel of Figure 1 explores the ‘weak’ Larmor-centered and ‘strong’ *A*/2-centered hyperfine coupling patterns for an $S = 1/2$, $I = 1/2$ spin system – the simplest ENDOR active spin system.

The hyperfine coupling (hfc), *A*, interaction for a particular nucleus contains a wealth of information. This is because hfc is related to electron spin delocalization onto a given nucleus, and hence, bonding information, geometry, and structural information. The matrix, **A**, can thus be decomposed into two components: $\mathbf{A} = A_{\text{loc}} + T$. The first component, A_{loc}, is the local contribution to the observed hyperfine coupling and it depends on the nuclear properties of the nucleus observed. Various interactions of this nucleus with the electron spin are ‘contained’ within A_{loc}, including covalent bonding interactions and isotropic hyperfine coupling arising in general from electron spin density in *s*-orbitals at the nucleus. Ideally, the collection of A_{loc} of all nuclei for a metallocenter yields a complete composition of the covalent bonding network electron spin in the first coordination sphere. For the atoms involved in the ‘covalent’ bonded network, in-depth analysis of A_{loc} can yield rich inorganic information, such as: *i*) valency of the metal ions, [21] *ii*) covalency of the ligands [22] and

iii) the coordination geometry of the metallocenter. The second term, *T*, garners the non-local, dipolar coupling information of atoms near the metallocenter, covalently bonded or not. Dipolar couplings allow for distance estimates between the nuclear and electron spin, and other geometric constraints such as angles and coordinates. [14, 23]

Atoms of nuclear spin $I \geq 1$ possess a non-spherical atomic nucleus and are referred to as quadrupolar nuclei. In contrast to nuclei with $I = 1/2$, for which the $M_I = \pm 1/2$ values are equal in energy (degenerate) in the absence of an external magnetic field, regardless of their electronic environment, nuclei with, e.g., $I = 1$ (as in ^{14}N) have $M_I = 0, \pm 1$ levels, which may have differing nuclear energy magnitudes, even in the absence of external magnetic field. [9] All that is required is an internal *electric* field gradient, which can result from an unequal charge distribution around the quadrupolar nucleus, which could be the consequence of an imbalance of p orbital valence electrons about the nucleus. [24] This 'charge distribution' is measured and observed as an additional splitting of the ENDOR transitions described above. In this case of quadrupolar splitting, denoted as *P* (or sometimes *Q*), each ENDOR peak is further split by the quadrupole moment into 2*I* lines dictated by the following (first-order) equation:

$$\nu_{\pm}(M_I) = \left| \nu_N \pm \frac{A}{2} \pm \frac{3P(2M_I - 1)}{2} \right| \quad (3)$$

applicable when the quadrupole splitting is much smaller than the hyperfine. [9] For an $S = 1/2$, $I = 1$ system, the same ENDOR selection rules, $\Delta M_S = 0$, $\Delta M_I = \pm 1$, still apply, however, the possible splitting pattern is now more complex, as seen in Figure 2. For an axial quadrupole tensor, $\mathbf{P} = [-P_x/2, -P_y/2, P_z]$, the allowed ENDOR transitions are as follows: *e* and *f* of the $M_S = +1/2$ manifold, and *d* and *g* of the $M_S = -1/2$ manifold. The hyperfine can once again be in a 'weak' or 'strong' coupling regime as described earlier, however, for each, the observed quadrupole splitting is the same, 3*P*, Figure 2. The quadrupole coupling information thus obtained can be extremely powerful in determining bonding information and bond order, critical for distinguishing e.g., sp^2 imidazole nitrogens from other protein nitrogenous species. [24, 25]

Many of the Fe-S protein samples studied by EPR and ENDOR spectroscopy are in a frozen solution and therefore are a random distribution of all possible orientations in the magnetic or lab frame, hence the probability distribution of the field to align with any given orientation is equivalent. As each of the hyperfine, **A**, and quadrupole, **P**, tensors are orientation dependent, the deconvolution and mapping of complete tensors onto the electronic **g** tensor is performed through analysis of 2D field-frequency ENDOR spectra. [16, 26–29] ENDOR spectra collected at the magnetic field edges of the rhombic EPR spectrum typically resemble a 'single-crystal-like' position, therefore one is observing only a single map of the **A** and **P** tensors along a single axis of the **g** tensor. ENDOR spectra of the 2D field-frequency between these field edges represent a mathematical subset of orientations of hyperfine and quadrupole. Through the correspondence of magnetic field (*g* values) and angular section, the absolute values and orientations of each **A** and **P** may be mapped onto the relative molecular frame provided by the **g** tensor.

ENDOR spectra may be collected with 'continuous-wave' (CW) microwave instrumentation by holding the magnetic field static while sweeping an applied radiofrequency (RF). The classic CW method for ENDOR acquisition involves field modulation and phase-sensitive detection with an RF sweep, and has superior sensitivity to the currently more popular pulsed ENDOR techniques. [14] However, pulsed ENDOR techniques frequently are able to give better-resolved ENDOR line shapes, and to resolve weaker hyperfine couplings. [30, 31]

Pulsed ENDOR techniques consist of microwave pulse sequences with the incorporation of RF pulses. There are two fundamental pulsed ENDOR techniques, named after their inventors, Mims [6] and Davies, [32] respectively. The Mims ENDOR pulse sequence is based on the three-pulse (each 90° pulse is represented by π/2 in the sequence) stimulated electron spin echo (ESE) sequence: π/2 −τ − π/2 − *T* − π/2 − τ − *echo* (Figure 3). To achieve ENDOR, an RF pulse is applied during time *T*. The Mims sequence can be used for large couplings but is most useful for resolving small hyperfine couplings, generally less than 4 MHz. Its sensitivity is a joint function of the hyperfine coupling being interrogated, *A*, and the interval, τ.

$$\mathrm{ENDOR} \propto (1 - \cos(\pi A \tau))/2 \quad (4)$$

The Mims ENDOR sequence thus is affected by 'blind spots' (i.e., points at which the S/N is essentially zero), when $A = n/\tau$, where $n = 0, 1, \ldots$, integer. [33]

The presence of blind spots can sometimes be advantageous as they can allow suppression of signals with specific hyperfine coupling, potentially simplifying spectra. [33] The first two 'non-selective' microwave pulses of the stimulated pulse sequence are responsible for the holes created in Mims ENDOR as the π/2 − τ − π/2 sequence creates a 'polarization grating' within the inhomogeneous EPR line where the ENDOR is detected. [34]

For larger hyperfine couplings, generally greater than 4 MHz, the Davies ENDOR sequence, π − *T* − π/2 − τ − π − τ − *echo*, where the RF is applied once again at time *T*, is employed (Figure 3). [32] The preparation microwave π pulse is first applied to 'flip' the electron spin and then the RF pulse is applied during time *T* to then excite and mix nuclear transitions that match the RF pulse frequency. A Hahn echo sequence (i.e., the originally invented ESE sequence; described in more detail in the ESEEM section below): π/2 − τ − π − τ − *echo*, is then applied and directly detects the NMR polarization of the EPR transition created by the RF pulse, yielding the ENDOR measurement. In contrast to the Mims pulse sequence; the Davies ENDOR detection is described by the function, [33, 35]

$$\mathrm{ENDOR}(A(\mathrm{MHz}), t_p(\mu\mathrm{s})) \propto \frac{1.4(t_p)}{0.7^2 + (At_p)^2} \quad (5)$$

where t_p is the separation in time between the first two pulse. For the Davies ENDOR response, the 'hole in the middle,' appears as *A* goes to zero, but otherwise the ENDOR response does not have 'blind spots'.

These two pulse sequences have set the foundation for development of additional techniques. The Remote-Echo Mims (ReMims) 'four-pulse' sequence (Figure 3) developed by Doan allows for the collection of distortion-free ENDOR spectra of nuclei with hyperfine coupling greater than typically obtainable by the Mims pulse sequence, and is useful to bridge the gap in hyperfine coupling between traditional Mims and Davies ENDOR methods. [36]

Another pulsed ENDOR 'trick' for deconvolution of ENDOR spectra and to ease the process of assignments of overlapping peaks is the employment of TRIPLE spectroscopy (where TRIPLE is not an acronym for anything and is sometimes referred to as *double ENDOR*). [34, 37] As it is considered a 'pump – probe' technique, the TRIPLE technique may be able to resolve and confirm nuclei hyperfine coupling assignments. A second 'pump' RF pulse of a constant frequency is added before the variable 'probe' RF pulse of the ENDOR pulse sequence. When the pump frequency matches a ENDOR transition of a ν_+ transition of a given nuclei, for example, the irradiation will cause an intensity change of the ν_- transition, correlating the ν_-/ν_+ pair for a single hyperfine coupling.

Relative signs of a hyperfine tensor for individual nuclei can sometimes be found through the analysis and simulation of 2D field-frequency ENDOR patterns, when a through-space dipole interaction gives a reference sign (e.g. [38, 39]). Likewise TRIPLE can sometimes be used to determine relative hyperfine signs of multiple nuclei in a system through the so-called implicit TRIPLE effect. [40] First established on the low-spin Fe^{III} ($S = 1/2$) center of the non-heme enzyme nitrile hydratase, [40] the implicit TRIPLE effect has been extended to FeS clusters. [41] Whereas the determination of relative ^{57}Fe hyperfine coupling signs has been well established in ENDOR, recently multi-pulse sequences have been developed to obtain absolute sign information, starting with the work of Bennebroek and Schmidt. [42,43, 44] Most recently, a robust and reliable multi-pulse sequence has been developed by Doan, the Pulsed ENDOR Saturation Recovery (PESTRE) protocol, which determines absolute signs of hyperfine couplings in conjunction with corresponding ENDOR measurements, described below. [45, 46] No longer does the assignment of absolute signs of ^{57}Fe hyperfine couplings of FeS clusters depend solely on high field Mössbauer measurements. [20]

ESEEM

Electron Spin Echo Envelope Modulation Spectroscopy (ESEEM) [47–49] is a microwave-only pulsed technique that has the ability to resolve small hyperfine and quadrupole couplings that may not be resolved using other advanced techniques such as ENDOR spectroscopy, and has the experimental advantage of simplicity as no separate RF equipment is required, unlike for ENDOR. [50] ESEEM, as the name implies, employs the detection of a spin echo by a two pulse (primary echo), $\pi/2 - \tau - \pi - \tau - echo$, or a three pulse (stimulated echo) sequence, described later. The basic two pulse sequence, often employed for 'electron-spin-echo-detected' EPR spectra, will create what is also often referred to as a Hahn spin echo. [51] After the $\pi/2$ pulse flips electron spins into the orthogonal plane of the magnetic field vector, the electron spins dephase at a relaxation rate, T_{1e}, characteristic of the electron spin system. For transition metal ions at temperatures below 10 K, typical T_{1e} times are on the order of 10 μs. The electron spin is allowed to 'dephase' during a time τ

before it is flipped again by π. The electron spin has memory and will begin to 'rephase' much like the previous 'dephasing' but now in the opposite axis direction so as to develop an echo which appears at the same time interval for the original dephasing, τ. By varying τ, the 'dephasing' behavior of the electron spin is detected.

As in ENDOR, the electron and nuclear Zeeman effects dominate the spectrum and will dominate the electron spin echo's intensity. However, electron-nuclear hyperfine and quadrupole interactions also contribute to the echo intensity, and they are better exploited by varying τ over a series of applied pulse sequences. When τ is varied, the echo intensity of each pulse sequence of a given step in time, τ, is measured, forming a time-domain spectrum. Primarily, the phase memory of the system is observed as exponential decay of the echo intensity as τ increases. Of central interest, periodic modulation(s) of the electron spin echo by nuclear interactions appear within the time domain spectrum. This modulation created by nuclear hyperfine and/or quadrupole transitions is of central interest in the ESEEM experiment, therefore deeper modulation is desired for increased S/N. The relaxation decay of the echo is subtracted from the time domain spectrum followed by subsequent processing (windowing, zero filling, etc. – the same "tricks" as used in FT-NMR) before the final Fourier transform that yields a frequency domain spectrum for easier observation of the hyperfine and quadrupole couplings.

ESEEM spectroscopy has the advantage over ENDOR spectroscopy of being able to 'count' similar nuclei of similar hyperfine and quadrupole parameters by the nuclear modulation depth. [25] In contrast, ENDOR signal intensities are difficult to correlate with number of nuclei. For example, this quantitative ability of ESEEM has been extremely useful in the determining the number of imidazole ligands of a given metallocenter. [25]

The transitions observed in ESEEM vary slightly from those of ENDOR. As ENDOR spectroscopy follows its selection rules more rigorously, ESEEM techniques exploit both allowed and 'semi-forbidden' transitions. [34] For $S = 1/2$, $I = 1/2$ cases, maximum modulation depth within the ESEEM time-domain spectrum is obtained when the microwave energy 'matches' the Hamiltonian energy (Eq 1), taking into specific consideration the second and third terms, the hyperfine and quadrupole interactions, respectively. ESEEM transitions observed for $I = 1/2$ nuclei are a result of only the anisotropic portion of the hyperfine tensor (primarily T; see definition for **A** given above). Many anisotropic nuclei that may be of interest, e.g., ^{1}H couplings of metal-bound $^{1}H_{x}O$ species, have very broad lines, so that the modulation is frequently lost within the dead time of the instrument, making ESEEM of $I = 1/2$ systems often difficult. [50] However, ^{15}N ($I = 1/2$) isotopic labeling can be useful for analyzing weaker ^{14}N couplings, because the ^{15}N ESEEM can yield a more direct estimate of the dipolar contribution, which can then be used in interpreting the ^{14}N ESEEM data, which contain isotropic and quadrupole couplings, as discussed next.

For $S = 1/2$, $I = 1$ cases, frequently histidine ^{14}N systems at X-band (~ 9.5 GHz), the quadrupole term now plays a significant role. [25] The off-diagonal matrix elements introduced by the rhombic quadrupole tensor allows for more significant mixing of the quantum states, and semi-forbidden $\Delta M_I = \pm 2$, double quantum, transitions to occur, such as

h, *i*, *j*, and *k* in Figure 2. The semi-forbidden transitions in Figure 2 are combination differences between the allowed EPR and ENDOR transitions, creating unique observable transitions for the ESEEM experiment. In the opposite view, when both allowed EPR and semi-forbidden ESEEM transitions are excited in the ESEEM experiment, their frequencies will beat against each other and result in single transitions at the ENDOR frequencies, for example *i* (EPR) – *h* (semi-forbidden) = *f* (ENDOR).

Three-pulse ESEEM, which has the sequence: $\pi/2 - \tau - \pi/2 - \Delta T - \pi/2 - \tau - echo$ (Figure 3), is often simpler to analyze as it contains only the principal ENDOR (NMR) frequencies and semi-forbidden transitions, while lacking the sum and difference peaks of transitions observed in a two-pulse ESEEM experiment. While greater signal intensity is achieved with the three-pulse ESEEM sequence as compared to the two-pulse ESEEM sequence for disordered (frozen solution) systems, the main disadvantage of three-pulse ESEEM is the inclusion of 'blind-spots' as a function of τ. These holes are caused by the same 'polarization grating', $\pi/2 - \tau - \pi/2$, of the stimulated echo as seen in the Mims ENDOR spectroscopy, however, the hole pattern has no dependence on *A*, only on τ, therefore, multiple three pulse ESEEM spectra of varying τ should be collected to ensure proper assignments.

HYSCORE

The development of three-pulse ESEEM techniques led to its extension into a two-dimensional form, [52] much as what had occurred earlier in NMR spectroscopy. This 2D ESEEM is referred to as hyperfine sublevel correlation (HYSCORE) spectroscopy, and is produced by the addition of a 'mixing pulse' to create a four-pulse ESEEM sequence. [53] While 3-pulse ESEEM works well for some disordered systems, it often loses much of the fast decaying modulation amplitude, quicker than the electron spin decay. This is much more of a problem for larger coupling with significant hyperfine anisotropy. The nuclear modulation is often lost before collection begins because of instrument dead time, or only a small amount is resolved before it decays. The addition of a fourth π pulse to the three pulse sequence alleviates this problem by transferring nuclear spin coherence from one manifold to the other and prolonging the modulation decay time. The addition of this π pulse between the second and third $\pi/2$ pulses of the three-pulse sequence, $\pi/2 - \tau - \pi/2 - T_1 - \pi - T_2 - \pi/2 - \tau - echo$ (Figure 3), creates two separate 'evolution' periods before and after the π pulse, termed T_1 and T_2. The π pulse takes the nuclear coherence developed in the $M_S = \pm 1/2$ electron manifold during the first evolution period and mixes it between the electron spin manifolds. The nuclear spin coherence now evolves in the $M_S = -/+ 1/2$ electron spin manifold, and a nuclear coherence transfer echo is created at $T_1 = T_2$. The nuclear coherence transfer echo is most easily observed in the frequency domain spectrum along the diagonal of $T_1 = T_2$. The last $\pi/2$ pulse transfers the nuclear coherences to electron coherences for detection as an electron spin echo. The key aspect of the HYSCORE experiment is that the final electron spin echo produced has been modulated by the nuclear spins, similar to the ESEEM experiment, however, the mixing pulse helps extend the electron spin relaxation decay time, improving sensitivity relative to 2D three-pulse ESEEM spectroscopy of disordered (frozen solution) systems.

The typical four-pulse ESEEM experiment is done in a 2D fashion (HYSCORE) where T_1 and T_2 are incremented independently of each other and the final product therefore correlates the nuclear frequencies with the mixing of the electron spin manifolds. The 2D time domain spectrum is processed in a similar fashion as described earlier for ESEEM and 2D Fourier transform results in four quadrants, where, as with ENDOR, two coupling regimes are possible, either a strong ($A > \nu_n$) or weak coupling ($\nu_n > A$) regime; however, all peaks are not observed in a single quadrant. For 'weak' couplings of powder samples, peaks are once again Larmor centered perpendicular to the frequency diagonal in the first (+,+) and third (−,−) quadrants. For stronger couplings, cross peaks appear in the second and fourth quadrants, occasionally labeled as (+,−) and (−,+), respectively. This process allows for the readout and interpretation of multiple nuclei in a single spectrum that may have been unmanageable in a single ESEEM experiment. The powder pattern responses do not easily translate to complete hyperfine and quadrupole tensors. Complete line shape analysis and simulations at multiple magnetic field positions is the only true way to fully resolve **A** and **P** tensor values and their respective orientation to **g**, reviewed extensively elsewhere. [50, 54–57]

HYSCORE is most useful to resolve broad hyperfine lines that three-pulse ESEEM often fails to detect. The ability of HYSCORE to detect large anisotropic couplings of $I = 1/2$ nuclei such as ^{1}H and ^{13}C is a result of the added π mixing pulse, as these couplings are no longer lost through destructive interference which occurs in the three pulse experiment. Of course, HYSCORE still retains 'blind-spots' with τ time dependencies; therefore careful experimental and/or simulation considerations must be made.

Advanced EPR techniques applied to non-Kramers (integer-spin) systems

The above description of ENDOR, ESEEM, and HYSCORE techniques uses as examples the Kramers, $S = 1/2$, state the most common and spectrally rewarding of the possible spin states of FeS clusters. However, FeS clusters can also be found in higher spin states. Resting state nitrogenase has $S = 3/2$, and has been extensively studied by ENDOR as described elsewhere in this review and in other reviews. [58–60] For completeness it is useful to note that ENDOR and ESEEM can be productively applied to favorable integer spin states, primarily $S \geq 2$, which can be found in 3Fe-red clusters, $[Fe_3S_4]^0$, and has recently been identified in catalytic turnover states of nitrogenase. [60–62] It has been known for many years that integer-spin (non-Kramers) states having $S \geq 2$ with negative zero-field splitting parameter D (so that the spin ground doublet is $|S, \pm M_S\rangle = \pm S$) exhibit EPR spectra, generally at low fields. [63, 64] More recently, it was shown that ENDOR and ESEEM of such EPR signals can be highly informative. [65–67]

Advanced EPR studies of FeS clusters in iron-sulfur and related proteins—

This section describes advanced EPR studies that focus on the FeS cluster itself, using as probes primarily the Fe ions themselves (enriched in ^{57}Fe), but also ^{1}H nuclei located on coordinated thiolates that directly provide information on their nearby Fe ion. As discussed subsequently the inorganic sulfides can also be studied upon enrichment in ^{33}S ($I = 3/2$, 0.75% natural abundance). In the case of heterometallic clusters, such as in nitrogenase FeMo-co, other nuclei can be studied, such as ^{95}Mo ($I = 5/2$, 15.9% natural abundance, *and*

enriched) and the central ion of FeMo-co, now identified as a carbide, due in part to enrichment in ^{13}C. [68–70]

^{57}Fe ENDOR

It is of interest to note that ^{57}Fe studies of FeS clusters not only initiated the use of ENDOR in characterizing metalloenzymes, [7] but were the motivation [71] for the development of the theory and methodology for determining hyperfine interactions tensors through the simulation of 2D field-frequency patterns of ENDOR spectra collected across the EPR envelope of the center under study, [16, 26, 27] as well as the development of the most robust method for determining hyperfine signs, PESTRE. [45]

2Fe-Ferredoxins

The exchange coupling of the two iron spins, S = 2 Fe^{II} and S = 5/2 Fe^{III} ions, in an EPR observable reduced $[2Fe2S]^+$ cluster result in either a ferromagnetically [72] coupled ground state, which yields a total spin, S = 9/2, or an antiferromagnetically coupled ground state, which gives S = 1/2. [73] The observed **g** tensor for the antiferromagnetically coupled state is given by

$$\mathbf{g}=\frac{7}{3}\mathbf{g}_{\mathrm{III}}-\frac{4}{3}\mathbf{g}_{\mathrm{II}} \quad (6)$$

where $\mathbf{g}_{\mathrm{III}}$ and $\mathbf{g}_{\mathrm{II}}$ are the individual **g** tensors of the ferric and ferrous centers, respectively. The low-spin S = 1/2 ground state is more commonly observed for [2Fe2S] clusters. Figure 4 presents Q-band (35 GHz) EPR spectra of three, representative FeS proteins with S = 1/2 ground states, including $[2Fe2S]^+$ cluster from *Aquifex aeolicus* Fd1. The spectra were all recorded at 2 K under “rapid passage” conditions, [74] so that the experimental spectrum appears as an absorption line shape. In addition, for each protein, a numerical derivative spectrum is also provided, which thus has the first derivative line shape of an EPR spectrum recorded under “slow passage” conditions, as is the case for typically reported spectra. Each format has advantages and disadvantages. The absorption lineshape is better for observation of broad lines and gives a better idea as to the actual amount of signal. The first derivative lineshape is better for observation of narrow lines. This can easily be seen in Figure 4B, wherein the spectral signature of a small amount of adventitious Mn(II), which appears as a sextet due to hyperfine coupling to ^{55}Mn (I = 5/2, 100%) is greatly accentuated in the digital derivative presentation, even though the Mn(II) is actually present in very low concentration, as shown by the experimental, absorption lineshape, which is dominated by the much broader $[4Fe4S]^+$ EPR signal. and an oxidized 2Fe-Fd $[2Fe2S]^+$ (Figure 4A), which has a significantly rhombic signal with g values straddling 2.0 (**g** = [2.05, 1.95, 1.89], g_{iso} = 1.96).

Either of the S = 1/2 or 9/2 paramagnetic states for $[2Fe2S]^+$ clusters are amenable to ENDOR characterization of both the ^{57}Fe centers and of coordinated ligands and other nearby molecules. Both ^{57}Fe ENDOR and magnetic Mössbauer spectroscopies may characterize the electronic structure of the iron ions of a given FeS center. [64, 75] Each technique has distinct advantages and disadvantages. As discussed elsewhere, [13, 14, 20,

76] Mössbauer is able to detect all Fe sites in a given sample, while ENDOR observes only those interacting with unpaired electron(s). This fact alone can lead to complementary information being provided by the two techniques. For example, Mössbauer is able to characterize the diamagnetic, reduced $[2Fe2S]^0$ $S = 0$ ground state, inaccessible by ENDOR, as well as other paramagnetic, or integer-spin systems ($S = 1, 2, \ldots$), which are more difficult, but not impossible (*vide supra*) to study by EPR and ENDOR. However, Mössbauer may be overwhelmed when multiple FeS clusters reside within a protein, severely convoluting a spectrum. ENDOR, in contrast, has the advantage of being 'blind' to diamagnetic species and can select among paramagnetic FeS clusters whose EPR envelopes do not overlap. Indeed, the spin state selection of ENDOR plays a critical role in the study of some complex FeS systems. A more subtle distinction is that Mössbauer can determine ^{57}Fe quadrupole splitting that is unattainable through ENDOR spectroscopy as this information arises from the nuclear excited state of ^{57}Fe ($I = 3/2$), accessed by the γ-ray energy employed by Mössbauer. [77] Traditionally, an advantage of Mössbauer is that it allowed determination of the sign of hyperfine couplings, along with their magnitudes, while such sign information was not obtainable from ENDOR. However, as discussed above, newly developed ENDOR protocols for determining absolute hyperfine signs [20, 45, 46] have "leveled the playing field" between the two techniques in this regard.

The **g** tensor for [2Fe2S] clusters may be used to classify clusters into families and determine electronic characteristics [20], however it is the ^{57}Fe hyperfine couplings that provide the deepest insight into their electronic structure and ENDOR spectroscopy has the added advantage of being able to map the **g** tensor orientation onto the molecular frame.

The $[2Fe2S]^+$ clusters from *Aquifex aeolicus* (*Aae*) ferredoxins (Fd1, Fd5, and Fd5) are cysteine coordinated and belong to a $g_{iso} = 1.96$ subclass of 2Fe ferredoxins. [20] By grouping [2Fe2S] proteins into subclasses of related electronic structure, various ligand-field energies may be determined from EPR parameters as shown recently for Fd1, Fd4, and Fd5 from *Aae*. Such $[2Fe2S]^+$ clusters exhibit fairly isotropic Fe^{III} coupling, while the hyperfine coupling of the Fe^{II} ion is very anisotropic with its strongest hyperfine coupling along g_1. The constituent Fe^{III} ion in a $[2Fe2S]^+$ cluster is relatively insensitive to its coordination environment, which is expected due to the spherical electron distribution of its high-spin d^5 (half-filled) electronic configuration. [18, 20, 78, 79] In contrast, the ligand field of the Fe^{II} ion is very sensitive to its coordination environment as a result of the unsymmetrical electron distribution of its high-spin d^6 configuration. The differences in the average of g values for different classes of [2Fe2S] clusters reflect the environment of the Fe^{II} site. [80] The dictates the ligand field energy d^6, Fe^{II} ion controls the rhombic splitting of the cluster **g** tensor, which is proportional to the mixing of pure $d(z^2)(^5A_1)$ (axial compression) or $d(x^2 - y^2)(^5B_1)$ (axial elongation) states of Fe^{II} for D_{2d} symmetry. For $g_{iso} = 1.96$ class of [2Fe2S] proteins, the various ligand-field energies of the Fe^{II} ion in its ground state may be determined from fitting the g values to a diagonalized energy matrix for two pure z^2 and x^2-y^2 states (diagonal terms) and the amount of rhombic crystal field mixing (off-diagonal terms) due to a rhombic crystal-field distortion ($D_{2h} \rightarrow C_{2v}$). Thus, the plot of rhombic splitting versus canonical g values yields the ligand-field parameters for a given class of

[2Fe2S] clusters. Figure 5 presents a solution to Eqs. 6 and 8 with ligand-field parameters given in the figure caption.

$$\tan 2\eta = -\frac{2\varepsilon_{\mathrm{mix}}}{\varepsilon_{z^2} - \varepsilon_{x^2-y^2}} \quad (7)$$

$$\begin{aligned} g_{\mathrm{II}x}(\eta) &= g_e - \frac{8\lambda}{\Delta E_{yz}}\sin^2\left(\eta + \frac{\pi}{3}\right) = g_e + \Delta g_{\mathrm{II}x}(\eta), \\ g_{\mathrm{II}y}(\eta) &= g_e - \frac{8\lambda}{\Delta E_{xz}}\sin^2\left(\eta - \frac{\pi}{3}\right) = g_e + \Delta g_{\mathrm{II}y}(\eta), \\ g_{\mathrm{II}z}(\eta) &= g_e - \frac{8\lambda}{\Delta E_{xy}}\sin^2\eta = g_e + \Delta g_{\mathrm{II}z}(\eta). \end{aligned} \quad (8)$$

The amount of orbital mixing is proportional to the rhombic splitting of **g**, $\Delta g_{\perp} = g_3 - g_2$, and is a function of the fictitious angle 2η (Figure 5). [20]

As the EPR spectrum is influenced by the symmetry of the FeS cluster, the same is obviously true for the iron hyperfine couplings. High precision ENDOR of the ^{57}Fe hfc of Fd1, Fd4, and Fd5 from *Aae* reveal isotropic Fe^{III} hyperfine couplings, matching those previously established by Mössbauer spectroscopy. The Fe^{II} hyperfine couplings are vastly different for Fd1 and Fd5 which happen to be remarkably similar in structure. Further investigation of the slight differences in the structural, electronic, hyperfine properties of characterized ferredoxin proteins needs to be done to achieve a more general understanding of the mixed valent [2Fe–2S] cluster. Understanding of the simplest FeS cluster serves as a building block for understanding higher nuclearity FeS clusters.

4Fe-Ferredoxin Overview

Various oxidation states of [4Fe4S] clusters are observed, ranging from the 3+ state seen in oxidized high potential iron-sulfur protein (HiPIP-ox), to 2+, 1+, and 0. Only 3+, $S = 1/2$, and 1+, $S = 1/2$ or $S = 3/2$, cluster oxidation states possess paramagnetic ground spin states and are amenable to typical advanced EPR spectroscopies. [81–83] The other, diamagnetic 2+, $S = 0$, and 0, $S = 4$, oxidation states may be observed through Mössbauer spectroscopy. The ground spin states are most conveniently explained by antiferromagnetic coupling of [2Fe2S] cluster pairs (the so-called 2-2 model), ($[2Fe2S]^{2+}$, $S = 5$; $[2Fe2S]^{+}$, $S = 9/2$; $[2Fe2S]^{0}$, $S = 4$) and the Fe^{II} $S = 2$ and/or Fe^{III} $S = 5/2$ ion(s). The common $[4Fe4S]^{3+}$ $S = 1/2$ state is the result of an $[2Fe2S]^{+}$ ($Fe^{2.5}$-$Fe^{2.5}$) $S = 9/2$ pair antiferromagnetically coupled with two Fe^{III} $S = 5/2$ ions. The two electron reduced $[4Fe4S]^{+}$ is composed also of an $[2Fe2S]^{+}$ ($Fe^{2.5}$-$Fe^{2.5}$) $S = 9/2$ pair however it is antiferromagnetically coupled with two Fe^{II} $S = 2$ ions. [18, 84] Examples of an oxidized HiPIP $[4Fe4S]^{3+}$ and a reduced $[4Fe4S]^{+}$ are exhibited in Figure 4. The oxidized HiPIP $[4Fe4S]^{3+}$ exhibits an axial, narrow linewidth signal, with *g* values above 2.0 ($g_{\|} = 2.14$, $g_{\perp} = 2.04$, $g_{iso} = 2.07$) and the reduced 4Fe-Fe $[4Fe4S]^{+}$ has a broader linewidth, slightly rhombic signal with *g* values straddling 2.0 (**g** = [2.07, 1.94, 1. 91], $g_{iso} = 1.97$). It should be noted, as can be seen by comparison of Figures 4A and 4C, that it is essentially impossible to distinguish solely by EPR between 4Fe-red

and 2Fe-red centers. As described below, the specific nature of the coupling can be variable and more intricate than indicated here.

4Fe-Ferredoxin Models

The synthesis of small molecule model compounds of the active site center of ferredoxins and other FeS cluster species was a great achievement of inorganic chemistry that has been extensively reviewed elsewhere. [85–87] Of relevance here is the use made of several synthetic ferredoxins for detailed EPR and ENDOR studies by Gloux, Lamotte, Mouesca, and co-workers in Grenoble. [18, 88–93] The synthetically accessible cluster, $[Fe_4S_4(SR)_4]^{2-}$ (where R = Ph (-C_6H_5), Bz (-$CH_2C_6H_5$)) is diamagnetic and corresponds to the 4Fe-ox (or HiPIP-red) protein cluster forms. These workers were able to generate EPR active forms of the synthetic clusters by low-temperature γ-irradiation of single crystals, this process, which has also been used extensively with metalloproteins in frozen solution, [94] [95] [96] generates free electrons which can then reduce the FeS center to generate $[Fe_4S_4(SR)_4]^{3-}$, the analog to the 4Fe-red cluster. In addition, oxidized clusters, $[Fe_4S_4(SR)_4]^{1-}$, can also be concurrently generated, analogous to the HiPIP-ox form. The different EPR signatures of these species allowed their deconvolution in single-crystal EPR spectra. [90, 92, 97] In these synthetic clusters, the only ENDOR active nucleus is ^{1}H, with the methylene hydrogen atoms of the benzylthiolato (or related) ligands serving as models for the β-H atoms of cysteinyl ligands in FeS clusters. [89, 93] Nevertheless, ^{1}H ENDOR has provided a wealth of information on the electronic structure of these 4Fe4S model compounds. All eight ^{1}H hyperfine tensors were fully determined for $[Fe_4S_4(SCH_2C_6D_5)_4]^{1-}$, wherein the benzene ring deuteration assisted in simplifying the ^{1}H X-band ENDOR spectra. The results on hydrogen dipolar coupling and spin distribution within the cluster could be related to those from paramagnetic NMR and allowed a proposal to be made as to the specific spin coupling state, namely $|S_{\text{mixed-valence}}, S_{\text{ferric}}, S_{\text{total}}\rangle = |7/2, 3, 1/2\rangle$, as opposed to $|9/2, 4, 1/2\rangle$, [89] (note that in some 2Fe-Fds, $S_{\text{mixed-valence}} = S_{\text{ferric}} + S_{\text{ferrous}} = 5/2 + 2 = 9/2$, and $0 \le S_{\text{ferric}} \le 10$ (+ 5/2 + 5/2)). The same parent compound, in the reduced form generated by γ-irradiation was later studied by Q-band ^{1}H ENDOR. [98] It was possible to determine the full hyperfine tensors of all eight benzyl methylene hydrogen atoms, plus three more tensors from ^{1}H nuclei on adjacent molecules. Analogously to the earlier study, the spin distribution within the 4Fe-red model cluster was determined, including the spin projection onto each Fe ion, which is crucial for understanding hyperfine coupling to bound substrate in enzymatic FeS clusters. In this cluster, the spin coupling ground state was determined to be $|S_{34}, S_{134}, S_{\text{total}}\rangle = |4, 2, 1/2\rangle$, using the so-called '3-1' scheme, wherein the three formally ferrous ions (Fe^{II}_1, Fe^{II}_3, and Fe^{II}_4) are coupled to give first S_{34} ($0 \le S_{34} \le 4$; here 4) and then $S_{134} = S_{34} - S_2 = 4 - 2$ in this case, which is then antiferromagnetically coupled to the ferric ion: $S_{\text{total}} = S_{134} - S_2 = |4 - 5/2| = 1/2$. An alternate, and widely used coupling scheme (*vide supra*), although considered less physically sound for $[Fe_4S_4]^+$ by Moriaud *et al*. [105], is the '2-2' scheme which is analogous to that used above for $[Fe_4S_4]^{3+}$, namely, $S_{\text{mixed-valence}} = S_{12} = 9/2$ (or lower) and $S_{\text{ferrous}} = S_{34} = 4$ (or lower), with $S_{\text{total}} = S_{12} - S_{34} = |9/2 - 4| = 1/2$. Using the 2-2 model, the $[Fe_4S_4(SCH_2C_6D_5)_4]^{3-}$, is best represented as $|S_{\text{mixed-valence}}, S_{\text{ferrous}}, S_{\text{total}}\rangle = |S_{12}, S_{34}, S_{\text{total}}\rangle = |7/2/, 3, 1/2\rangle$; the spin coupling scheme analogous to that for the HiPIP-ox model cluster.

The Grenoble workers were also able to prepare $[^{57}Fe_4S_4(SCH_2C_6H_5)_4]^{2-}$, and made ^{57}Fe X-band ENDOR measurements of γ-irradiated species that allowed the determination of the full ^{57}Fe hyperfine coupling tensors of all four Fe sites in a $[Fe_4S_4]^{3+}$ cluster. [88] Subsequently, thanks to the advantages provided by Q-band ENDOR, namely shifting the ^{1}H ENDOR resonances far from those of ^{57}Fe as well as providing greater *g* value dispersion, Moriaud et al. [105] were able to study successfully a 4Fe-red model, $[^{57}Fe_4S_4(SCH_2C_6H_5)_4]^{3-}$, and determined the full ^{57}Fe hyperfine tensors in this cluster as well. [88] These landmark experimental results on model compounds have been crucial in subsequent theoretical studies of FeS cluster electronic structure, [91] and have been extremely helpful in providing benchmarks for understanding biological FeS clusters for which such high precision single-crystal ENDOR studies are not feasible.

Heterodisulfide reductase

During the final methane forming step by methanogenic archaea, a mixed disulfide of coenzyme M (CoM, mercaptoethane sulfonate) and coenzyme B (CoB, 7-mercaptoheptanoyl-L-threonine phosphate), CoM-S-S-CoB, is formed. [99] Methanogens from *Methanothermobacter marburgensis* do not contain cytochromes and must reduce CoM-S-S-CoB by other means, as the regeneration of the individual CoM-SH and CoB-SH thiols is needed for continued methane formation. [100] The exothermic reduction of this disulfide is performed by heterodisulfide reductase (Hdr), a part of the proposed hydrogenase-heterodisulfide reductase complex, MvhADG-HdrABC. [99] Hdr is composed of three subunits, HdrA containing a FAD bonding motif as found from primary sequence data and four [4Fe4S] cluster binding sites, based again on the primary sequence. HdrC contains two additional [4Fe4S] binding sites. The subunit of disulfide reduction, HdrB, contains a bound [4Fe4S] cluster in a C-terminal CCG motif ($CX_{31–39}CCGX_{35–36}CXXC$) and a bound zinc to the N-terminal CCG domain. [101]

HdrABC in the presence of only CoM (CoM-HdrABC) exhibits an EPR signal below 50 K from a paramagnetic $S = 1/2$ species which has *g* values similar to those of the oxidized form of HdrB. This $S = 1/2$ signal of CoM-HdrABC is lost upon the addition and reaction of CoB-SH, which reduces the [4Fe4S] cluster. The reduction of the FeS cluster observed by EPR, hyperfine broadenings of the EPR signal from ^{57}Fe enriched enzyme [102] and ^{33}S-labeled CoM-SH, [103] combined with variable-temperature magnetic circular dichroism (VT-MCD) experiments, [104] led to the suggested $[4Fe4S]^{3+}$ formal charge of the CoM substrate bound cluster in the CoM-HdrABC complex.

Previous 9 and 95 (W-band) GHz ENDOR of CoM-Hdr exhibited unusually isotropic ^{57}Fe couplings of four distinct iron responses for an [4Fe4S] cluster, with respective signs implied from polarized patterns of the W-band ENDOR responses. [105] The cluster is observed only under oxidizing conditions, with two iron hyperfine couplings resembling an ($Fe^{2.5+}$–$Fe^{2.5+}$) pair, [18] indicating the cluster is $[4Fe4S]^{3+}$, however, this is not supported by the observed average of Hdr-CoM *g* values, $g_{iso} < 2.0$, which contrasts to what is observed for well-known $[4Fe4S]^{3+}$ clusters, such as oxidized HiPIPs, which have *g* values > 2.0 [92] (see Figure 4).

The 34 GHz ^{57}Fe ENDOR spectra of CoM-HdrABC and HdrB in an oxidized form ($HdrB_{oxid}$) (Figure 6), unambiguously resolve all four iron sites of the [4Fe4S] cluster [106] and provide improved resolution over the earlier W-band results. [105] Using the hyperfine sign results previously found for CoM-HdrABC from 95 GHz ENDOR spectroscopy, [105] a mixed valence pair, $Fe^{2.5+}$–$Fe^{2.5+}$, with isotropic coupling of approximately −30 MHz is observed, along with a ferric pair, Fe^{III}–Fe^{III}, with coupling of approximately +20 MHz, which together are typical for an $[4Fe4S]^{3+}$ $S = 1/2$ cluster and have been observed previously for other HiPIP proteins [18] and are almost identical to that of the oxidized HiPIP $[4Fe4S]^{3+}$ cluster in *Chromatium vinosum* measured by Mössbauer spectroscopy. [107]

These ^{57}Fe hyperfine couplings are in the ‘strong coupling’ regime where the ENDOR response at each microwave frequency is centered at $A/2$. The increased separation of the ENDOR $\nu_{+/-}$ doublets at Q-band frequency and correspondingly higher magnetic fields yielded higher resolution of the four iron hyperfine couplings compared to the situation at X-band measurements, Figure 6.

Hydrogenase

The hydrogenase enzymes consist of three classes, separated by their metal cofactor active sites: the mononuclear iron [Fe]-, diiron [FeFe]-, and the [NiFe]-hydrogenases. [108] The active site of the [FeFe] enzymes is shown in Figure 7. Both [FeFe] and [NiFe]-hydrogenases contain multiple FeS clusters for electron delivery to their active sites, however the [FeFe]-hydrogenase uniquely contains an [4Fe4S] cluster that is completely cysteinyl coordinated and is bound to the proximal iron (Fe_p) of the active site diiron center (H-cluster) through a cysteine thiolate bridge conserved throughout the [FeFe] hydrogenases. [109, 110] The proximal (to the [4Fe4S] cluster) iron, Fe_p, and the distal iron, Fe_d, each contain CO and CN^- exogenous ligands, and are bridged by a CO and two thiolate bridges from a dithiolate moiety, unique to [FeFe]-hydrogenases. [108]

While the advanced EPR spectroscopic characterization of hydrogenase has provided an abundance of information including ligand unpaired spin density, [111] thiolate bridge atom identification, [112–115], cluster assembly, [113, 116–120] [121] and model complexes, [122–124] all extensively reviewed elsewhere, [108, 116, 125] we will briefly show the particular example of the ^{57}Fe ENDOR and HYSCORE work of the [4Fe4S] cluster of the [FeFe]-hydrogenase. [41] This study determined that the Fe_p of the paramagnetic [Fe^{1+}–Fe^{2+}] oxidized H-center is in the Fe^I oxidation state and binds to the cuboidal [4Fe4S] cluster, while the distal iron, Fe_d, alternates between Fe^I (reduction) and Fe^{II} (oxidation) states. It is the paramagnetic Fe_p^I ($3d^7$) ion that is the source of unpaired electron spin density that contributes to all iron hyperfine values observed for the formally diamagnetic $[4Fe4S]^{2+}$ center via spin density distribution across the entire 6Fe center. [41] All six iron hyperfine values were determined, the four of the [4Fe4S] cluster through ENDOR spectroscopy, with their overlapping, orientation-dependent pattern deconvoluted through the use of pulsed Davies TRIPLE experiments, a ‘pump–probe’ technique. [37] The weaker hyperfine values of the [FeFe] active site were determined through HYSCORE

spectroscopy. [41] This *tour de force* combination of advanced EPR techniques has fully characterized the iron electronic structure of the [FeFe]-hydrogenase.

Nitrogenase

ENDOR and ESEEM spectroscopies have been applied extensively to the "Everest of metalloenzymes" in an effort to shine light on biological reduction of dinitrogen to ammonia. [14, 58–60, 126] The complex mixed-metal active site of nitrogen reduction by nitrogenase, FeMo-co (Fe_7S_9CMo). As noted above, the early development of orientation-selective ENDOR occurred in the context of X-band ^{57}Fe field-modulated CW ENDOR studies of the resting-state (S = 3/2) FeMo-co. The hyperfine tensors thus derived [127–129] were later used for the Mössbauer analysis [130] More recently, 35 GHz ^{57}Fe ENDOR was used to identify the different CO-bound inhibitor states. [131, 132]

Most recently, 35 GHz Davies pulsed ^{57}Fe ENDOR was combined with the PESTRE techniques to allow the characterization of all seven of the Fe sites in an S = 1/2 hydrogen turnover state of FeMo-co that has accumulated four electrons/protons, stored as two hydrides that bridge Fe and two protons. [46] ^{57}Fe ENDOR studies yield the hyperfine tensors for five Fe sites of this intermediate and the coupling magnitude of a sixth. TRIPLE ENDOR provided valuable assistance in decomposing overlapping ^{57}Fe responses. Pulsed ENDOR Saturation and Recovery (PESTRE) allowed a direct measurement of the hyperfine signs, Figure 9. The PESTRE protocol employs three stages of Davies microwave pulse sequences: (I) no applied RF, to establish an electron spin echo baseline; (II) applied RF at the frequency of the probed ENDOR transition, applied to saturate the response; (III) RF frequency turned off, to monitor the ESE relaxation behavior which is characteristic of the ratio of A/g_n. A particular benefit of this technique is that it does not require comparison of the intensities of ν_+ and ν_- branches of an ENDOR spectrum, giving reliable sign information from a single branch.

Through the use of a sum-rule on the spin projection coefficients, [18] the magnitude and sign of all seven Fe sites are found. The significance of these measurements is to account for the four additional electrons of the E_4 state compared to resting state (E_0), using the Lowe-Thorneley scheme for nitrogenase intermediates. [133] The ^{57}Fe hyperfine character reveals that the formal redox state of the E_4 intermediate is the same as the resting state cluster, although it has four additional electrons. Therefore, these additional electrons must be 'stored' on 2 of the 4 protons of the E_4 intermediate as bridging hydrides, yielding critical insight into the nitrogenase mechanism.

Other Components: Heterometal

^{95}Mo ENDOR—The nitrogenase α-70^{Ile} MoFe protein described above contains two metal-bridging hydrido ligands, as characterized by ^{1,2}H ENDOR. [134] Although hydride binding only to Fe sites seemed more plausible, it was important to test the possibility of hydride binding involving the Mo ion. The Davies ENDOR studies at multiple magnetic fields of the ^{95}Mo-enriched intermediate showed that the isotropic ^{95}Mo hyperfine coupling was extremely small, $a_{iso} \approx 4$ MHz, decreased from that in the resting state (Figure 10). This a_{iso} value is at least five-fold less than the lower bound required by the ^{1,2}H ENDOR

measurements for Mo to be involved in forming a Mo-H-Fe, hydride. These measurements thus led to the conclusion that this catalytically central intermediate contains two Fe-H-Fe moieties. [60]

95Mo NK-ESEEM of a Nitrogenase S ≥ 2 Catalytic Intermediate—Rapid freezing during turnover of a remodeled nitrogenase MoFe protein (α-70$^{Val\rightarrow Ala}$, α-195$^{His\rightarrow Gln}$) with the electron-transfer Fe protein and with the substrates diazene, methyldiazene (HN=N-CH_3), hydrazine, NO_2^-, or NH_2OH each results in the loss of the resting-state signal from the catalytic FeMo-co and appearance of the signals from two new signals, Figure 11. [62] One signal (denoted ***I***) appears in the vicinity of g_2 and has $S = 1/2$. A second signal (denoted ***H***) is seen as a broad featureless absorption that begins near zero field and extends to ~ 5000 G (at Q-band). Such an EPR signature arises from an FeS cluster in an integer-spin, 'non-Kramers (NK)' state with $S \geq 2$. [62, 136] and could potentially be due to a variety of FeS systems; in nitrogenase, there are three such possibilities: the catalytically active FeMo-co cluster, the electron-transfer P-cluster (Fe7S9) also present in the MoFe protein; and [4Fe4S] cluster in the Fe protein.

NK-ESEEM [65, 67] was able to identify the source of the ***H*** signals. NK-ESEEM time-waves of the ***H*** signal of ^{95}Mo enriched MoFe protein produced significant changes of the NK-ESEEM time-wave, which established that this NK-EPR signal arose from the Mo-containing FeMo-co in an integer-spin state, and not the all-iron P or [4Fe4S] clusters. [62]

Other Components: Sulfide

The first ^{33}S ENDOR measurements were performed on the reduced cluster of aconitase, and analysis of ^{33}S resonances from the $[4Fe4S]^+$ cluster of the enzyme-substrate complex suggested that the sulfur sites occur as two pairs ($S_{\alpha 1}$, $S_{\alpha 2}$; $S_{\beta 1}$, $S_{\beta 2}$) with remarkably small spin density on sulfur, and even disclosed their spatial relation to the Fe sites. [137] Figure 12 summarizes the information from the ^{57}Fe and ^{33}S studies about the four Fe and four inorganic sulfides, placing it within the context of the X-ray diffraction structure, [138] which showed that cysteines are bound to the three iron ions that correspond to the three F_b seen spectroscopically. Subsequently, ^{33}S ENDOR measurements were performed on the resting-state FeMo-co of nitrogenase. [128] We should note that the substitution of NMR/ENDOR-active ^{77}Se ($I = 1/2$) for S in a [2Fe2S] cluster was instrumental in deducing the stoichiometry of these clusters. [139]

Cluster Ligation

Nitrogenous Protein-Derived Ligands (Rieske and Fra2)

The [2Fe2S] cluster is found in many proteins across Nature and comprises several classes. These include clusters with complete cysteine coordination as in ferredoxins, [7, 8, 20, 140–143] or with some degree of noncysteine coordination. This section focuses on advanced EPR studies of the protein-derived, non-cysteinyl ligands of the FeS cluster. This situation was first examined for [2Fe2S] clusters with the Rieske and *Fra2* proteins. Single histidine ligation (i.e., (Cys_2 [$Fe^{III}S_2Fe^{II}$]HisCys)) is found in the yeast regulatory protein Fra2-Grx3, which has been characterized by ENDOR, [144] and the human protein mitoNEET, and has

been well characterized by advanced EPR. [78, 145–147] Double histidine ligation ($Cys_2[Fe^{III}S_2Fe^{II}]His_2$) occurs in the well studied Rieske proteins [79, 148–152]. These active site structures are all shown in Figure 13. We discuss here the more recent example of mitoNEET, and the demonstration that even arginine ligation exists, as in the sulfur atom donating [2Fe2S] cluster of Biotin Synthase. [153–156]

mitoNEET

The homodimeric [2Fe2S] human mitoNEET protein is located within the mitochondrial membrane. [147] This protein is known to interact with the thiazolidinedione class of diabetes drugs, however its primary function is currently unknown. [145] This [2Fe2S] cluster attained significant bioinorganic interest when it was revealed that it was coordinated by 3Cys 1His amino acids, [145] a first among [2Fe2S] proteins, differing from the all Cys ferredoxin class and 2Cys 2His Rieske class (see Figure 13). [79, 149–151, 157] The sole histidine of mitoNEET coordinates to the Fe through the N_δ of the imidazole ring, the same coordination as observed for each His in Rieske clusters. [145]

The multi-frequency EPR and ESEEM work at X- (9.5 GHz), K_a- (31 GHz), and 'Q'- (34 GHz) bands elucidated the full structural characteristics the individual clusters and the dipole interaction of the two $S = 1/2$ $[2Fe2S]^+$ clusters of the homodimer, [78] which are separated at a distance of 16 Å. [145] As is typically done, the Fe ions are separately described as a ferric, Fe^{III} $S = 5/2$, and ferrous, Fe^{II} $S = 2$, ions and an antiferromagnetically coupled representation results in the observed $S = 1/2$ ground state. [20] The coupled representation for a [2Fe2S] cluster typically represents a single isolated FeS cluster well, however, the close proximity of the two [2Fe2S] clusters (~16 Å) of the homodimer was taken into consideration. The uncoupled representation employed by Dicus, et al. [78] employs the usual Fe ion spin projections (Eq. 6) [158] and sums of all dipolar interactions of every iron of the two [2Fe2S] clusters, both *inter*-cluster and *intra*-cluster dipole interactions, 6 interactions total. This approach was advantageous for the assignment of the [2Fe2S] iron oxidation states as the intra-cluster dipolar distances vary enough to yield predictable differences in Fe-Fe couplings. By mapping the Fe-Fe pairs onto the crystal structure the assignment of the Fe^{II} and Fe^{III} oxidation states could be made to the specific iron sites of the [2Fe2S] clusters. In this model, the Fe^{III} can either be coordinated by the two cysteines or by one cysteine and one histidine. Only an assignment where the Fe^{III}-Fe^{III} intra-cluster pair occupies the inner iron sites, i.e., those with the least separation (Figure 14), yields a dipolar coupling observable by X-band EPR. Therefore the Fe^{II} ions occupy the outer intra-cluster pair and have the single histidine ligand coordinated, as shown by 'Fe2' in Figure 14. [78]

The small hyperfine interaction of the $^{14}N_\delta$ histidine was amenable to ESEEM spectroscopy, and multi-frequency microwave instrumentation allowed for the deepest available modulation to be obtained. To obtain the deepest amount of modulation, increased ESEEM signal, one may aim to be within the 'cancelation regime' where one electron manifold (M_S) is nearly canceled. This is the case when the hyperfine energy is (approximately) equal to twice its Larmor frequency. [159] Recall, as the microwave frequency of instrument is increased, the Larmor frequency of the resonant nuclei scales linearly. For example, the

Larmor frequency of ^{14}N is approximately 1.03 MHz for a $g = 2$ field position at X-band (9.5 GHz), but will increase to 3.40 and 3.84 MHz for the same EPR transition at K_a (31 GHz) and Q-band (35 GHz), respectively. One of the largest advantages of moving in microwave frequency from X- up to Q-band is that proton resonances are shifted from the nitrogen region as the proton, with its large g_N value, Larmor frequency moves from 14 MHz to > 50 MHz.

The mid-range frequency ESEEM studies by Dicus, et al. [78] assigned the coordinating histidine nitrogen, N_δ, to the Fe^{II} ion of the reduced $[2Fe2S]^+$ cluster of mitoNEET. As ^{15}N lacks a quadrupole moment, the transitions obtained by ESEEM are a result of only the anisotropic portion of the hyperfine tensor, allowing for a more direct estimate of the dipolar contribution, which can be used in refining the ^{14}N ESEEM analysis. The values of $(^{15}N)a_{iso} = 8.77$ MHz and $T = 1.77$ MHz obtained by both K_a- and Q-band ESEEM were consistent with both Q-band Davies ENDOR and HYSCORE spectroscopies, demonstrating the accuracy of obtaining the ^{15}N hyperfine tensor through ESEEM at either K_a or Q band microwave frequencies.

The ^{14}N hyperfine parameters are scaled from the ^{15}N ESEEM analysis by their nuclear gyromagnetic ratio $|A(^{14}N)/A(^{15}N)| = |g_n(^{14}N)/g_n(^{15}N)| = 0.713$, which then facilitates extraction of the ^{14}N quadrupole parameters. The complete ^{14}N quadrupole tensor, $\mathbf{P}(^{14}N)$ and its relative orientation with respect to the iron sulfur cluster could then be elucidated by extensive analysis involving field dependent simulations and crystal structure information. From the simulation-determined **P** and **A** orientations with respect to **g**, assuming a typical quadrupole tensor orientation for the imidazole nitrogen, [24] the orientation of **g** was mapped on the cluster with its principal component, g_1, lying in the Fe-(μ)S_2-Fe plane, offset 33° from the Fe-Fe vector, Figure 15. This assignment for mitoNEET is in partial agreement with that of the original Rieske protein studies, where g_1 was also assigned along the Fe-Fe vector. [79] It also only partially agrees with the later study on Rieske protein of bovine mitochondrial cytochrome *bc*1 complex by Bowman, et al., [149] who had available a protein crystal. Single crystal EPR has the ability to definitively map a **g** tensor onto the molecular frame. The Rieske bishistidine ligated [2Fe2S] core in the single-crystal case was found to have g_1 close to the S-S vector. [149] Ultimately, single crystal EPR would need to be done on mitoNEET along with further examples of Rieske clusters to determine **g** tensor orientations overall in these systems. Such information would greatly assist computational studies of electronic structure of [2Fe2S] centers and how changes in coordination can tune the redox and catalytic properties of these important systems.

Biotin Synthase

The biotin synthase enzyme (BS, or BioB) contains two FeS clusters. One is a [4Fe4S] cluster which binds S-adenosylmethionine (SAM or AdoMet) as observed by crystallography [155] and catalyzes the production of 5′-deoxyadenosyl radical (5′-dA•) as performed by the radical SAM enzyme family, to be discussed later. The [4Fe4S] radical SAM cluster is not air-stable and is lost within minutes upon exposure to air and is thus absent from protein purified aerobically. A second single air-stable $[2Fe2S]^{2+}$ cluster is

observed per monomer of the biotin synthase homodimer isolated and purified from *E. coli*. [153]

Isotopic ^{15}N labeling of the Arg amino acids through the incorporation of (*guanidino*-$^{15}N_2$)-L-arginine into the growth media confirms the ligation of the paramagnetic $[2Fe2S]^+$ cluster by the amino group of Arg260 (see Figure 13) and is supported by the previous loss of ^{14}N hyperfine coupling observed for the Arg260Met variant by previous 3-pulse ESEEM spectroscopy and more recent $^{14/15}N$ HYSCORE studies (Figure 16). [153, 156] This unique Arg ligation to a $[2Fe2S]^+$ cluster, also observed in the crystal structure, [155] introduces another $[2Fe2S]^+$ cluster with non-cysteine coordination.

Spectroscopy of Substrates

The [4Fe4S] clusters serve many functions in Nature. Initially characterized solely as electron transfer agents, as in ferredoxins and other redox enzymes, their roles quickly expanded upon the discovery of the unique open iron site of the [4Fe4S] cluster of aconitase. [160] Beinert and Kennedy [137, 161–163] were the first to characterize an FeS cluster that catalyzed a chemical reaction, not just electron transfer. This section focuses on advanced EPR studies of exogenous compounds: substrates, substrate analogs, or inhibitors, which interact with the FeS cluster active site of such enzymes, and either have naturally occurring magnetic nuclei (^1H, ^{14}N, ^{31}P) or can be specifically labeled with them (^2H, ^{13}C, ^{15}N).

Aconitase

The enzyme aconitase catalyzes the stereospecific interconversion of citrate and isocitrate via the dehydrated intermediate *cis*-aconitate, Figure 17. The active site contains a $[4Fe4S]^{2+}$ cluster that can be reduced to the EPR-active $[4Fe4S]^+$ state with retention of activity. The cluster does not act in electron transport but rather performs its catalytic function through interaction with substrate at a specific single iron site of the cluster (Fe_a), first identified by Mössbauer. [164] This enzyme was the test bench whose study not only showed how ENDOR spectroscopy could determine active-site composition and electronic and geometric structure: ENDOR studies of substrate interactions made decisive contributions to the determination of the enzyme catalytic mechanism.

The first question addressed in the ENDOR investigation of the catalytic role of the cluster in a dehydration/hydration reaction was whether solvent H_xO (H_2O or OH^-) and/or the OH of substrate binds to the cluster. The use of ^{17}O, ^1H, and ^2H ENDOR showed that the fourth ligand of Fe_a in substrate-free enzyme is a hydroxyl ion from solvent, and that binding of substrate or substrate analogues to Fe_a causes the hydroxyl to become protonated to form a bound water molecule. Note that this represented the first demonstration of an exogenous ligand bound to an iron-sulfur cluster. The studies further suggested that the cluster might simultaneously coordinate the OH of substrate and H_2O of the solvent (Figure 17).

The second key question was whether one or more carboxylate groups of substrate bind to the cluster. This was answered through the use of ^{17}O ENDOR spectroscopy in conjunction with the biochemical brilliance of Beinert and Kennedy. Figure 17 presents ENDOR spectra of $[4Fe4S]^+$ aconitase in the presence of three citrate isotopologues in which the three

carboxyl groups have been *individually* labeled with ^{17}O. ENDOR measurements with substrate whose central (β) carboxyl group is ^{17}O labeled show a strong ^{17}O pattern but no ^{17}O ENDOR signal was observed when either of the terminal carboxyl groups (α or γ) was ^{17}O labeled (Figure 17). Thus under the experimental conditions of these samples, the central carboxyl group binds to Fe_a, but the two terminal groups (α or γ) do not bind to the cluster. The end result of these and other ^{17}O ENDOR measurements was that the substrate is bound as a chelate involving the citrate hydroxyl and a β-carboxyl oxygen, Figure 12. This ENDOR-derived structure for the substrate-bound cluster was eventually corroborated by subsequent X-ray diffraction studies. [165]

However, the enzyme also is able to accommodate substrate bound by the α-carboxyl, as was shown by ^{17}O ENDOR of enzyme that had bound a ^{17}O -enriched isocitrate analogue that lacks the β-carboxylate. Presumably the addition of the negatively charged carboxyl causes protonation of the OH- that binds to the cluster in the absence of substrate. The resulting structure of citrate bound to the unique Fe of the cluster, as deduced from ENDOR spectroscopy, is shown in Figure 12.

ENDOR spectroscopy thus showed that the cluster functions as follows: *(i)* it helps to position the substrate through the binding of one carboxyl; *(ii)* it coordinates and accepts the hydroxyl of substrate during the dehydration of citrate and isocitrate; *(iii)* it donates a bound hydroxyl during the rehydration of *cis*-aconitate. To accommodate the stereochemistry of the reaction, *cis*-aconitate must furthermore disengage from the active site, rotate 180°, and switch the carboxyl that binds before completing the catalytic cycle.

Nitrogenase—The mechanism of nitrogenase has been probed by ENDOR of numerous isotopically labeled substrates. [61, 166, 167] A detailed discussion of this aspect of the use of ENDOR is beyond the scope of this review, but has been recently summarized elsewhere. [58–60, 168]

Radical SAM

Following aconitase, other catalytic [4Fe4S] clusters have been discovered, [171] leading to a renaissance of interest in FeS proteins. The realization that the role of [4Fe4S] clusters extends beyond electron transfer has been greatly magnified by the discovery of their role in the radical SAM (S-adenosylmethionine) enzymes. Radical SAM enzymes comprise a diverse and rapidly expanding superfamily that has been recently reviewed (many times) [121, 172–176] [177–179] [180] and is the subject of other contributions to this volume (**References This Issue**).

Enzymes of the radical SAM superfamily utilize a [4Fe–4S] cluster and *S*-adenosylmethionine (SAM) to generate catalytically essential radicals, Figure 18. A key mechanistic question posed by this family was the role of the [4Fe–4S] cluster bound by a characteristic CX_3CX_2C motif. As with aconitase, the clusters of these enzymes have a “unique” iron site that is not coordinated to the enzyme by a cysteinyl sulfur: does this Fe have a catalytic function, as is true for aconitase? This question was answered through the use of EPR and pulsed 35 GHz ENDOR spectroscopy applied to the radical-SAM enzymes, pyruvate formate-lyase (PFL) activating enzyme (PFL-AE), and lysine 2–3 aminomutase

(LAM). [170, 181, 182] The experiments disclosed that the cluster plays at least a dual role: the unique Fe anchors the AdoMet cofactor by chelating the amino and carboxyl groups of methionine; electron transfer from the cluster initiates homolytic cleavage of the bond to adenosine.

^{2}H and ^{13}C pulsed ENDOR spectroscopy was performed on [4Fe–4S]$^{+}$-PFL-AE (S = 1/2) with bound AdoMet (denoted [1+/AdoMet]) that had been labeled at the methyl position with either ^{2}H or ^{13}C (see Figure 19). [181] The observation of substantial ^{2}H and ^{13}C hyperfine couplings from the labels clearly demonstrated that AdoMet binds adjacent to the 4Fe cluster. The cofactor was shown to bind in the same geometry to both the 1+ and 2+ states of the cluster through cryoreduction of the frozen [4Fe–4S]$^{2+}$/AdoMet complex to form the EPR-active reduced (1+) state which was trapped in the structure of the oxidized (2+) state.

Modeling of the through-space electron–nuclear dipolar interaction between the cluster electron spin and the methyl-^{13}C and ^{2}H showed that the shortest distance between an AdoMet methyl proton and an iron of the cluster is ~3.7(2) Å, with a distance of ~4.9(6) Å from the methyl carbon to this iron. Most intriguingly, the analysis disclosed a through-bond (local), isotropic contribution to the ^{13}C interaction, which requires overlap between orbitals on the cluster and on AdoMet. Later studies of the same state formed within LAM indicated that the coupling likely arises from interaction of the SAM sulfur with the unique Fe of the cluster.

The coordination sphere of the unique Fe was examined by 35 GHz pulsed ENDOR spectroscopic studies of PFL-AE complexed with SAM labeled with ^{17}O/^{13}C in the carboxyl group of the methionine fragment, and with ^{15}N in the amino group. [182] ENDOR signals observed with all three labels (Figure 19) showed that both the carboxylato and amino groups of methionine are coordinated to the unique iron of the [4Fe4S] cluster in a classical five-membered-ring N/O chelate. The key structural role of the cluster revealed by ENDOR spectroscopy was subsequently confirmed by X-ray diffraction studies, Figure 19. [155, 177, 183, 184]

The formation of the amino-acid chelate to the unique Fe anchors the methionine end of SAM, thereby fixing the geometry of the sulfonium linkage for the subsequent initiation of radical chemistry. In conjunction with the localization of the methylsulfonium moiety near to the unique Fe, as revealed by the ^{13}C and ^{2}H ENDOR measurements, these results led to a proposed reaction mechanism in which inner-sphere electron transfer from the cluster to SAM causes cleavage of the methionine-sulfonium/adenosyl bond that in part is driven by the formation of a coordinate bond between the unique Fe and the thioether sulfur of the methionine product of SAM fragmentation, Figure 18. The anchoring of SAM and the methionine product to the [4Fe4S] cluster in the structure exhibited in Figures 18 and 19 is a general bonding motif observed for all radical SAM enzymes.

Heterodisulfide reductase

As introduced earlier, Hdr reduces the disulfide bond of CoM-S-S-CoB. Isotopic ^{13}C labeling of CoM-SH at the second carbon of mercaptoethane sulfonate and subsequent

oxidation with CoM formed the singly labeled disulfide product, CoM-S-S-$^{13}CH_2CH_2SO_3^-$. [106] This allowed ^{13}C Mims ENDOR spectroscopy to yield ^{13}C hyperfine couplings and confirm the substrate's binding to the [4Fe4S] cluster of HdrB, Figure 20. The ^{13}C couplings, [1.8, 1.8, 0.4] MHz, are comparable to those observed for the ^{13}C hyperfine of methyl-^{13}C-AdoMet binding to the [4Fe4S] cluster of PFL-AE (*vide supra*). [181] These small couplings are expected as the ^{13}C label is one bond away from the S that is directly interacting with the FeS cluster. [106] In contrast, an Fe ion directly bound to ^{13}C would give much larger couplings, A_{min} = 12 MHz. [185]

The 'Second Cluster' of Radical SAM Enzymes

Numerous Radical SAM enzymes have a 'second cluster' in addition to the 4Fe4S cluster that binds SAM and reductively cleaves it. The role of the second cluster has also been investigated with advanced paramagnetic resonance techniques, beginning with the ENDOR study of MoA.

MoaA

The enzymes MoaA and MoaC catalyze the first step in the biosynthesis of the molybdenum cofactor (Moco) found in the biologically important molybdopterin enzymes, such as xanthine oxidase. [186] Each of these Moa enzymes contain two $[4Fe4S]^{2+,+}$ clusters. One $[4Fe4S]^{2+,+}$ site, cluster I, is found in an N-terminus CX_3CX_2C motif and is a characteristic Radical SAM cluster that generates the 5′-dA• radical to further catalyze the conversion of guanosine 5′-triphosphate (5′-GTP) substrate to tetrahydropyranopterin. [183, 187] The role of the other cluster, cluster II, was less certain, although X-ray crystallography clearly indicated that it was involved in substrate 5′-GTP binding and/or activation. A crystal structure of MoaA with 5'-GTP suggested an atom of the purine ring might be coordinating to a unique iron of the second [4Fe4S] cluster, [187] however, ambiguity remained as to whether it was the exocyclic amino group or nitrogen of the purine ring that is coordinating. The ambiguity of interaction of the 5′-GTP substrate with cluster II was a perfect candidate for unraveling by ENDOR spectroscopy.

The Radical SAM [4Fe4S] S = 1/2 cluster of MoaA was disrupted through mutagenesis of its CX_3CX_2C binding motif cysteines. The CW EPR and ENDOR signals of this mutant then arise only from cluster II, the site of 5′-GTP binding. The ENDOR exhibits ^{14}N hyperfine coupling [188] similar to that found for the amino-nitrogen of the SAM bound to iron in PFL-AE. [182] Nitrogen coordination is easily confirmed through global ^{15}N labeling of the 5′-GTP substrate and the observed ^{15}N ENDOR response at the expected shift in frequency as determined from the ratio of the nuclear g_N values: $\gamma = |A(^{15}N)/A(^{14}N)| = |g_N(^{15}N)/g_N(^{14}N)| = |1.41|$. [11, 188] However, given that the 5′-GTP substrate was globally labeled in ^{15}N, the issue of whether it is the purine ring or amino nitrogens of 5′-GTP that bind to cluster II is not resolved. [187] Employing an active substrate analogue, inosine 5′-triphosphate (5′-ITP), which lacks the exocyclic amino group at C2 (termed N2) of 5′-GTP, yielded a very similar EPR signal as with the natural substrate and remarkably similar ^{14}N ENDOR couplings were observed. This result confirms that either N1 or N3 of purine rings of both 5′-GTP substrate and 5′-ITP are the sources of nitrogen coordination to the fourth iron of the [4Fe4S] cluster, not the exocyclic amino group (in 5′-GTP). [188]

Both 5′-GTP substrate and 5′-ITP have multiple purine nitrogen atoms, N1 and N3, and correspondingly multiple nitrogen ENDOR signals of various couplings. [188] With these differing couplings, point-dipole distance estimations could be made for each nitrogen coupling and in conjunction with the predicted bound structure from X-ray crystallography, [187] allowed for the assignment of these couplings. The strongest coupled nitrogen belongs to N1 of the purine ring, not the exocyclic amino group, as shown through the use of the substrate analogue. However, signals from two additional nitrogens were anticipated, one from the purine ring and the other from the exocyclic amino group, at further distances and thus with weaker couplings. Pulsed Mims ENDOR for the weaker coupled N2 and N3 of the purine yielded maximum couplings of (^{15}N)A = 0.5 and 0.2 MHz. The maximum and minimum dipolar components of each nitrogen measurement yield point-dipole model estimates of the distance between the nuclear (^{15}N) spin and the unpaired electron spin of the [4Fe4S]$^{+}$ cluster.

By maintaining the crystallographically well resolved phosphate moiety of 5′-GTP in its fixed position, the ribose sugar and purine ring groups could then be positioned with respect to the [4Fe4S]$^{+}$ cluster to match the cluster-nitrogen distance estimates determined by ENDOR spectroscopy. Figure 22 superimposes the 5′-GTP model made through the ENDOR distance measurements upon that from the previous X-ray crystal structure. One can readily see some differences and indeed improvements upon the crystal structure. As ENDOR spectroscopy is performed on solution ‘powder’ samples, the resulting structure may differ from that determined by X-ray crystallography of solid state crystals. In addition to providing another view of active site structure, ENDOR and other advanced EPR techniques have the potential of “seeing” these structures in intermediates that may not be easily crystallized.

Biotin synthase (BS)

BS catalyzes biotin synthesis by formation of a thioether linkage between the methylene (C6) and methyl (C9) positions of dethiobiotin (DTB). This sulfur addition is a two step process whereby a 5′-deoxyadenosyl radical (5′-dA•) is generated by a radical SAM cluster which next abstracts a hydrogen atom from the methyl group (C9) of DTB, Figure 23. The subsequent high-energy 9-dethiobiotinyl radical is quenched by the addition of a sulfur atom to form the stable enzyme intermediate 9-mercaptodethiobiotin (MDTB). The introduction of a second equivalent of AdoMet and the resulting generation of another 5′-dA• radical which abstracts a hydrogen from the methylene group (C6) to allow for the formation of the thioether group and ring closure.

While the [4Fe4S] cluster of biotin synthase is the site of AdoMet binding and 5′-dA• radical formation, [189] the candidacy of AdoMet as the sulfur donor to biotin was excluded by isotopic labeling: ^{35}S of ^{35}S-AdoMet is not incorporated into biotin. [190] After the classification of biotin synthase as a radical SAM enzyme, the origin of the sulfur atom that is inserted into biotin needed to be answered. The [2Fe2S] cluster, discovered initially by X-ray crystallography, [155] was also proposed as the sulfur atom source and shown to be the sulfur atom donor to MDTB by reconstitution of apoenzyme with Fe^{3+} and $^{34}S^{2-}$ and by the

substitution of S^{2-} by Se^{2-}, each incorporated as the sulfur (or selenium) atom for the ring closure of biotin. [191, 192]

As the formation of biotin is not a single step process, samples frozen during turnover are a mixture of EPR paramagnetic species poised at various states. [156] The initially proposed binding of the 9-dethiobiontinyl radical to the $[2Fe2S]^{2+}$ cluster yields an paramagnetic species, the reduced $[2Fe2S]^{+}$ cluster. [156] The formation of this reduced cluster creates a new paramagnetic probe for coordination studies of the MDTB intermediate formation. EPR studies previously showed that the reduction of the $[2Fe2S]^{2+}$ cluster was kinetically linked with the production of MDTB, however they were unable to conclusively determine if the reduction of $[2Fe2S]^{2+}$ cluster and MDTB formation occur at the same time. [156]

Recent HYSCORE studies of biotin synthase under turnover reveals that the dethiobiotinyl radical, a result of hydrogen abstraction by 5′-dA•, moves ~2.9 Å closer to the μ-sulfide of the $[2Fe2S]^{2+}$ cluster for attack and sulfur abstraction. [153] The (9-methyl-^{13}C)-DTB labeled substrate, obtained by biosynthesis, yielded ^{13}C coupling (a_{iso} = 2.9 MHz) observed by HYSCORE spectroscopy. This result is consistent with the newly formed MDTB intermediate remaining bound to the remnant FeS cluster through the sulfur atom (MDTB-Fe-(μ)S-Fe), [153] as depicted in Figure 23. The ^{13}C coupling is reminiscent of that observed for the Fe-S-^{13}C of the radical SAM PFL-AE enzyme. [182] This work has characterized the transient MDTB structure, and the binding of substrate to the subsequently remnant Fe-S-Fe cluster. [153] There is great potential for advanced EPR, such as in further characterization of the ring closure mechanism. The kinetics of biotin synthase are favorably slow, so rapid-freeze quench techniques can be dispensed with. Additionally, as the [2Fe2S] cluster is the sulfur donor to biotin, the [2Fe2S] cluster must be regenerated, but we are unaware of any results on the regeneration mechanism. Radical SAM enzymes often play a critical role in the maturation of FeS clusters, maybe the radical SAM character of this enzyme plays two roles?

MiaB

Recently, several radical SAM enzymes have been identified that catalyze the attachment of methylthio groups to transfer RNAs or ribosomal proteins. These enzymes are thus called methylthiotransferases (MTTases) and include MiaB, MtaB, and RimO. [193–197] [198] Very recently, MiaB and RimO from *Thermotoga maritima* (*Tm*MiaB, *Tm*RimO) have been investigated by advanced EPR techniques. [199] MiaB contains a radical SAM cluster, but, as described above in MoaA, there is an additional cluster (cluster II), which is proposed as the site of sulfur (here as CH_3S-) transfer. These workers used both WT and an inactive MiaB mutant in which the three Cys residues binding the radical SAM cluster were mutated to alanine, so that only cluster II remained, but cluster II retained the ability to bind exogenous ligands. In this case, CH_3 ^{77}SeNa was used (^{77}Se, I = 1/2, 7.6% natural abundance), which is an active substrate for these MTTases. HYSCORE of both WT and mutant showed signals due to ^{77}Se interacting with cluster II (A = 3.8(5) MHz) indicating direct binding and thus supporting the accepted mechanism for MTTases. [199]

^{14,15}N NK-ESEEM of a Nitrogenase Intermediate Common to Multiple substrates

We state above that rapid freezing of a remodeled nitrogenase MoFe protein during turnover with each of the substrates, diazene, methyldiazene ($HN{=}N\text{-}CH_3$), hydrazine, NO_2^- and NH_2OH results in trapping of a common NK state, ***H***, with $S \geq 2$. The conclusion that all these substrates react to generate ***H*** was arrived at from NK-ESEEM studies, which showed that the NK intermediates formed with each substrate give the same time and frequency-domain spectra, Figure 25. [62, 136] The NK-ESEEM studies of the intermediates formed with methyldiazene ^{14,15}N isotopologues plus ^{1,2}H isotopologues further demonstrated that ***H*** corresponds to the nitrogen fixation intermediate with FeMo-co-bound $[NH_2]^-$ that is formed upon N-N bond cleavage. [62]

Bio-Organometallic Enzyme Intermediates

Perhaps the most remarkable cluster-substrate complexes contain bio-organometallic moieties, involving Fe-C bonds (and not involving CN^- as seen in hydrogenase!). The first such was a state in which the nitrogenase active site binds the alkene product of alkyne reduction. Considerably later, this study was used as the foundation for efforts to assign analogous states of other catalytic [4Fe4S] clusters.

Nitrogenase

Biological ‘nitrogen fixation’, the reductive cleavage of the N_2 triple bond at ambient pressure and temperature to form two NH_3, is carried out by the nitrogenase enzyme system. The catalytic site is a multimetallic cluster, denoted FeMo-cofactor (FeMo-co), $[Fe_7,Mo,S_9,C]$. In recent years a number of states have been freeze-trapped with reduction intermediates of N_2 and alternative substrates bound to FeMo-co, and characterized by ENDOR/ESEEM/HYSCORE. The first of these were states trapped during the reduction of alkynes: acetylene, propargyl alcohol ($HC{\equiv}C\text{–}CH_2OH$), and propargyl amine ($HC{\equiv}C\text{–}CH_2NH_2$).

The as-isolated form of the nitrogenase WT MoFe protein exhibits a characteristic $S = 3/2$ electron paramagnetic resonance (EPR) spectrum from resting state FeMo-co. The α-Ala^{70}-remodeled MoFe protein behaves similarly, but this mutation allows the use of larger substrates than just N_2 or acetylene. When the α-Ala^{70}-MoFe protein is freeze-trapped under turnover conditions with either propargyl alcohol or propargyl amine, the resting state is converted to one with an $S = 1/2$ signal, similar to that observed when acetylene is used as substrate with WT enzyme. Such a well-defined EPR signal indicated that FeMo-co had been trapped with a single reduction intermediate bound in high occupancy, and thus an unprecedented opportunity to explore the properties of this intermediate by EPR and ENDOR spectroscopies was given.

^{13}C ENDOR spectroscopy carried out on this intermediate generated with uniformly ^{13}C-labeled propargyl alcohol gave signals from the three distinct C atoms of substrate with isotropic coupling to the FeMo-co spin in order of magnitude: C3 > C2 > C1 (Figure 26A, C).[24] This result established that the substrate-derived intermediate was covalently bound to metal ion(s) of the FeMo cofactor – that this state is bio-organometallic. However, even full

determination of the ^{13}C tensors through analysis of 2D field-frequency patterns could not reveal the structure of the complex.

The nature of the bound intermediate instead was revealed by a detailed examination of the $^{1,2}H$ ENDOR responses from the four isotopomers generated when H- or D-labeled propargyl alcohol (PA-H; PA-D) were used as substrate during turnover in either H_2O or D_2O. [200] Key was the combined use of a newly developed, *quantitative* ^{1}H ENDOR technique, stochastic field-modulated (SF) CW ENDOR, in conjunction with Mims-pulsed ^{2}H ENDOR, to study a strongly-coupled proton signal (H^a) observed in the PA-H/H_2O spectrum (hyperfine coupling of $A(^1H^a) \approx 20$ MHz) in the four isotopologs. As shown in Figure 26B, the signal observed for PA-H/H_2O appears with half intensity in the spectra of *both* the PA-H/D_2O and PA-D/H_2O samples, and it is lost with the "doubly deuterated" PA-D/D_2O sample. Correspondingly the Mims ^{2}H ENDOR spectrum of PA-D/D_2O was seen with half the intensity for PA-H/D_2O and PA-D/H_2O and was absent for PA-H/H_2O. These observations imply that the H^a doublet in the PA-H/H_2O spectrum is the superposition of doublets from two magnetically *identical* and hence *symmetry-equivalent (mirror-symmetry)* protons, one derived from propargyl alcohol substrate (H_p) and the other acquired from solvent (H_s) during reduction. In addition, the experiments disclosed one weakly coupled proton (H^b) derived from solvent.

Detailed examination of the structures of inorganic model compounds having similar compositions showed that these $^{1,2}H$ ENDOR measurements require that this intermediate is a complex of the alkene product of reduction, allyl acohol, bound in a three-membered ring made up of the propargyl alcohol C3 and C2 atoms and a single Fe atom. Figure 26C, a structure that can be viewed as either a ferracyclopropane adduct or a π complex of the allyl alcohol alkene product. Density functional theory (DFT) calculations on FeMo-co subsequently confirmed the structure. [201] Further work led to a proposed detailed bonding geometry of the cofactor–reduction intermediate shown in Figure 26D.

This mechanistic insight into the reduction of an organic substrate is one component of the organometallic character of PA-FeMoco. This ferracycle structure was crucial in providing the basis for deriving the mechanism of IspG/IspH, as described next. Such bioorganometallic species may become more widely found in Nature, with advanced EPR techniques being crucial in their identification.

Isoprene Precursor Synthesis Through Organometallic Intermediates

The synthesis of isoprene precursors, which include carotenoids, cholesterol, steroid hormones, vitamins, and quinones, by eubacteria and apicomplexan parasites occurs solely via the methyl-erythritol phosphate (MEP) pathway. [202, 203] Pathogenic microorganisms such as the causative agents of anthrax, plague, gastrointestinal ulcers, venereal diseases, malaria, and tuberculosis also solely depend on the MEP pathway for isoprenoid precursor production, making the MEP pathway an attractive target for the development of new drugs. [204, 205] The last two steps in the MEP pathway, shown in Figure 27, involve the proteins IspG ((*E*)-4-hydroxy-3-methylbut-2-enyl diphosphate synthase), initially known as GcpE, [206, 207] and IspH ((*E*)-1-hydroxy-2-methylbut-2-enyl 4-diphosphate reductase), initially known as LytB. [208]

Both IspG and IspH catalyze $2H^+/2e^-$ reductions of their substrates through organometallic intermediates, which have been characterized through advanced EPR techniques by two separate groups: the collaborative team of Duin (Auburn Univ.) and Hoffman (Northwestern Univ); and Oldfield (Univ. of Illinois, Urbana-Champaign).

Initial ENDOR and HYSCORE studies by Oldfield and colleagues [209] attempted to shed light on the conversion of 2-*C*-methyl-D-erythritol-2,4-cyclodiphosphate (MEcPP) to (*E*)-4-hydroxy-3-methyl-but-2-enyl diphosphate (HMBPP) by IspG. To test a previously proposed reaction mechanism involving an epoxide, [206] Oldfield compared the EPR, ENDOR, and HYSCORE spectroscopic characteristics of IspG with MEcPP or HMBPP binding, under turnover conditions and with a 2,3-HMBPP epoxide bound. Through uniform ^2H and both uniform and partial ^{13}C isotopic labeling of the MEcPP, the binding of substrate to the unique fourth iron was narrowed to occur via either 2C –**or**– 3C. A similar π/σ binding scheme for propargyl alcohol (PA) to the 7Fe9SMoC cluster (FeMo-co) of nitrogenase had earlier been described by Hoffman et al.; C1 exhibits ^{13}C couplings of a_{iso} = 3.7 MHz. [200] Taking as a model the work on propargyl alcohol bound to FeMo-co, Oldfield et al. proposed that the inhibition of IspG by alkynes results from their binding in an analogous organometallic π/σ fashion.

Duin and Hoffman [210] observed a strong ^1H ENDOR response in IspG with MEcPP, and proposed that it arose from the C2′ methyl group of MEcPP. This proposal was later confirmed by Oldfield through use of the isotopologue with ^2H at C2′. [185] Further studies with individual atom isotopic labeling confirmed that C2 is the carbon most strongly coupled to the FeS cluster and the strong ^1H response is from the C2′ methyl group. [185] This supported the structure proposed by Duin and Hoffman, where “a ferraoxetane with an Fe-C2 bond, [Figure 28] also considered by Wang et al.,[[209]] although not favored [by Oldfield], might be expected to have a large coupling to $^{13}C3$ and its α proton….”

Subsequent studies by Oldfield involved ^{17}O labeling of the hydroxyl group of MEcPP and the use of HYSCORE spectroscopy by Oldfield, which exhibited a strongly coupled ^{17}O nucleus [211], indication of a strong Fe-O interaction. Taken together, the $^1H/^2H$ [210], ^{13}C, and ^{17}O [185] ENDOR data create a consensus that IspG reacts via the ferraoxetane intermediate structure of Duin.

Following the production of HMBPP, IspH catalyzes its reduction into isopentenyl diphosphate and dimethylallyl diphosphate in ratios of 4:1 to 6:1 during the last step of the methylerythritol phosphate pathway. [212]

Initial characterization of IspH inhibitors by Oldfield yielded the highest inhibition of activity by alkynyl diphosphate, which was proposed to bind to the unique iron of the [4Fe4S] cluster as a π (or π/σ) metallocycle complex. [213] Later ^{13}C ENDOR spectroscopy, also by Oldfield, [211] revealed couplings once again similar to that observed for PA bound to nitrogenase. The analogy of the observed couplings with those for the PA properties, taken with the alkene inhibition observation, led Oldfield to propose a π/σ “metallacycle” or η_2-alkenyl complex. [211]

Later ENDOR spectroscopic studies by Hoffman and colleagues of freeze-quenched samples of the wild-type and mutant enzymes confirmed the binding of the HMBPP substrate to IspH through the observation of weak ^{31}P hyperfine dipolar couplings, A_{max} = 0.17 MHz. [214] A dipolar interaction with no isotropic contributions may be treated as a point-dipole with the Fe-S cluster as a single point, and allows for reliable distance measurements to be made for distant nuclei, yielding an Fe-^{31}P distance of $r \sim 7$ Å. [214] These measurements initiated the assembly of the coordination sphere around the [4Fe4S] cluster. Analogous dipolar distance determinations were made for the racemate mixture of a single ^{2}H label at the same carbon position as the hydroxyl group is attached, C1 (Figure 28), of HMBPP. This deuteron creates a new ENDOR 'probe' on the opposite end of the substrate from the ^{31}P of the phosphate group. Its ^{2}H ENDOR signal gives a calculated distance of r(Fe-^{2}H) = 3.4 Å, implying that this carbon with the hydroxyl group is adjacent to site of linkage to the FeS cluster. HMBPP is bound through *either* the hydroxyl or as a π complex with a Fe-O linkage of the freeze-trapped intermediate. [214]

Isotopic labeling by Oldfield of the hydroxyl group of HMBPP with ^{17}O yielded weak ^{17}O hyperfine couplings, compared to IspG, implying the absence of direct Fe-O bonding. [215, 216] This eliminated the possibility of binding through the hydroxyl group for the structure observed by Oldfield, contrasting with the freeze-trapped structure proposed by Duin and Hoffman. However, π binding of the allyl groups is still a viable mechanism, as previously suggested by Duin and Hoffman. [214] The final mechanism proposed by Oldfield, partially supported by crystallography, [217] discarded the possibility of the ferraoxatane, but instead supports an η-3 allyl anion mechanism. Through the combined methods of crystallography and advanced EPR, Groll and Oldfield have made additional studies of the inhibitors of IspG and IspH and their organometallic binding modes. [215–219]

Outlook

Advanced EPR techniques, namely ENDOR, and ESEEM and HYSCORE spectroscopies, have been crucial in understanding FeS proteins from the early days of their discovery. ENDOR, along with EPR and Mössbauer, was decisive in understanding the nature of magnetic coupling in ferredoxin FeS clusters that gave rise to their varying electron spin states. This in turn was connected to their redox properties, the only role initially assigned to FeS proteins. ENDOR also was essential in analyzing more complicated FeS systems, specifically nitrogenase FeMo-co, wherein the Fe and Mo sites were identified and quantified. The next phase was the key role played by ENDOR in demonstrating that an FeS cluster, in the citric acid cycle enzyme aconitase, was the catalytically active site for an organic transformation. Since then, advanced EPR techniques have gone in tandem with the biochemical progress on FeS proteins. Notable examples include work on unraveling the structure and mechanism of FeFe hydrogenase and on nitrogenase, wherein the tools of molecular biology and enzymology allowed the characterization of enzyme intermediates that has led to a deeper understanding of the mechanism of biological nitrogen fixation, and that an authentic organometallic moiety can exist on an FeS cluster. Another phase in the saga of FeS proteins is the identification of the radical SAM superfamily, whose membership and variety of chemical catalysis is constantly growing. Here again, ENDOR and ESEEM and HYSCORE have all been instrumental in directly providing information

that has allowed mechanism to be proposed for quite intricate organic reactions. The preparation of suitable isotopologs of substrates/inhibitors – many of which could be useful for NMR studies in other contexts, is also an important part of this progress. We conclude by expressing the belief that as long as biochemists are working on FeS proteins, practitioners of advanced EPR spectroscopic techniques can make major contributions to advance this important field.

Acknowledgments

The authors thank Jacques Meyer for helpful conversations and careful reading of this manuscript. The authors also thank Jacques Meyer for providing the *Aquifex aeolicus* Fd1 sample, Jose Moura, UNL, Lisbon, Portugal for the sample of *Desulfovibrio gigas* Fd, and Mary Claire Kennedy, Medical College of Wisconsin, for the sample of *Ectothiorhodospira halophila* HiPIP. This work was supported by the National Institutes of Health (GM111097 to B.M.H.) and the National Science Foundation (MCB-1118613 to B.M.H., and DGE-0824162 to G.E.C.).

Abbreviations

Spectroscopic terms

CW	continuous wave
EPR	electron paramagnetic resonance
ENDOR	electron nuclear double resonance
ESEEM	electron spin echo envelope modulation
hfc	hyperfine coupling
HYSCORE	hyperfine sublevel correlation
PESTRE	Pulsed ENDOR Saturation and Recovery
RF	radiofrequency

Biochemical terms

Aae	*Aquifex aeolicus*
AdoMet/SAM	*S*-adenosylmethionine
BioB/BS	Biotin synthase
CoM	coenzyme M, mercaptoethane sulfonate
CoB	coenzyme B, 7-mercaptoheptanoyl-L-threonine phosphate
Fd	ferredoxin
FeMo-co	iron molybdenum cofactor of nitrogenase
FeS	iron-sulfur
5′-GTP	guanosine 5′-triphosphate
Hdr	Heterodisulfide reductase
HiPIP	High Potential Iron-Sulfur Protein

HMBPP	(*E*)-4-hydroxy-3-methyl-but-2-enyl diphosphate
5′-ITP	inosine 5′-triphosphate
MDTB	9-mercaptodethiobiotin
MEcPP	2-*C*-methyl-D-erythritol-2,4-cyclodiphosphate
MiaB, RimO	Radical *S*-adenosyl methionine methylthiotransferase (MTTase) enzymes
MoaA	Molybdenum cofactor biosynthetic enzyme
PFL-AE	Pyruvate formate lyase-activating enzyme

References

1. Sands RH, Beinert H. Studies on mitochondria and submitochondrial particles by paramagnetic resonance (EPR) spectroscopy. Biochem. Biophys. Res. Commun. 1960; 3:47–52.
2. Shethna YI, Wilson PW, Hansen RE, Beinert H. Identification by isotopic substitution of EPR signal at $g = 1.94$ in non-heme iron protein from *Azotobacter*. Proc. Nat. Acad. Sci. 1964; 52:1263–1271. [PubMed: 14231451]
3. Feher G. Observation of nuclear magnetic resonances via the electron spin resonance line. Phys. Rev. 1956; 103:834–835.
4. Feher G. Electron spin resonance experiments on donors in silicon. I. Electronic structure of donors by the electron nuclear double resonance technique. Phys. Rev. 1959; 114:1219–1244.
5. Lambe J, Laurance N, McIrvine EC, Terhune RW. Mechanisms of double resonance in solids. Phys. Rev. 1961; 122:1161–1170.
6. Mims WB. Pulsed endor experiments. Proc. Roy. Soc. Lond. 1965; 283:452–457.
7. Fritz J, Anderson R, Fee J, Palmer G, Sands RH, Tsibris JC, Gunsalus IC, Orme-Johnson WH, Beinert H. The iron electron-nuclear double resonance (ENDOR) of two-iron ferredoxins from spinach, parsley, pig adrenal cortex and *Pseudomonas putida*. Biochim Biophys Acta. 1971; 253:110–133. [PubMed: 4331268]
8. Anderson R, Dunham WR, Sands RH, Bearden AJ, Crespi HL. On the nature of the iron sulfur cluster in a deuterated algal ferredoxin. Quarterly Review of Biophysics. 1975; 7:443–504.
9. Abragam, A.; Bleaney, B. Electron Paramagnetic Resonance Of Transition Ions. New York: Dover Publications; 1986.
10. Schweiger A. Pulsed electron spin resonance spectroscopy: Basic principles, techniques, and examples of applications. Agnew. Chem. Int. Ed. Engl. 1991; 30:265–292.
11. Weil J, Bolton J. Electron Paramagnetic Resonance (2 ed.). 2011
12. Möbius, K.; Lubitz, W. Biological Magnetic Resonance. Boston, MA: Springer US; 1987. ENDOR Spectroscopy in Photobiology and Biochemistry; p. 129-247.
13. Hoffman BM. Electron nuclear double resonance (ENDOR) of metalloenzymes. Acc. Chem. Res. 1991; 24:164–170.
14. Hoffman BM. ENDOR of metalloenzymes. Acc Chem Res. 2003; 36:522–529. [PubMed: 12859213]
15. Schweiger, A. Electron Nuclear Double Resonance of Transition Metal Complexes with Organic Ligands. Vol. 51. Berlin, Heidelberg: Springer Berlin Heidelberg; 1982. Electron nuclear double resonance of transition metal complexes with organic ligands; p. 1-119.
16. DeRose, VJ.; Hoffman, BM. Protein Structure and Mechanism Studied by Electron Nuclear Double Resonance Spectroscopy. In: Sauer, K., editor. Methods in Enzymology. Vol. 246. New York: Academic Press; 1995. p. 554-589.
17. Noodleman L, Peng CY, Case DA, Mouesca JM. Orbital interactions, electron delocalization and spin coupling in iron-sulfur clusters. Coord. Chem. Rev. 1995; 144:199–244.

18. Mouesca JM, Noodleman L, Case DA, Lamotte B. Spin densities and spin coupling in iron-sulfur clusters: A new analysis of hyperfine coupling constants. Inorg. Chem. 1995; 34:4347–4359.
19. Telser J, Huang H, Lee H-I, Adams MWW, Hoffman BM. Site Valencies and Spin Coupling in the 3Fe and 4Fe (S = 1/2) Clusters of *Pyrococcus furiosus* Ferredoxin by ^{57}Fe ENDOR. J. Am. Chem. Soc. 1998; 120:861–870.
20. Cutsail GE 3rd, Doan PE, Hoffman BM, Meyer J, Telser J. EPR and ^{57}Fe ENDOR investigation of 2Fe ferredoxins from *Aquifex aeolicus*. JBIC, J. Bio. Inorg. Chem. 2012; 17:1137–1150.
21. Lee H-I, Hales BJ, Hoffman BM. Metal-Ion Valencies of the FeMo Cofactor in CO-Inhibited and Resting State Nitrogenase by ^{57}Fe Q-Band ENDOR. J. Am. Chem. Soc. 1997; 119:11395–11400.
22. Manikandan P, Choi EY, Hille R, Hoffman BM. 35 GHz ENDOR characterization of the "very rapid" signal of xanthine oxidase reacted with 2-hydroxy-6-methylpurine (^{13}C8): evidence against direct Mo-C8 interaction. J Am Chem Soc. 2001; 123:2658–2663. [PubMed: 11456936]
23. Hutchison CA, McKay DB. The determination of hydrogen coordinates in lanthanum nicotinate dihydrate crystals by Nd^{+3}-proton double resonance. J. Chem. Phys. 1977; 66:3311.
24. Lucken, EAC. Nuclear quadrupole coupling constants. London, New York: Academic P.; 1969.
25. Mims WB, Peisach J. The nuclear modulation effect in electron spin echoes for complexes of Cu^{2+} and imidazole with ^{14}N and ^{15}N. J. Chem. Phys. 1978; 69:4921.
26. Hoffman BM, Martinsen J, Venters RA. General theory of polycrystalline ENDOR patterns. g and hyperfine tensors of arbitrary symmetry and relative orientation. J. Magn. Reson. 1984; 59:110–123.
27. Hoffman BM, Venters RA, Martinsen J. General theory of polycrystalline ENDOR patterns. Effects of finite EPR and ENDOR component linewidths. J. Magn. Reson. 1985; 62:537–542.
28. Hoffman, BM.; Gurbiel, RJ.; Werst, MM.; Sivaraja, M. Electron nuclear double resonance (ENDOR) of metalloenzymes. In: Hoff, AJ., editor. Advanced EPR : applications in biology and biochemistry. Amsterdam; New York New York, NY, U.S.A.: Elsevier; Distributors for the U.S. and Canada, Elsevier Science Pub. Co.; 1989. p. xxiip. 918
29. Doan PE. The past, present, and future of orientation-selected endor analysis: Solving the challenges of dipolar-coupled nuclei. Paramagnetic Resonance of Metallobiomolecules, ACS SYMPOSIUM SERIES. 2003
30. Epel B, Poppl A, Manikandan P, Vega S, Goldfarb D. The effect of spin relaxation on ENDOR spectra recorded at high magnetic fields and low temperatures. J. Magn. Reson. 2001; 148:388–397. [PubMed: 11237646]
31. Epel B, Arieli D, Baute D, Goldfarb D. Improving W-band pulsed ENDOR sensitivity—random acquisition and pulsed special TRIPLE. J. Magn. Reson. 2003; 164:78–83. [PubMed: 12932459]
32. Davies ER. A new pulse endor technique. Phys. Lett. A. 1974; 47:1–2.
33. Doan PE, Lees NS, Shanmugam M, Hoffman BM. Simulating suppression effects in Pulsed ENDOR, and the 'hole in the middle' of Mims and Davies ENDOR Spectra. Appl. Magn. Res. 2010; 37:763–779.
34. Schweiger, A.; Jeschke, G. Principles of pulse electron paramagnetic resonance. Oxford, UK ; New York: Oxford University Press; 2001.
35. Fan C, Doan PE, Davoust CE, Hoffman BM. Quantitative studies of davies pulsed ENDOR. J. Magn. Reson. 1992; 98:62–72.
36. Doan PE, Hoffman BM. Making hyperfine selection in Mims ENDOR independent of deadtime. Chem. Phys. Lett. 1997; 269:208–214.
37. Gemperle C, Schweiger A. Pulsed Electron Nuclear Double-Resonance Methodology. Chem. Rev. 1991; 91:1481–1505.
38. Kinney RA, Hetterscheid DGH, Hanna BS, Schrock RR, Hoffman BM. Formation of $\{[HIPTN_3N]Mo(III)H\}^-$ by Heterolytic Cleavage of H_2 as Established by EPR and ENDOR Spectroscopy. Inorg. Chem. 2010; 49:704–713. [PubMed: 20000748]
39. Lee Y, Kinney RA, Hoffman BM, Peters JC. A nonclassical dihydrogen adduct of S = 1/2 Fe(I). J Am Chem Soc. 2011; 133:16366–16369. [PubMed: 21954981]

40. Doan PE, Nelson MJ, Jin H, Hoffman BM. An Implicit TRIPLE Effect in Mims Pulsed ENDOR: A Sensitive New Technique for Determining Signs of Hyperfine Couplings. J. Am. Chem. Soc. 1996; 118:7014–7015.
41. Silakov A, Reijerse EJ, Albracht SP, Hatchikian EC, Lubitz W. The electronic structure of the H-cluster in the [FeFe]-hydrogenase from *Desulfovibrio desulfuricans*: a Q-band ^{57}Fe-ENDOR and HYSCORE study. J Am Chem Soc. 2007; 129:11447–11458. [PubMed: 17722921]
42. Bennebroek MT, Schmidt J. Pulsed ENDOR spectroscopy at large thermal spin polarizations and the absolute sign of the hyperfine interaction. J. Magn. Reson. 1997; 128:199–206.
43. Epel B, Manikandan P, Kroneck PMH, Goldfarb D. High-field ENDOR and the sign of the hyperfine coupling. Appl. Magn. Reson. 2001; 21:287–297.
44. Yang TC, Hoffman BM. A Davies/Hahn multi-sequence for studies of spin relaxation in pulsed ENDOR. J. Magn. Reson. 2006; 181:280–286. [PubMed: 16777447]
45. Doan PE. Combining steady-state and dynamic methods for determining absolute signs of hyperfine interactions: pulsed ENDOR Saturation and Recovery (PESTRE). J. Magn. Reson. 2011; 208:76–86. [PubMed: 21075026]
46. Doan PE, Telser J, Barney BM, Igarashi RY, Dean DR, Seefeldt LC, Hoffman BM. ^{57}Fe ENDOR spectroscopy and 'electron inventory' analysis of the nitrogenase E_4 intermediate suggest the metal-ion core of FeMo-cofactor cycles through only one redox couple. J Am Chem Soc. 2011; 133:17329–17340. [PubMed: 21980917]
47. Cowen J, Kaplan D. Spin-echo measurement of the spin-lattice and spin-spin relaxation in Ce^{3+} in lanthanum magnesium nitrate. Phys. Rev. 1961; 124:1098–1101.
48. Mims W, Nassau K, McGee J. Spectral diffusion in electron resonance lines. Phys. Rev. 1961; 123:2059–2069.
49. Rowan L, Hahn E, Mims W. Electron-spin-echo envelope modulation. Phys. Rev. 1965; 137:A61–A71.
50. McCracken, J. Encyclopedia of Inorganic Chemistry. John Wiley & Sons, Ltd; 2006. Electron Spin Echo Envelope Modulation (ESEEM) Spectroscopy.
51. Hahn E. Spin Echoes. Phys. Rev. 1950; 80:580–594.
52. Merks RPJ, De Beer R. Two-dimensional Fourier transform of electron spin echo envelope modulation. An alternative for ENDOR. J. Phys. Chem. 1979; 83:3319–3322.
53. Hofer P, Grupp A, Mehring M. High-resolution time-domain electron-nuclear-sublevel spectroscopy by pulsed coherence transfer. Phys. Rev. A. 1986; 33:3519–3522. [PubMed: 9897070]
54. Dikanov SA, Bowman MK. Cross-peak lineshape of two-dimensional ESEEM spectra in disordered $S = 1/2$, $I = 1/2$ spin systems. J. Magn. Reson. Ser. A. 1995; 116:125–128.
55. Dikanov SA, Xun L, Karpiel AB, Tyryshkin AM, Bowman MK. Orientationally-selected two-dimensional ESEEM spectroscopy of the Rieske-type iron–sulfur cluster in 2,4,5-trichlorophenoxyacetate monooxygenase from *Burkholderia cepacia* AC1100. J. Am. Chem. Soc. 1996; 118:8408–8416.
56. Madi ZL, Van Doorslaer S, Schweiger A. Numerical simulation of one- and two-dimensional ESEEM experiments. J. Magn. Reson. 2002; 154:181–191. [PubMed: 11846575]
57. Stoll S, Schweiger A. Rapid construction of solid-state magnetic resonance powder spectra from frequencies and amplitudes as applied to ESEEM. J. Magn. Reson. 2003; 163:248–256. [PubMed: 12914840]
58. Hoffman BM, Dean DR, Seefeldt LC. Climbing nitrogenase: toward a mechanism of enzymatic nitrogen fixation. Acc Chem Res. 2009; 42:609–619. [PubMed: 19267458]
59. Hoffman BM, Lukoyanov D, Dean DR, Seefeldt LC. Nitrogenase: a draft mechanism. Acc Chem Res. 2013; 46:587–595. [PubMed: 23289741]
60. Hoffman BM, Lukoyanov D, Yang ZY, Dean DR, Seefeldt LC. Mechanism of nitrogen fixation by nitrogenase: the next stage. Chem. Rev. 2014; 114:4041–4062. [PubMed: 24467365]
61. Lukoyanov D, Barney BM, Dean DR, Seefeldt LC, Hoffman BM. Connecting nitrogenase intermediates with the kinetic scheme for N_2 reduction by a relaxation protocol and identification of the N_2 binding state. Proc. Nat. Acad. Sci. 2007; 104:1451–1455. [PubMed: 17251348]

62. Lukoyanov D, Yang ZY, Barney BM, Dean DR, Seefeldt LC, Hoffman BM. Unification of reaction pathway and kinetic scheme for N_2 reduction catalyzed by nitrogenase. Proc. Nat. Acad. Sci. 2012; 109:5583–5587. [PubMed: 22460797]

63. Hendrich MP, Debrunner PG. Integer-spin electron paramagnetic resonance of iron proteins. Biophys J. 1989; 56:489–506. [PubMed: 2551404]

64. Munck E, Surerus KK, Hendrich MP. Combining Mössbauer spectroscopy with integer spin electron paramagnetic resonance. Methods Enzymol. 1993; 227:463–479. [PubMed: 8255233]

65. Hoffman BM. ENDOR and ESEEM of a non-Kramers doublet in an integer-spin system. Journal of Physical Chemistry. 1994; 98:11657–11665.

66. Hoffman BM, Sturgeon BE, Doan PE, DeRose VJ, Liu KE, Lippard SJ. ESEEM and ENDOR magnetic resonance studies of the non-Kramers doublet in the integer-spin diiron(II) forms of two methane monooxygenase hydroxylases and hemerythrin azide. J. Am. Chem. Soc. 1994; 116:6023–6024.

67. Sturgeon BE, Doan PE, Liu KE, Burdi D, Tong WH, Nocek JM, Gupta N, Stubbe J, Donald J, Kurtz M, Lippard SJ, Hoffman BM. Non-Kramers ESEEM of integer-spin diferrous carboxylate-bridged clusters in proteins. J. Am. Chem. Soc. 1997; 119:375–386.

68. Lancaster KM, Roemelt M, Ettenhuber P, Hu Y, Ribbe MW, Neese F, Bergmann U, DeBeer S. X-ray emission spectroscopy evidences a central carbon in the nitrogenase iron-molybdenum cofactor. Science. 2011; 334:974–977. [PubMed: 22096198]

69. Spatzal T, Aksoyoglu M, Zhang L, Andrade SL, Schleicher E, Weber S, Rees DC, Einsle O. Evidence for interstitial carbon in nitrogenase FeMo cofactor. Science. 2011; 334:940. [PubMed: 22096190]

70. Wiig JA, Hu Y, Lee CC, Ribbe MW. Radical SAM-dependent carbon insertion into the nitrogenase M-cluster. Science. 2012; 337:1672–1675. [PubMed: 23019652]

71. True AE, Nelson MJ, Venters RA, Orme-Johnson WH, Hoffman BM. ^{57}Fe hyperfine coupling tensors of the FeMo cluster in *Azotobacter vinelandii* MoFe protein: Determination by polycrystalline ENDOR spectroscopy. J. Am. Chem. Soc. 1988; 110:1935–1943.

72. Crouse BR, Meyer J, Johnson MK. Spectroscopic evidence for a reduced Fe_2S_2 cluster with a S = 9/2 ground state in mutant forms of *Clostridium pasteurianum* 2Fe ferredoxin. J. Am. Chem. Soc. 1995; 117:9612–9613.

73. Noodleman L, Norman JG, Osborne JH, Aizman A, Case DA. Models for ferredoxins: electronic structures of iron-sulfur clusters with one, two, and four iron atoms. J. Am. Chem. Soc. 1985; 107:3418–3426.

74. Mailer C, Taylor CP. Rapid adiabatic passage EPR of ferricytochrome c: signal enhancement and determination of the spin-lattice relaxation time. Biochim Biophys Acta. 1973; 322:195–203. [PubMed: 4358082]

75. Huynh BH, Kent TA. Mössbauer studies of iron proteins. Adv. Inorg. Biochem. 1984; 6:163–223. [PubMed: 6100155]

76. Kent TA, Dreyer JL, Kennedy MC, Huynh BH, Emptage MH, Beinert H, Munck E. Mössbauer studies of beef heart aconitase: evidence for facile interconversions of iron-sulfur clusters. Proc. Nat. Acad. Sci. 1982; 79:1096–1100. [PubMed: 6280166]

77. Long, GJ.; Grandjean, F. Mössbauer spectroscopy applied to inorganic chemistry. New York: Plenum Press; 1984.

78. Dicus MM, Conlan A, Nechushtai R, Jennings PA, Paddock ML, Britt RD, Stoll S. Binding of histidine in the (Cys)3(His)1-coordinated [2Fe-2S] cluster of human mitoNEET. J Am Chem Soc. 2010; 132:2037–2049. [PubMed: 20099820]

79. Gurbiel RJ, Doan PE, Gassner GT, Macke TJ, Case DA, Ohnishi T, Fee JA, Ballou DP, Hoffman BM. Active site structure of Rieske-type proteins: electron nuclear double resonance studies of isotopically labeled phthalate dioxygenase from *Pseudomonas cepacia* and Rieske protein from *Rhodobacter capsulatus* and molecular modeling studies of a Rieske center. Biochemistry. 1996; 35:7834–7845. [PubMed: 8672484]

80. Orio M, Mouesca JM. Variation of average g values and effective exchange coupling constants among [2Fe-2S] clusters: a density functional theory study of the impact of localization (trapping

forces) versus delocalization (double-exchange) as competing factors. Inorg. Chem. 2008; 47:5394–5416. [PubMed: 18491857]

81. Priem AH, Klaassen AA, Reijerse EJ, Meyer TE, Luchinat C, Capozzi F, Dunham WR, Hagen WR. EPR analysis of multiple forms of $[4Fe\text{-}4S]^{3+}$ clusters in HiPIPs. JBIC, J. Bio. Inorg. Chem. 2005; 10:417–424.
82. Grazina, R.; Pauleta, SR.; Moura, JJG.; Moura, I. Iron–sulfur centers: New roles for ancient metal sites. In: Poeppelmeier, JR., editor. Comprehensive Inorganic Chemistry II. Second Edition. Amsterdam: Elsevier; 2013. p. 103-148.
83. Belinskii M. Spin coupling model for tetrameric iron clusters in ferredoxins. I. Theory, exchange levels, g-factors. Chem. Phys. 1993; 172:189–211.
84. Johnson DC, Dean DR, Smith AD, Johnson MK. Structure, function, and formation of biological iron-sulfur clusters. Annu. Rev. Biochem. 2005; 74:247–281. [PubMed: 15952888]
85. Lee SC, Holm RH. Speculative synthetic chemistry and the nitrogenase problem. Proc. Nat. Acad. Sci. 2003; 100:3595–3600. [PubMed: 12642670]
86. Holm RH. Trinuclear cuboidal heterometallic cubane-type iron-sulfur clusters: New structural and reactivity themes in chemistry and biology. Adv. Inorg. Chem. 1992; 38:1–71.
87. Holm RH, Ciurli S, Weigel JA. Subsite-specific structures and reactions in native and Synthetic (4Fe-4S) cubane-type clusters. Prog. Inorg. Chem. 1990; 38:1–74.
88. Rius G, Lamotte B. Single-Crystal ENDOR Study of a ^{57}Fe-Enriched Iron-Sulfur $[Fe_4S_4]^{3+}$ Cluster. J. Am. Chem. Soc. 1989; 111:2464–2469.
89. Mouesca J-M, Rius G, Lamotte B. Single-crystal proton ENDOR studies of the $[Fe_4S_4]^{3+}$ cluster: Determination of the spin population distribution and proposal of a model to interpret the ^{1}H NMR paramagnetic shifts in high-potential ferredoxins. J. Am. Chem. Soc. 1993; 115:4714–4731.
90. Gloux J, Gloux P, Lamotte B, Mouesca J-M, Rius G. The Different $[Fe_4S_4]^{3+}$ and $[Fe_4S_4]^{+}$ Species Created by g Irradiation in Single Crystals of the $(Et_4N)_2[Fe_4S_4(SBenz)_4]$ Model Compound: Their EPR Description and Their Biological Significance. J. Am. Chem. Soc. 1994; 116:1953–1961.
91. Noodleman L, Case DA, Mouesca JM, Lamotte B. Valence electron delocalization in polynuclear iron-sulfur clusters. J. Biol. Inorg. Chem. 1996; 1:177–182.
92. Le Pape L, Lamotte B, Mouesca J-M, Rius G. Paramagnetic states of four iron–four sulfur clusters. 1. EPR single-crystal study of 3+ and 1+ clusters of an asymmetrical model compound and general model for the interpretation of the g-tensors of these two redox states. J. Am. Chem. Soc. 1997; 119:9757–9770.
93. Le Pape L, Lamotte B, Mouesca J-M, Rius G. Paramagnetic states of four iron–four sulfur clusters. 2. Proton ENDOR study of a 1+ state in an asymmetrical cluster. J. Am. Chem. Soc. 1997; 119:9771–9781.
94. Davydov R, Kappl R, Huttermann J, Peterson JA. EPR-spectroscopy of reduced oxyferrous-P450cam. FEBS Lett. 1991; 295:113–115. [PubMed: 1662641]
95. Dikanov SA, Davydov RM, Xun L, Bowman MK. CW and pulsed EPR characterization of the reduced Rieske type iron-sulfur center in 2,4,5-trichlorophenoxyacetate monoxygenase. J. Magn. Reson. 1996; 112:289–294.
96. Telser J, Davydov R, Kim CH, Adams MWW, Hoffman BM. Investigation of the unusual electronic structure of *Pyrococcus furiosus* 4Fe ferredoxin by EPR spectroscopy of protein reduced at ambient and cryogenic temperatures. Inorg. Chem. 1999; 38:3550–3553. [PubMed: 11671103]
97. Gloux J, Gloux P, Lamotte B, Rius a G. Creation and ESR identification, in single crystals, of synthetic analogs of the $S = (1/2)$ states of the Fe4S4 cores of the reduced ferredoxins and oxidized high-potential proteins. Phys Rev Lett. 1985; 54:599–602. [PubMed: 10031562]
98. Moriaud F, Gambarelli S, Lamotte B, Mouesca J-M. Detailed proton Q-band ENDOR study of the electron spin population distribution in the reduced $[4Fe\text{-}4S]^{1+}$ state. J. Phys. Chem. B. 2001; 105:9631–9642.
99. Thauer RK, Kaster AK, Seedorf H, Buckel W, Hedderich R. Methanogenic archaea: ecologically relevant differences in energy conservation. Nat. Rev. Microbiol. 2008; 6:579–591. [PubMed: 18587410]

100. Simianu M, Murakami E, Brewer JM, Ragsdale SW. Purification and properties of the heme- and iron-sulfur-containing heterodisulfide reductase from *Methanosarcina thermophila*. Biochemistry. 1998; 37:10027–10039. [PubMed: 9665708]

101. Hamann N, Mander GJ, Shokes JE, Scott RA, Bennati M, Hedderich R. A cysteine-rich CCG domain contains a novel [4Fe-4S] cluster binding motif as deduced from studies with subunit B of heterodisulfide reductase from *Methanothermobacter marburgensis*. Biochemistry. 2007; 46:12875–12885. [PubMed: 17929940]

102. Madadi-Kahkesh S, Duin EC, Heim S, Albracht SP, Johnson MK, Hedderich R. A paramagnetic species with unique EPR characteristics in the active site of heterodisulfide reductase from methanogenic archaea. Eur J Biochem. 2001; 268:2566–2577. [PubMed: 11322875]

103. Duin EC, Bauer C, Jaun B, Hedderich R. Coenzyme M binds to a [4Fe–4S] cluster in the active site of heterodisulfide reductase as deduced from EPR studies with the [^{33}S]coenzyme M-treated enzyme. FEBS Lett. 2003; 538:81–84. [PubMed: 12633857]

104. Duin EC, Madadi-Kahkesh S, Hedderich R, Clay MD, Johnson MK. Heterodisulfide reductase from *Methanothermobacter marburgensis* contains an active-site [4Fe–4S] cluster that is directly involved in mediating heterodisulfide reduction. FEBS Lett. 2002; 512:263–268. [PubMed: 11852093]

105. Bennati M, Weiden N, Dinse KP, Hedderich R. ^{57}Fe ENDOR spectroscopy on the iron-sulfur cluster involved in substrate reduction of heterodisulfide reductase. J Am Chem Soc. 2004; 126:8378–8379. [PubMed: 15237985]

106. Fielding AJ, Parey K, Ermler U, Scheller S, Jaun B, Bennati M. Advanced electron paramagnetic resonance on the catalytic iron-sulfur cluster bound to the CCG domain of heterodisulfide reductase and succinate: quinone reductase. JBIC, J. Bio. Inorg. Chem. 2013; 18:905–915.

107. Middleton P, Dickson DP, Johnson CE, Rush JD. Interpretation of the Mössbauer spectra of the high-potential iron protein from *Chromatium*. Eur J Biochem. 1980; 104:289–296. [PubMed: 6245869]

108. Lubitz W, Ogata H, Rudiger O, Reijerse E. Hydrogenases. Chem. Rev. 2014; 114:4081–4148. [PubMed: 24655035]

109. Peters JW, Lanzilotta WN, Lemon BJ, Seefeldt LC. X-ray crystal structure of the Fe-only hydrogenase (CpI) from *Clostridium pasteurianum* to 1.8 angstrom resolution. Science. 1998; 282:1853–1858. [PubMed: 9836629]

110. Nicolet Y, Piras C, Legrand P, Hatchikian CE, Fontecilla-Camps JC. *Desulfovibrio desulfuricans* iron hydrogenase: the structure shows unusual coordination to an active site Fe binuclear center. Structure. 1999; 7:13–23. [PubMed: 10368269]

111. Silakov A, Wenk B, Reijerse E, Albracht SP, Lubitz W. Spin distribution of the H-cluster in the H(ox)-CO state of the [FeFe] hydrogenase from *Desulfovibrio desulfuricans*: HYSCORE and ENDOR study of ^{14}N and ^{13}C nuclear interactions. JBIC, J. Bio. Inorg. Chem. 2009; 14:301–313.

112. Esselborn J, Lambertz C, Adamska-Venkatesh A, Simmons T, Berggren G, Noth J, Siebel J, Hemschemeier A, Artero V, Reijerse E, Fontecave M, Lubitz W, Happe T. Spontaneous activation of [FeFe]-hydrogenases by an inorganic [2Fe] active site mimic. Nat. Chem. Bio. 2013; 9:607–609. [PubMed: 23934246]

113. Berggren G, Adamska A, Lambertz C, Simmons TR, Esselborn J, Atta M, Gambarelli S, Mouesca JM, Reijerse E, Lubitz W, Happe T, Artero V, Fontecave M. Biomimetic assembly and activation of [FeFe]-hydrogenases. Nature. 2013; 499:66–69. [PubMed: 23803769]

114. Silakov A, Wenk B, Reijerse E, Lubitz W. ^{14}N HYSCORE investigation of the H-cluster of [FeFe] hydrogenase: evidence for a nitrogen in the dithiol bridge. Phys. Chem. Chem. Phys.: PCCP. 2009; 11:6592–6599.

115. Erdem OF, Schwartz L, Stein M, Silakov A, Kaur-Ghumaan S, Huang P, Ott S, Reijerse EJ, Lubitz W. A model of the [FeFe] hydrogenase active site with a biologically relevant azadithiolate bridge: a spectroscopic and theoretical investigation. Agnew. Chem. Int. Ed. Engl. 2011; 50:1439–1443.

116. Shepard EM, Mus F, Betz JN, Byer AS, Duffus BR, Peters JW, Broderick JB. [FeFe]-hydrogenase maturation. Biochemistry. 2014; 53:4090–4104. [PubMed: 24878200]

117. Kuchenreuther JM, Myers WK, Suess DL, Stich TA, Pelmenschikov V, Shiigi SA, Cramer SP, Swartz JR, Britt RD, George SJ. The HydG enzyme generates an $Fe(CO)_2(CN)$ synthon in assembly of the FeFe hydrogenase H-cluster. Science. 2014; 343:424–427. [PubMed: 24458644]
118. Kuchenreuther JM, Myers WK, Stich TA, George SJ, Nejatyjahromy Y, Swartz JR, Britt RD. A radical intermediate in tyrosine scission to the CO and CN^- ligands of FeFe hydrogenase. Science. 2013; 342:472–475. [PubMed: 24159045]
119. Kuchenreuther JM, Guo Y, Wang H, Myers WK, George SJ, Boyke CA, Yoda Y, Alp EE, Zhao J, Britt RD, Swartz JR, Cramer SP. Nuclear resonance vibrational spectroscopy and electron paramagnetic resonance spectroscopy of ^{57}Fe-enriched [FeFe] hydrogenase indicate stepwise assembly of the H-cluster. Biochemistry. 2013; 52:818–826. [PubMed: 23249091]
120. Berto P, Di Valentin M, Cendron L, Vallese F, Albertini M, Salvadori E, Giacometti GM, Carbonera D, Costantini P. The [4Fe-4S]-cluster coordination of [FeFe]-hydrogenase maturation protein HydF as revealed by EPR and HYSCORE spectroscopies. Biochim Biophys Acta. 2012; 1817:2149–2157. [PubMed: 22985598]
121. Stich TA, Myers WK, Britt RD. Paramagnetic intermediates generated by radical S-adenosylmethionine (SAM) enzymes. Acc Chem Res. 2014; 47:2235–2243. [PubMed: 24991701]
122. Simmons TR, Berggren G, Bacchi M, Fontecave M, Artero V. Mimicking hydrogenases: From biomimetics to artificial enzymes. Coord. Chem. Rev. 2014; 270–271:127–150.
123. Hsieh CH, Erdem OF, Harman SD, Singleton ML, Reijerse E, Lubitz W, Popescu CV, Reibenspies JH, Brothers SM, Hall MB, Darensbourg MY. Structural and spectroscopic features of mixed valent Fe(II)Fe(I) complexes and factors related to the rotated configuration of diiron hydrogenase. J Am Chem Soc. 2012; 134:13089–13102. [PubMed: 22774845]
124. Ogo S, Ichikawa K, Kishima T, Matsumoto T, Nakai H, Kusaka K, Ohhara T. A functional [NiFe]hydrogenase mimic that catalyzes electron and hydride transfer from H_2. Science. 2013; 339:682–684. [PubMed: 23393260]
125. Lubitz W, Reijerse E, van Gastel M. [NiFe] and [FeFe] hydrogenases studied by advanced magnetic resonance techniques. Chem. Rev. 2007; 107:4331–4365. [PubMed: 17845059]
126. Dos Santos PC, Igarashi RY, Lee HI, Hoffman BM, Seefeldt LC, Dean DR. Substrate interactions with the nitrogenase active site. Acc Chem Res. 2005; 38:208–214. [PubMed: 15766240]
127. Hoffman BM, Venters RA, Roberts JE, Nelson M, Orme-Johnson WH. ^{57}Fe ENDOR of the Nitrogenase MoFe Protein. J. Am. Chem. Soc. 1982; 104:4711–4712.
128. Venters RA, Nelson MJ, Mclean PA, True AE, Levy MA, Hoffman BM, Orme-Johnson WH. ENDOR of the resting state of nitrogenase molybdenum iron proteins from *Azotobacter-vinelandii, Klebsiella-pneumoniae*, and *Clostridium-pasteurianum* - ^{1}H, ^{57}Fe, ^{95}Mo, and ^{33}S studies. J. Am. Chem. Soc. 1986; 108:3487–3498.
129. True AE, Nelson MJ, Venters RA, Orme-Johnson WH, Hoffman BM. ^{57}Fe hyperfine coupling tensors of the FeMo cluster in *Azotobacter vinelandii* MoFe protein: determination by polycrystalline ENDOR spectroscopy. J. Am. Chem. Soc. 1988; 110:1935–1943.
130. Yoo SJ, Angove HC, Papaefthymiou V, Burgess BK, Münck E. Mössbauer study of the MoFe protein of nitrogenase from *Azotobacter vinelandii* using selective ^{57}Fe enrichment of the M-Centers. J. Am. Chem. Soc. 2000; 122:4926–4936.
131. Pollock RC, Lee H-I, Cameron LM, DeRose VJ, Hales BJ, Orme-Johnson WH, Hoffman BM. Investigation of CO bound to inhibited forms of nitrogenase MoFe protein by ^{13}C ENDOR. J. Am. Chem. Soc. 1995; 117:8686–8687.
132. Christie PD, Lee HI, Cameron LM, Hales BJ, OrmeJohnson WH, Hoffman BM. Identification of the CO-binding cluster in nitrogenase MoFe protein by ENDOR of Fe-57 isotopomers. J. Am. Chem. Soc. 1996; 118:8707–8709.
133. Thorneley RNF, Lowe DJ. Nitrogenase: substrate binding and activation. JBIC, J. Bio. Inorg. Chem. 1996; 1:576–580.
134. Igarashi RY, Laryukhin M, Dos Santos PC, Lee HI, Dean DR, Seefeldt LC, Hoffman BM. Trapping H^- bound to the nitrogenase FeMo-cofactor active site during H_2 evolution: characterization by ENDOR spectroscopy. J Am Chem Soc. 2005; 127:6231–6241. [PubMed: 15853328]

135. Lukoyanov D, Yang ZY, Dean DR, Seefeldt LC, Hoffman BM. Is Mo involved in hydride binding by the four-electron reduced (E_4) intermediate of the nitrogenase MoFe protein? J Am Chem Soc. 2010; 132:2526–2527. [PubMed: 20121157]
136. Shaw S, Lukoyanov D, Danyal K, Dean DR, Hoffman BM, Seefeldt LC. Nitrite and hydroxylamine as nitrogenase substrates: mechanistic implications for the pathway of N_2 reduction. J Am Chem Soc. 2014; 136:12776–12783. [PubMed: 25136926]
137. Werst MM, Kennedy MC, Houseman ALP, Beinert H, Hoffman BM. Characterization of the iron-sulfur $[4Fe\text{-}4S]^+$ cluster at the active site of aconitase by ^{57}Fe, ^{33}S, and ^{14}N electron nuclear double resonance spectroscopy. Biochemistry. 1990; 29:10533–10540. [PubMed: 2271662]
138. Robbins AH, Stout CD. Structure of activated aconitase: formation of the [4Fe-4S] cluster in the crystal. Proc. Nat. Acad. Sci. 1989; 86:3639–3643. [PubMed: 2726740]
139. Orme-Johnson WH, Hansen RE, Beinert H, Tsibris JC, Bartholomaus RC, Gunsalus IC. On the sulfur components of iron-sulfur proteins. I. The number of acid-labile sulfur groups sharing an unpaired electron with iron. Proc. Nat. Acad. Sci. 1968; 60:368–372. [PubMed: 4302637]
140. Meyer J. Ferredoxins of the third kind. FEBS Lett. 2001; 509:1–5. [PubMed: 11734195]
141. Meyer J. The evolution of ferredoxins. Trends Ecol Evol. 1988; 3:222–226. [PubMed: 21227235]
142. Hearshen DO, Hagen WR, Sands RH, Grande HJ, Crespi HL, Gunsalus IC, Dunham WR. An analysis of g strain in the EPR of two [2Fe–2S] ferredoxins. Evidence for a protein rigidity model. J. Magn. Reson. 1986; 69:440–459.
143. Yeh AP, Ambroggio XI, Andrade SL, Einsle O, Chatelet C, Meyer J, Rees DC. High resolution crystal structures of the wild type and Cys-55→Ser and Cys-59→Ser variants of the thioredoxin-like [2Fe-2S] ferredoxin from *Aquifex aeolicus*. J. Bio. Chem. 2002; 277:34499–34507. [PubMed: 12089152]
144. Li H, Mapolelo DT, Dingra NN, Naik SG, Lees NS, Hoffman BM, Riggs-Gelasco PJ, Huynh BH, Johnson MK, Outten CE. The yeast iron regulatory proteins Grx3/4 and Fra2 form heterodimeric complexes containing a [2Fe-2S] cluster with cysteinyl and histidyl ligation. Biochemistry. 2009; 48:9569–9581. [PubMed: 19715344]
145. Paddock ML, Wiley SE, Axelrod HL, Cohen AE, Roy M, Abresch EC, Capraro D, Murphy AN, Nechushtai R, Dixon JE, Jennings PA. MitoNEET is a uniquely folded 2Fe 2S outer mitochondrial membrane protein stabilized by pioglitazone. Proc. Nat. Acad. Sci. 2007; 104:14342–14347. [PubMed: 17766440]
146. Colca JR, McDonald WG, Waldon DJ, Leone JW, Lull JM, Bannow CA, Lund ET, Mathews WR. Identification of a novel mitochondrial protein ("mitoNEET") cross-linked specifically by a thiazolidinedione photoprobe. Am J Physiol Endocrinol Metab. 2004; 286:E252–E260. [PubMed: 14570702]
147. Wiley SE, Murphy AN, Ross SA, van der Geer P, Dixon JE. MitoNEET is an iron-containing outer mitochondrial membrane protein that regulates oxidative capacity. Proc. Nat. Acad. Sci. 2007; 104:5318–5323. [PubMed: 17376863]
148. Bertrand P, Gayda JP, Fee JA, Kuila D, Cammack R. Comparison of the spin-lattice relaxation properties of the two classes of [2Fe-2S] clusters in proteins. Biochim Biophys Acta. 1987; 916:24–28. [PubMed: 2822125]
149. Bowman MK, Berry EA, Roberts AG, Kramer DM. Orientation of the g-tensor axes of the Rieske subunit in the cytochrome bc1 complex. Biochemistry. 2004; 43:430–436. [PubMed: 14717597]
150. Fee JA, Findling KL, Yoshida T, Hille R, Tarr GE, Hearshen DO, Dunham WR, Day EP, Kent TA, Munck E. Purification and characterization of the Rieske iron-sulfur protein from *Thermus thermophilus*. Evidence for a [2Fe-2S] cluster having non-cysteine ligands. J. Bio. Chem. 1984; 259:124–133. [PubMed: 6323399]
151. Kappl R, Ebelshäuser M, Hannemann F, Bernhardt R, Hüttermann J. Probing electronic and structural properties of the reduced [2Fe–2S] cluster by orientation-selective ^1H ENDOR spectroscopy: Adrenodoxin versus Rieske iron-sulfur protein. Appl. Magn. Reson. 2006; 30:427–459.
152. Kolling DR, Samoilova RI, Shubin AA, Crofts AR, Dikanov SA. Proton environment of reduced Rieske iron-sulfur cluster probed by two-dimensional ESEEM spectroscopy. J. Phys. Chem. A. 2009; 113:653–667. [PubMed: 19099453]

153. Fugate CJ, Stich TA, Kim EG, Myers WK, Britt RD, Jarrett JT. 9-Mercaptodethiobiotin is generated as a ligand to the [2Fe-2S]+ cluster during the reaction catalyzed by biotin synthase from *Escherichia coli*. J Am Chem Soc. 2012; 134:9042–9045. [PubMed: 22607542]

154. Fugate CJ, Jarrett JT. Biotin synthase: insights into radical-mediated carbon-sulfur bond formation. Biochim Biophys Acta. 2012; 1824:1213–1222. [PubMed: 22326745]

155. Berkovitch F, Nicolet Y, Wan JT, Jarrett JT, Drennan CL. Crystal structure of biotin synthase, an S-adenosylmethionine-dependent radical enzyme. Science. 2004; 303:76–79. [PubMed: 14704425]

156. Taylor AM, Stoll S, Britt RD, Jarrett JT. Reduction of the [2Fe-2S] cluster accompanies formation of the intermediate 9-mercaptodethiobiotin in *Escherichia coli* biotin synthase. Biochemistry. 2011; 50:7953–7963. [PubMed: 21859080]

157. Rieske JS, MacLennan DH, Coleman R. Isolation and properties of an iron-protein from the (reduced coenzyme Q)-cytochrome C reductase complex of the respiratory chain. Biochem. Biophys. Res. Commun. 1964; 15:338–344.

158. Gibson JF, Hall DO, Thornley JH, Whatley FR. The iron complex in spinach ferredoxin. Proc. Nat. Acad. Sci. 1966; 56:987–990. [PubMed: 4291228]

159. Mims W. Envelope Modulation in Spin-Echo Experiments. Physical Review B. 1972; 5:2409–2419.

160. Beinert H, Kennedy MC, Stout CD. Aconitase as iron–sulfur protein, enzyme, and iron-regulatory protein. Chemical Reviews. 1996; 96:2335–2374. [PubMed: 11848830]

161. Telser J, Emptage MH, Merkle H, Kennedy MC, Beinert H, Hoffman BM. ^{17}O electron nuclear double resonance characterization of substrate binding to the $[4Fe\text{-}4S]^{1+}$ cluster of reduced active aconitase. J. Bio. Chem. 1986; 261:4840–4846. [PubMed: 3007476]

162. Kennedy MC, Werst M, Telser J, Emptage MH, Beinert H, Hoffman BM. Mode of substrate carboxyl binding to the $[4Fe\text{-}4S]^{+}$ cluster of reduced aconitase as studied by ^{17}O and ^{13}C electron-nuclear double resonance spectroscopy. Proc. Nat. Acad. Sci. 1987; 84:8854–8858. [PubMed: 3480514]

163. Werst MM, Kennedy MC, Beinert H, Hoffman BM. ^{17}O, ^{1}H, and ^{2}H electron nuclear double resonance characterization of solvent, substrate, and inhibitor binding to the $[4Fe\text{-}4S]^{+}$ cluster of aconitase. Biochemistry. 1990; 29:10526–10532. [PubMed: 2176871]

164. Kent TA, Emptage MH, Merkle H, Kennedy MC, Beinert H, Munck E. Mössbauer studies of aconitase. Substrate and inhibitor binding, reaction intermediates, and hyperfine interactions of reduced 3Fe and 4Fe clusters. J. Bio. Chem. 1985; 260:6871–6881. [PubMed: 2987236]

165. Robbins AH, Stout CD. The structure of aconitase. Proteins. 1989; 5:289–312. [PubMed: 2798408]

166. Barney BM, Yang TC, Igarashi RY, Dos Santos PC, Laryukhin M, Lee HI, Hoffman BM, Dean DR, Seefeldt LC. Intermediates trapped during nitrogenase reduction of N triple bond N, CH_3-N=NH, and H_2N-NH_2. J Am Chem Soc. 2005; 127:14960–14961. [PubMed: 16248599]

167. Lukoyanov D, Pelmenschikov V, Maeser N, Laryukhin M, Yang TC, Noodleman L, Dean DR, Case DA, Seefeldt LC, Hoffman BM. Testing if the interstitial atom, X, of the nitrogenase molybdenum-iron cofactor is N or C: ENDOR, ESEEM, and DFT studies of the $S = 3/2$ resting state in multiple environments. Inorg. Chem. 2007; 46:11437–11449. [PubMed: 18027933]

168. Seefeldt LC, Hoffman BM, Dean DR. Mechanism of Mo-dependent nitrogenase. Annu. Rev. Biochem. 2009; 78:701–722. [PubMed: 19489731]

169. Walsby CJ, Ortillo D, Yang J, Nnyepi MR, Broderick WE, Hoffman BM, Broderick JB. Spectroscopic approaches to elucidating novel iron-sulfur chemistry in the "radical-SAM" protein superfamily. Inorg. Chem. 2005; 44:727–741. [PubMed: 15859242]

170. Lees NS, Chen D, Walsby CJ, Behshad E, Frey PA, Hoffman BM. How an enzyme tames reactive intermediates: positioning of the active-site components of lysine 2,3-aminomutase during enzymatic turnover as determined by ENDOR spectroscopy. J Am Chem Soc. 2006; 128:10145–10154. [PubMed: 16881644]

171. Flint DH, Allen RM. Iron–Sulfur Proteins with Nonredox Functions. Chemical Reviews. 1996; 96:2315–2334. [PubMed: 11848829]

172. Frey PA. Travels with carbon-centered radicals. 5'-deoxyadenosine and 5'-deoxyadenosine-5'-yl in radical enzymology. Acc Chem Res. 2014; 47:540–549. [PubMed: 24308628]

173. Frey PA, Hegeman AD, Ruzicka FJ. The Radical SAM Superfamily. Crit Rev Biochem Mol Biol. 2008; 43:63–88. [PubMed: 18307109]

174. Broderick JB. Biochemistry: A radically different enzyme. Nature. 2010; 465:877–878. [PubMed: 20559373]

175. Zhang Q, van der Donk WA, Liu W. Radical-mediated enzymatic methylation: a tale of two SAMS. Acc Chem Res. 2012; 45:555–564. [PubMed: 22097883]

176. Duschene KS, Veneziano SE, Silver SC, Broderick JB. Control of radical chemistry in the AdoMet radical enzymes. Curr Opin Chem Biol. 2009; 13:74–83. [PubMed: 19269883]

177. Layer G, Heinz DW, Jahn D, Schubert WD. Structure and function of radical SAM enzymes. Curr Opin Chem Biol. 2004; 8:468–476. [PubMed: 15450488]

178. Hutcheson RU, Broderick JB. Radical SAM enzymes in methylation and methylthiolation. Metallomics. 2012; 4:1149–1154. [PubMed: 22992596]

179. Wang SC, Frey PA. S-adenosylmethionine as an oxidant: the radical SAM superfamily. Trens. Biochem. Sci. 2007; 32:101–110.

180. Cheek J, Broderick JB. Adenosylmethionine-dependent iron-sulfur enzymes: versatile clusters in a radical new role. JBIC, J. Bio. Inorg. Chem. 2001; 6:209–226.

181. Walsby CJ, Hong W, Broderick WE, Cheek J, Ortillo D, Broderick JB, Hoffman BM. Electron-nuclear double resonance spectroscopic evidence that S-adenosylmethionine binds in contact with the catalytically active $[4Fe–4S]^{+}$ cluster of Pyruvate Formate-Lyase Activating Enzyme. J. Am. Chem. Soc. 2002; 124:3143–3151. [PubMed: 11902903]

182. Walsby CJ, Ortillo D, Broderick WE, Broderick JB, Hoffman BM. An anchoring role for FeS clusters: Chelation of the amino acid moiety of S-adenosylmethionine to the unique iron site of the [4Fe–4S] cluster of Pyruvate Formate-Lyase Activating Enzyme. J. Am. Chem. Soc. 2002; 124:11270–11271. [PubMed: 12236732]

183. Hanzelmann P, Schindelin H. Crystal structure of the S-adenosylmethionine-dependent enzyme MoaA and its implications for molybdenum cofactor deficiency in humans. Proc. Nat. Acad. Sci. 2004; 101:12870–12875. [PubMed: 15317939]

184. Lepore BW, Ruzicka FJ, Frey PA, Ringe D. The x-ray crystal structure of lysine-2,3-aminomutase from *Clostridium subterminale*. Proc. Nat. Acad. Sci. 2005; 102:13819–13824. [PubMed: 16166264]

185. Wang W, Wang K, Li J, Nellutla S, Smirnova TI, Oldfield E. An ENDOR and HYSCORE investigation of a reaction intermediate in IspG (GcpE) catalysis. J Am Chem Soc. 2011; 133:8400–8403. [PubMed: 21574560]

186. Wuebbens MM, Rajagopalan KV. Investigation of the early steps of molybdopterin biosynthesis in *Escherichia coli* through the use of in-vivo labeling studies. J. Bio. Chem. 1995; 270:1082–1087. [PubMed: 7836363]

187. Hanzelmann P, Schindelin H. Binding of 5'-GTP to the C-terminal FeS cluster of the radical S-adenosylmethionine enzyme MoaA provides insights into its mechanism. Proc. Nat. Acad. Sci. 2006; 103:6829–6834. [PubMed: 16632608]

188. Lees NS, Hanzelmann P, Hernandez HL, Subramanian S, Schindelin H, Johnson MK, Hoffman BM. ENDOR spectroscopy shows that guanine N1 binds to [4Fe-4S] cluster II of the S-adenosylmethionine-dependent enzyme MoaA: mechanistic implications. J Am Chem Soc. 2009; 131:9184–9185. [PubMed: 19566093]

189. Cosper MM, Jameson GN, Davydov R, Eidsness MK, Hoffman BM, Huynh BH, Johnson MK. The $[4Fe\text{-}4S]^{2+}$ cluster in reconstituted biotin synthase binds S-adenosyl-L-methionine. J Am Chem Soc. 2002; 124:14006–14007. [PubMed: 12440894]

190. Sanyal I, Gibson KJ, Flint DH. *Escherichia coli* biotin synthase: an investigation into the factors required for its activity and its sulfur donor. Arch. Biochem. Biophys. 1996; 326:48–56. [PubMed: 8579371]

191. Bui BT, Florentin D, Fournier F, Ploux O, Méjean A, Marquet A. Biotin synthase mechanism: on the origin of sulphur. FEBS Lett. 1998; 440:226–230. [PubMed: 9862460]

192. Tse Sum Bui B, Mattioli TA, Florentin D, Bolbach G, Marquet A. *Escherichia coli* biotin synthase produces selenobiotin. Further evidence of the involvement of the $[2Fe\text{-}2S]^{2+}$ cluster in the sulfur insertion step. Biochemistry. 2006; 45:3824–3834. [PubMed: 16533066]

193. Pierrel F, Bjork GR, Fontecave M, Atta M. Enzymatic modification of tRNAs: MiaB is an iron-sulfur protein. J. Bio. Chem. 2002; 277:13367–13370. [PubMed: 11882645]

194. Pierrel F, Douki T, Fontecave M, Atta M. MiaB protein is a bifunctional radical-S-adenosylmethionine enzyme involved in thiolation and methylation of tRNA. J. Bio. Chem. 2004; 279:47555–47563. [PubMed: 15339930]

195. Hernandez HL, Pierrel F, Elleingand E, Garcia-Serres R, Huynh BH, Johnson MK, Fontecave M, Atta M. MiaB, a bifunctional radical-S-adenosylmethionine enzyme involved in the thiolation and methylation of tRNA, contains two essential [4Fe-4S] clusters. Biochemistry. 2007; 46:5140–5147. [PubMed: 17407324]

196. Boutigny S, Saini A, Baidoo EE, Yeung N, Keasling JD, Butland G. Physical and functional interactions of a monothiol glutaredoxin and an iron sulfur cluster carrier protein with the sulfur-donating radical S-adenosyl-L-methionine enzyme MiaB. J. Bio. Chem. 2013; 288:14200–14211. [PubMed: 23543739]

197. Molle T, Arragain S, Garcia R, Clemancey M, Latour J, Fontecave M, Mulliez E, Atta M, Gambarelli S, Mouesca J, Fontecave M, Kieffer-Jaquinot S, Forouhar F, Hunt JF. Sulfur insertion in biology by radical mechanism : Study of methylthiotransferases RimO and MiaB. JBIC, J. Bio. Inorg. Chem. 2014; 19:S251–S251.

198. Landgraf BJ, Arcinas AJ, Lee KH, Booker SJ. Identification of an intermediate methyl carrier in the radical S-adenosylmethionine methylthiotransferases RimO and MiaB. J Am Chem Soc. 2013; 135:15404–15416. [PubMed: 23991893]

199. Forouhar F, Arragain S, Atta M, Gambarelli S, Mouesca JM, Hussain M, Xiao R, Kieffer-Jaquinod S, Seetharaman J, Acton TB, Montelione GT, Mulliez E, Hunt JF, Fontecave M. Two Fe-S clusters catalyze sulfur insertion by radical-SAM methylthiotransferases. Nat. Chem. Bio. 2013; 9:333–338. [PubMed: 23542644]

200. Lee HI, Igarashi RY, Laryukhin M, Doan PE, Dos Santos PC, Dean DR, Seefeldt LC, Hoffman BM. An organometallic intermediate during alkyne reduction by nitrogenase. J Am Chem Soc. 2004; 126:9563–9569. [PubMed: 15291559]

201. Dance I. The mechanism of nitrogenase. Computed details of the site and geometry of binding of alkyne and alkene substrates and intermediates. J Am Chem Soc. 2004; 126:11852–11863. [PubMed: 15382920]

202. Rohmer M. The discovery of a mevalonate-independent pathway for isoprenoid biosynthesis in bacteria, algae and higher plants. Nat Prod Rep. 1999; 16:565–574. [PubMed: 10584331]

203. Eisenreich W, Bacher A, Arigoni D, Rohdich F. Biosynthesis of isoprenoids via the non-mevalonate pathway. Cell Mol Life Sci. 2004; 61:1401–1426. [PubMed: 15197467]

204. Rohdich F, Bacher A, Eisenreich W. Isoprenoid biosynthetic pathways as anti-infective drug targets. Biochem Soc Trans. 2005; 33:785–791. [PubMed: 16042599]

205. Oldfield E. Targeting isoprenoid biosynthesis for drug discovery: bench to bedside. Acc Chem Res. 2010; 43:1216–1226. [PubMed: 20560544]

206. Kollas AK, Duin EC, Eberl M, Altincicek B, Hintz M, Reichenberg A, Henschker D, Henne A, Steinbrecher I, Ostrovsky DN, Hedderich R, Beck E, Jomaa H, Wiesner J. Functional characterization of GcpE, an essential enzyme of the non-mevalonate pathway of isoprenoid biosynthesis. FEBS Lett. 2002; 532:432–436. [PubMed: 12482607]

207. Adedeji D, Hernandez H, Wiesner J, Kohler U, Jomaa H, Duin EC. Possible direct involvement of the active-site [4Fe-4S] cluster of the GcpE enzyme from *Thermus thermophilus* in the conversion of MEcPP. FEBS Lett. 2007; 581:279–283. [PubMed: 17214985]

208. Altincicek B, Duin EC, Reichenberg A, Hedderich R, Kollas AK, Hintz M, Wagner S, Wiesner J, Beck E, Jomaa H. LytB protein catalyzes the terminal step of the 2-C-methyl-D-erythritol-4-phosphate pathway of isoprenoid biosynthesis. FEBS Lett. 2002; 532:437–440. [PubMed: 12482608]

209. Wang W, Li J, Wang K, Huang C, Zhang Y, Oldfield E. Organometallic mechanism of action and inhibition of the 4Fe-4S isoprenoid biosynthesis protein GcpE (IspG). Proc. Nat. Acad. Sci. 2010; 107:11189–11193. [PubMed: 20534554]

210. Xu W, Lees NS, Adedeji D, Wiesner J, Jomaa H, Hoffman BM, Duin EC. Paramagnetic intermediates of (E)-4-hydroxy-3-methylbut-2-enyl diphosphate synthase (GcpE/IspG) under steady-state and pre-steady-state conditions. J Am Chem Soc. 2010; 132:14509–14520. [PubMed: 20863107]

211. Wang W, Wang K, Liu YL, No JH, Li J, Nilges MJ, Oldfield E. Bioorganometallic mechanism of action, and inhibition, of IspH. Proc. Nat. Acad. Sci. 2010; 107:4522–4527. [PubMed: 20173096]

212. Wolff M, Seemann M, Tse Sum Bui B, Frapart Y, Tritsch D, Estrabot AG, Rodr guez-Concepción M, Boronat A, Marquet A, Rohmer M. Isoprenoid biosynthesis via the methylerythritol phosphate pathway: the (E)-4-hydroxy-3-methylbut-2-enyl diphosphate reductase (LytB/IspH) from *Escherichia coli* is a [4Fe–4S] protein. FEBS Lett. 2003; 541:115–120. [PubMed: 12706830]

213. Wang K, Wang W, No JH, Zhang Y, Zhang Y, Oldfield E. Inhibition of the Fe_4S_4-cluster-containing protein IspH (LytB): electron paramagnetic resonance, metallacycles, and mechanisms. J Am Chem Soc. 2010; 132:6719–6727. [PubMed: 20426416]

214. Xu W, Lees NS, Hall D, Welideniya D, Hoffman BM, Duin EC. A closer look at the spectroscopic properties of possible reaction intermediates in wild-type and mutant (E)-4-hydroxyl-3-methylbut-2-enyl diphosphate reductase. Biochemistry. 2012; 51:4835–4849. [PubMed: 22646150]

215. Wang W, Wang K, Span I, Jauch J, Bacher A, Groll M, Oldfield E. Are free radicals involved in IspH catalysis? An EPR and crystallographic investigation. J Am Chem Soc. 2012; 134:11225–11234. [PubMed: 22687151]

216. Li J, Wang K, Smirnova TI, Khade RL, Zhang Y, Oldfield E. Isoprenoid biosynthesis: ferraoxetane or allyl anion mechanism for IspH catalysis? Agnew. Chem. Int. Ed. Engl. 2013; 52:6522–6525.

217. Span I, Grawert T, Bacher A, Eisenreich W, Groll M. Crystal structures of mutant IspH proteins reveal a rotation of the substrate's hydroxymethyl group during catalysis. J Mol Biol. 2012; 416:1–9. [PubMed: 22137895]

218. Span I, Wang K, Eisenreich W, Bacher A, Zhang Y, Oldfield E, Groll M. Insights into the binding of pyridines to the iron-sulfur enzyme IspH. J Am Chem Soc. 2014; 136:7926–7932. [PubMed: 24813236]

219. Span I, Wang K, Wang W, Zhang Y, Bacher A, Eisenreich W, Li K, Schulz C, Oldfield E, Groll M. Discovery of acetylene hydratase activity of the iron-sulphur protein IspH. Nat. Comm. 2012; 3:1042.

HIGHLIGHTS

- Background and applications of advanced EPR techniques relevant to FeS proteins
- Fundamental principles of advanced EPR: ENDOR, ESEEM, and HYSCORE
- Mechanistic and structural information on FeS clusters and proteins through EPR
- Variety of case studies: ferredoxins, radical SAM enzymes, nitrogenase and more

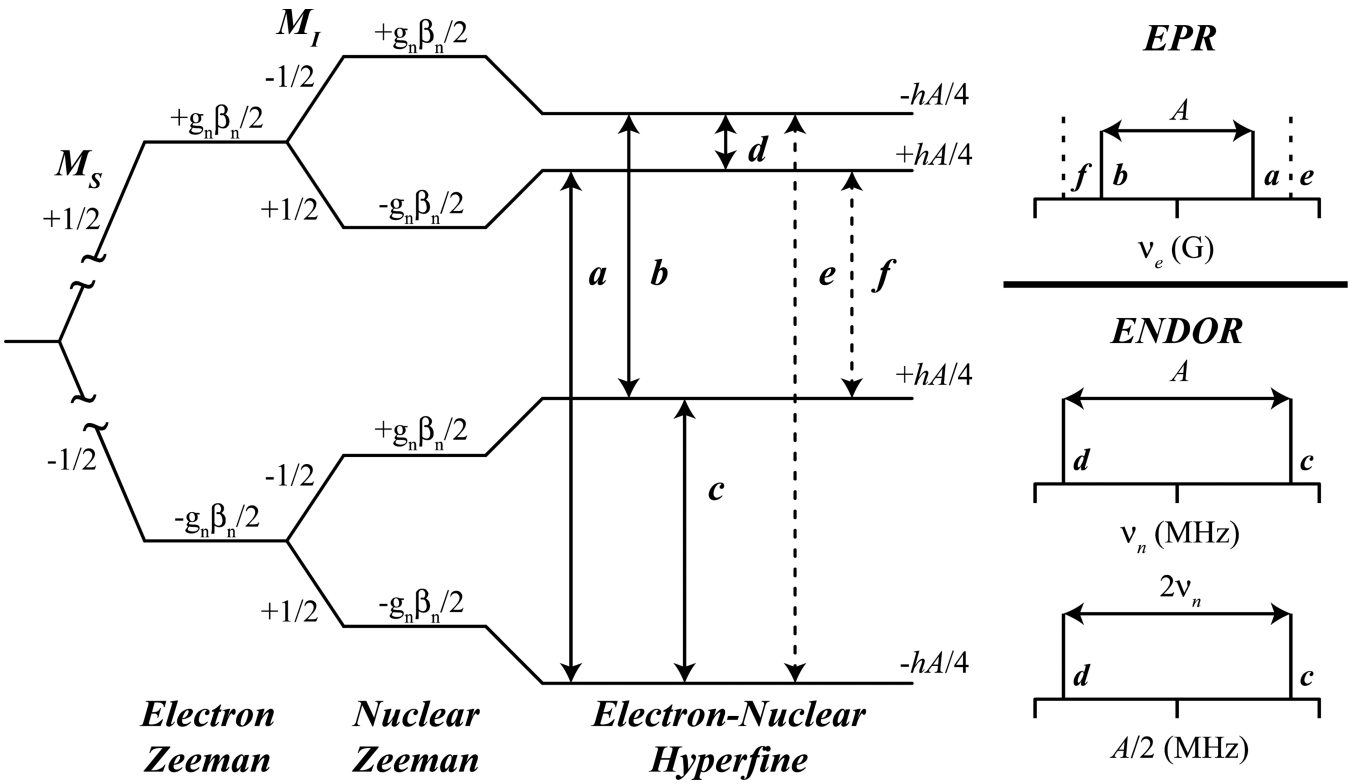

Figure 1.

Energy level diagram derived from the nuclear spin Hamiltonian (Eq 1) for a $S = 1/2$, $I = 1/2$ system. Solid lines represent allowed EPR (*a*, *b*) and ENDOR/ESEEM (*c*, *d*) transitions and dashed lines represent forbidden EPR (*e*, *f*) transitions. The stick representations (right) display the transition observed for EPR spectra (top) and for ENDOR spectra in 'weak' ν_n centered (middle) and 'strong' $A/2$ centered (bottom) coupling patterns.

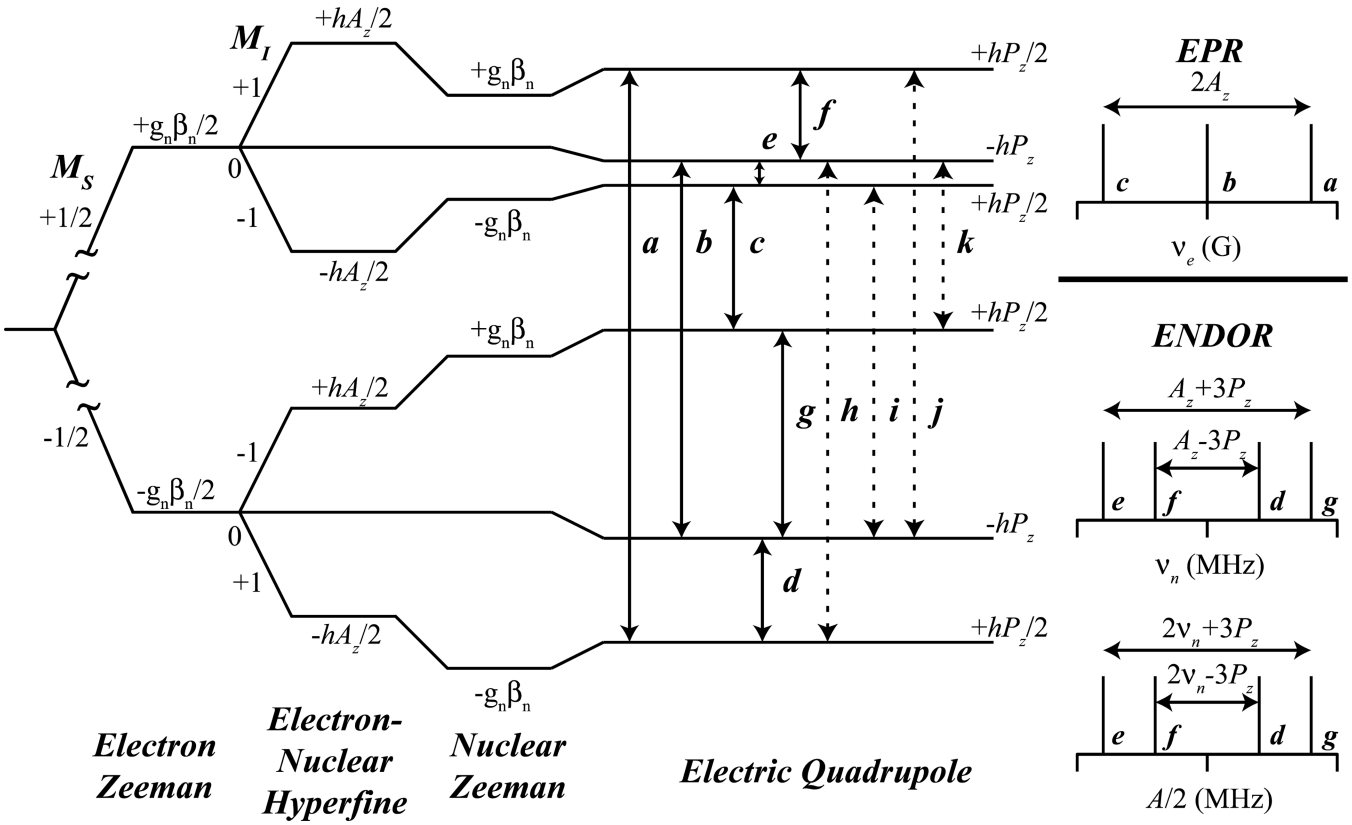

Figure 2.

Energy level diagram derived from the nuclear spin Hamiltonian (Eq. 1) for a $S = 1/2$, $I = 1$ system with an axial quadrupole tensor along the z axis. Solid lines represent allowed EPR (a, b, c) and ENDOR/ESEEM (d, e, f, g) and dashed lines represent semi-forbidden ESEEM (h, i, j, k) transitions.

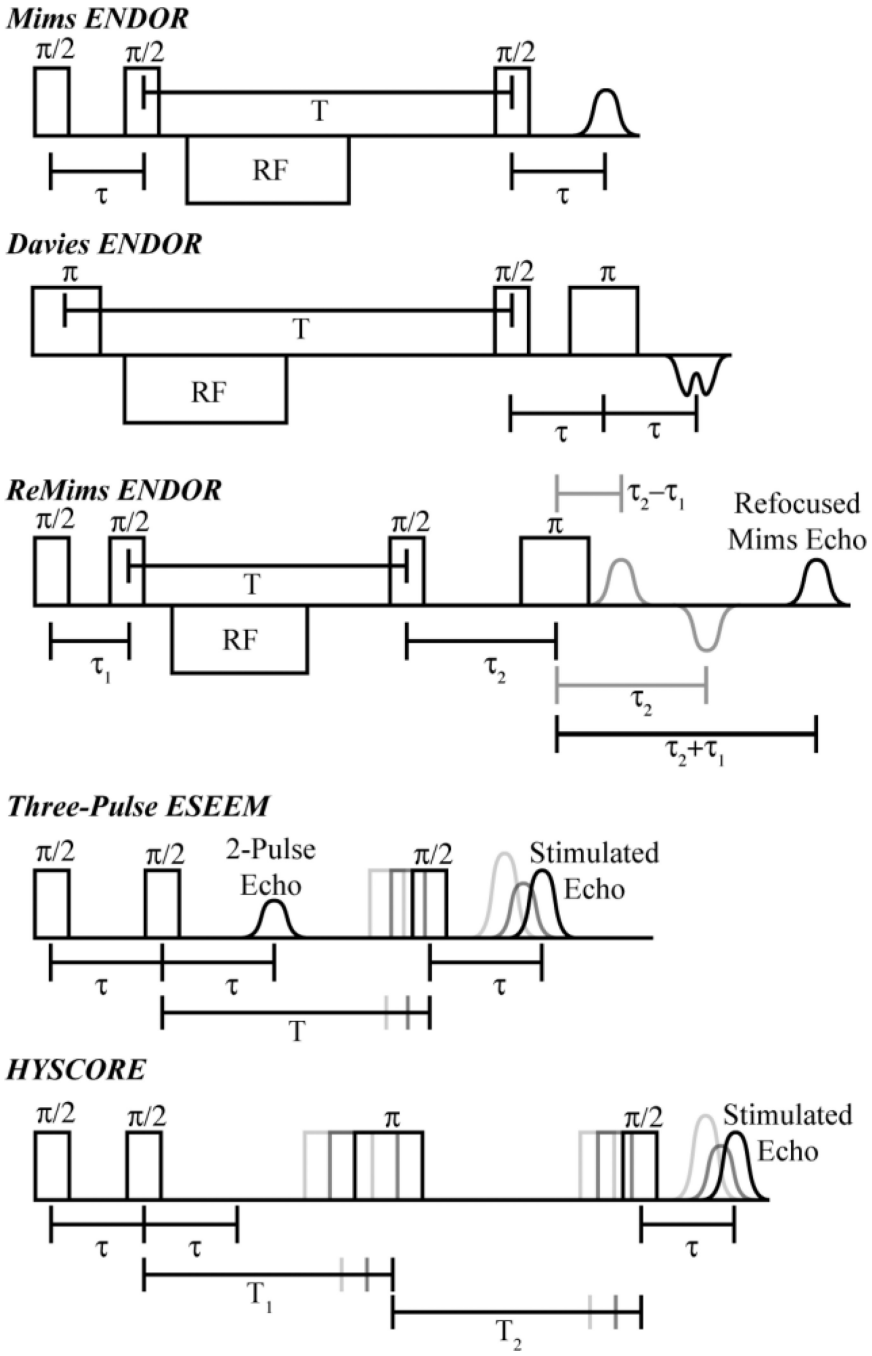

Figure 3.

Schematic representations of the Mims, Davies, and ReMims ENDOR pulse sequences, the three pulse ESEEM sequence, and the Hyperfine Sublevel Correlation (HYSCORE) pulse sequence.

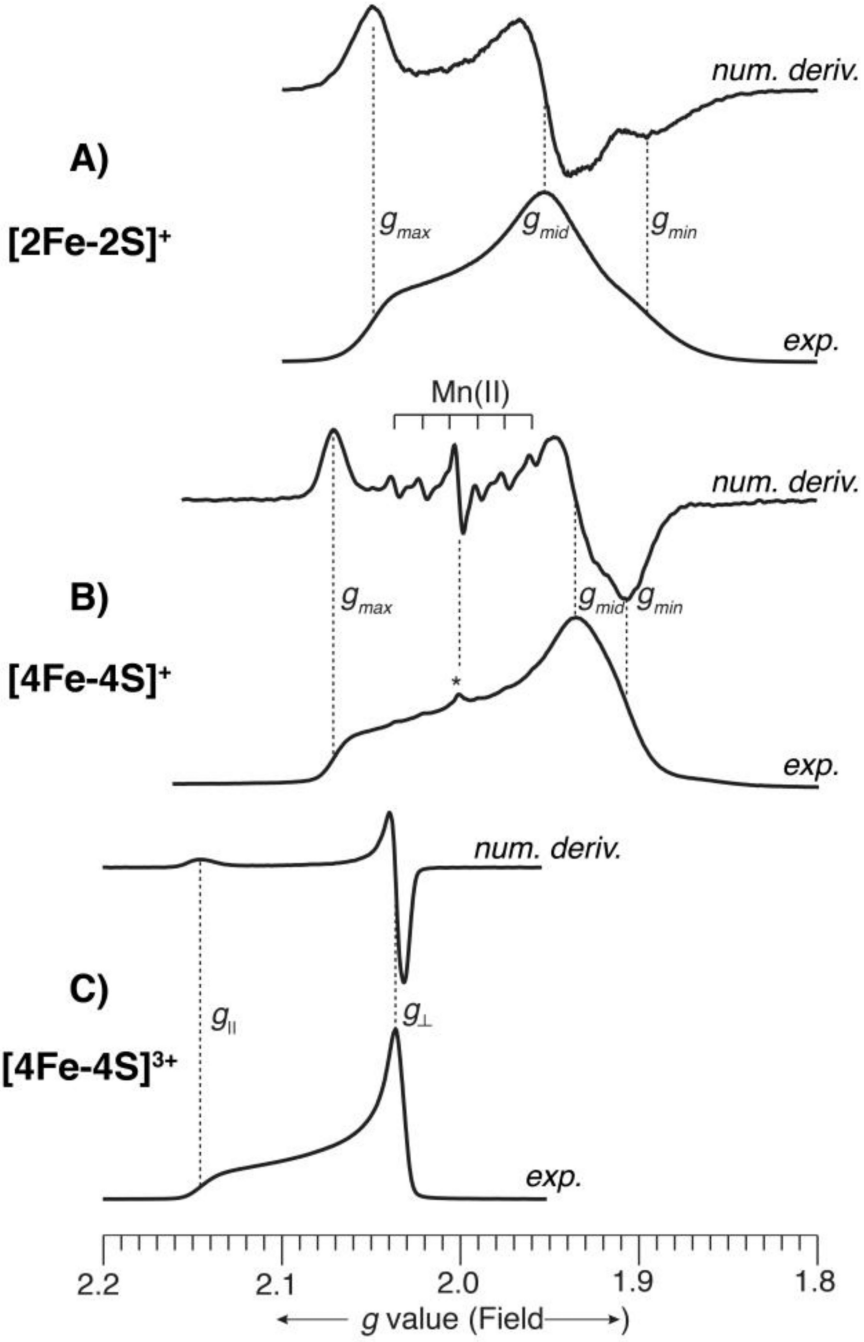

Figure 4.

Q-band (35 GHz) EPR spectra of three, representative FeS proteins. The spectra were all recorded at 2 K under “rapid passage” conditions, so that the experimental spectrum appears as an absorption lineshape. A digital derivative spectrum is displayed above each experimental spectrum, which gives the familiar presentation of EPR spectra. The intensities of all spectra have been arbitrarily scaled for ease of viewing. The abscissa is given in descending *g* value scale (corresponding to increasing magnetic field) to allow comparison among spectra recorded at slightly different microwave frequencies. The *g* values of the FeS

clusters are indicated on each spectrum. A) *Aquifex aeolicus* reduced 2Fe-Fd, $[2Fe2S]^{+}$, recorded at 35.028 GHz; B) *Desulfovibrio gigas* reduced 4Fe-Fd, $[4Fe4S]^{+}$, recorded at 34.946 GHz; In (B), the presence of a small amount of adventitious Mn(II), a common occurrence in metalloprotein samples, is indicated. This narrow line sextet (^{55}Mn, $I = 5/2$, 100%) is accentuated in the derivative presentation. An unknown radical ($g \approx 2.00$) is also present in very small amount and is indicated by an asterisk. C) *Halorhodospira halophila* (formerly *Ectothiorhodospira halophila*) oxidized HiPIP, $[4Fe4S]^{3+}$, recorded at 34.958 GHz.

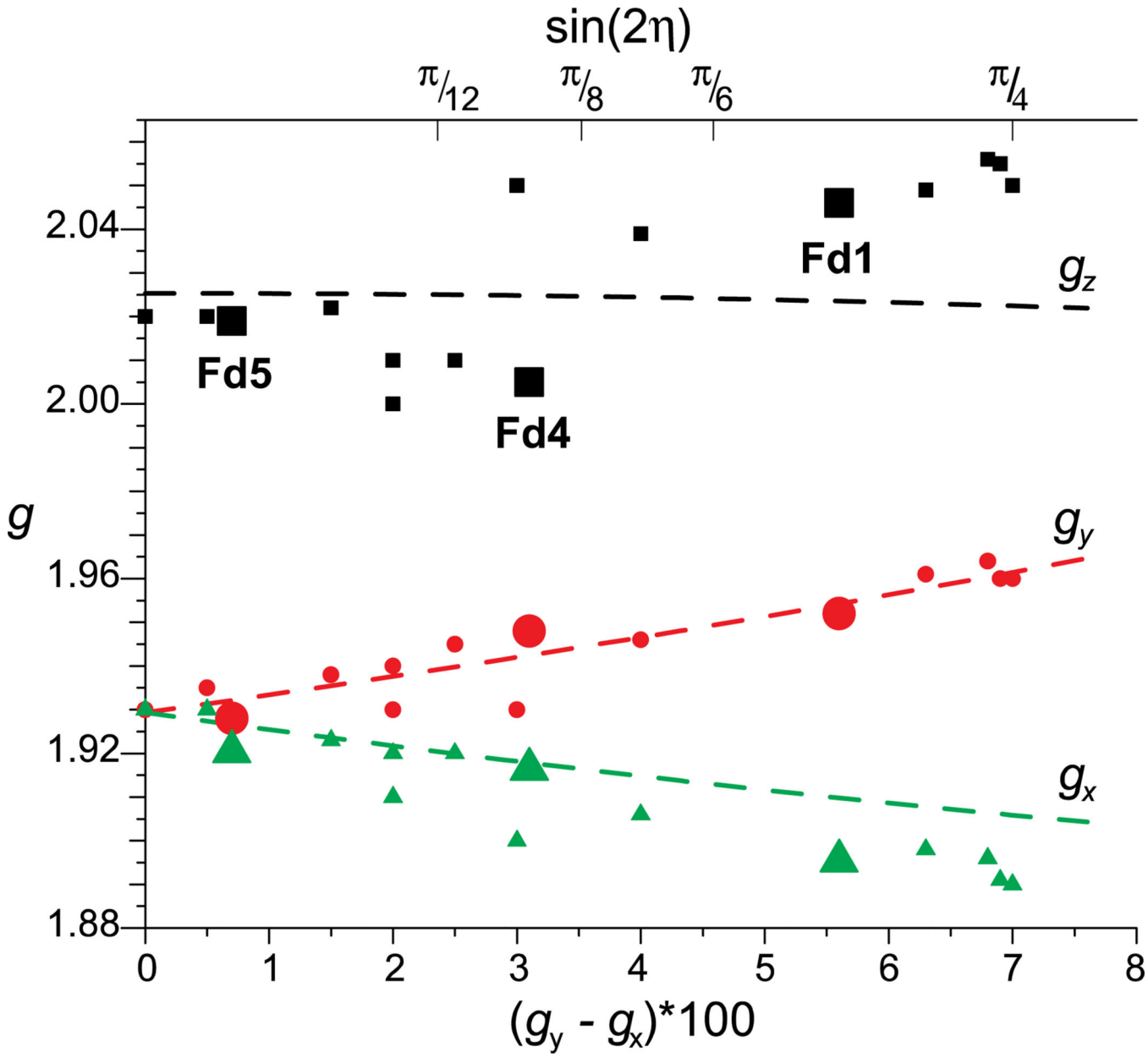

Figure 5.

'Bertrand plot' of *g* tensor components against Δg_{∞} (×100) for various [2Fe–2S] proteins of the g_{iso} = 1.96 subclass. Dashed lines represent values from Eqs. 6 – 8 calculated with the parameters $\lambda = -60\ cm^{-1}$, $\Delta E_{xy} = 15{,}000\ cm^{-1}$, $\Delta E_{xz} = \Delta E_{yz} = 5{,}000\ cm^{-1}$, $\mathbf{g}(^{57}Fe^{III}) = 2.01$. Reprinted from **Figure 5** of Cutsail, et al. [20] with kind permission from Springer Science and Business Media © 2012 SBIC.

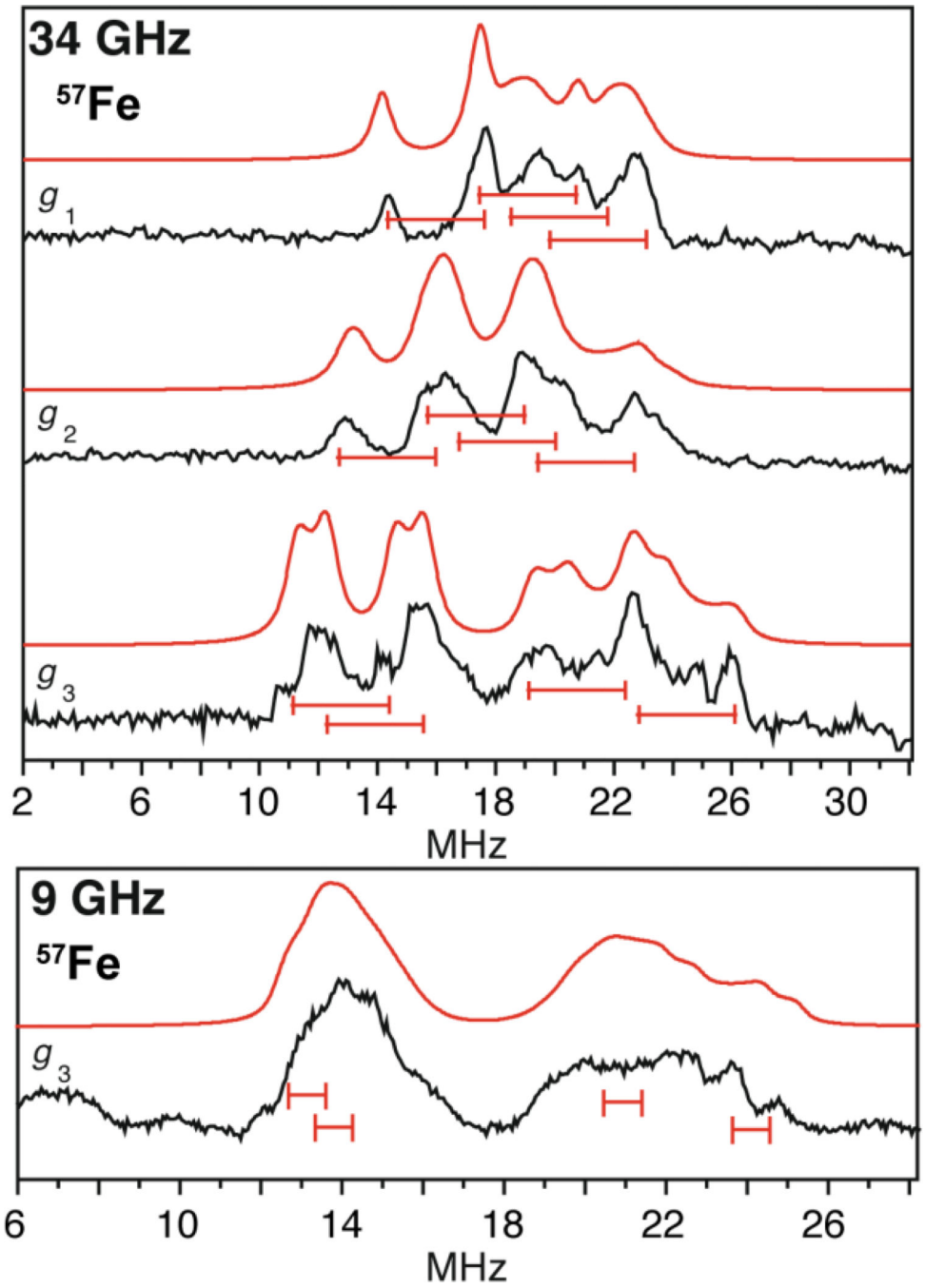

Figure 6.

The ^{57}Fe ENDOR of the [4Fe4S] cluster of the HdrB subunit taken at Q- and X-band frequencies with *A*/2 centered goalposts in red of length equal to $2\nu_n$. The higher frequency, Q-band (34 GHz) ENDOR generated better separation of the ^{57}Fe hyperfine as $2\nu_n$ is much greater from the higher magnetic field than that employed at X-band (9 GHz) frequency. ^{57}Fe ENDOR reprinted from Figure 2 of Fielding, et al. [106] with kind permission from Springer Science and Business Media © 2013 SBIC.

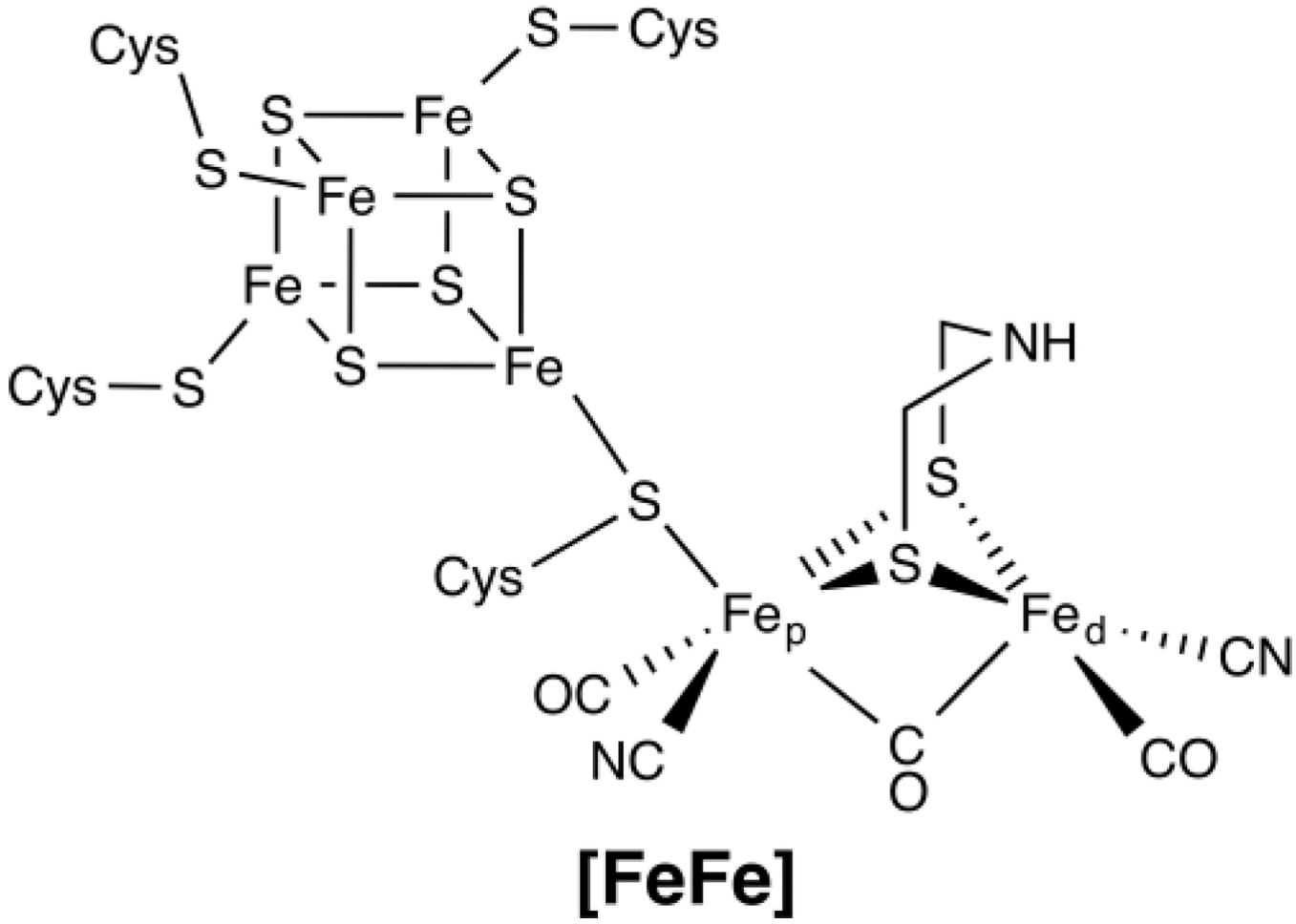

Figure 7.
Hydrogenase Active Site Structure; iron-only [FeFe] hydrogenase.

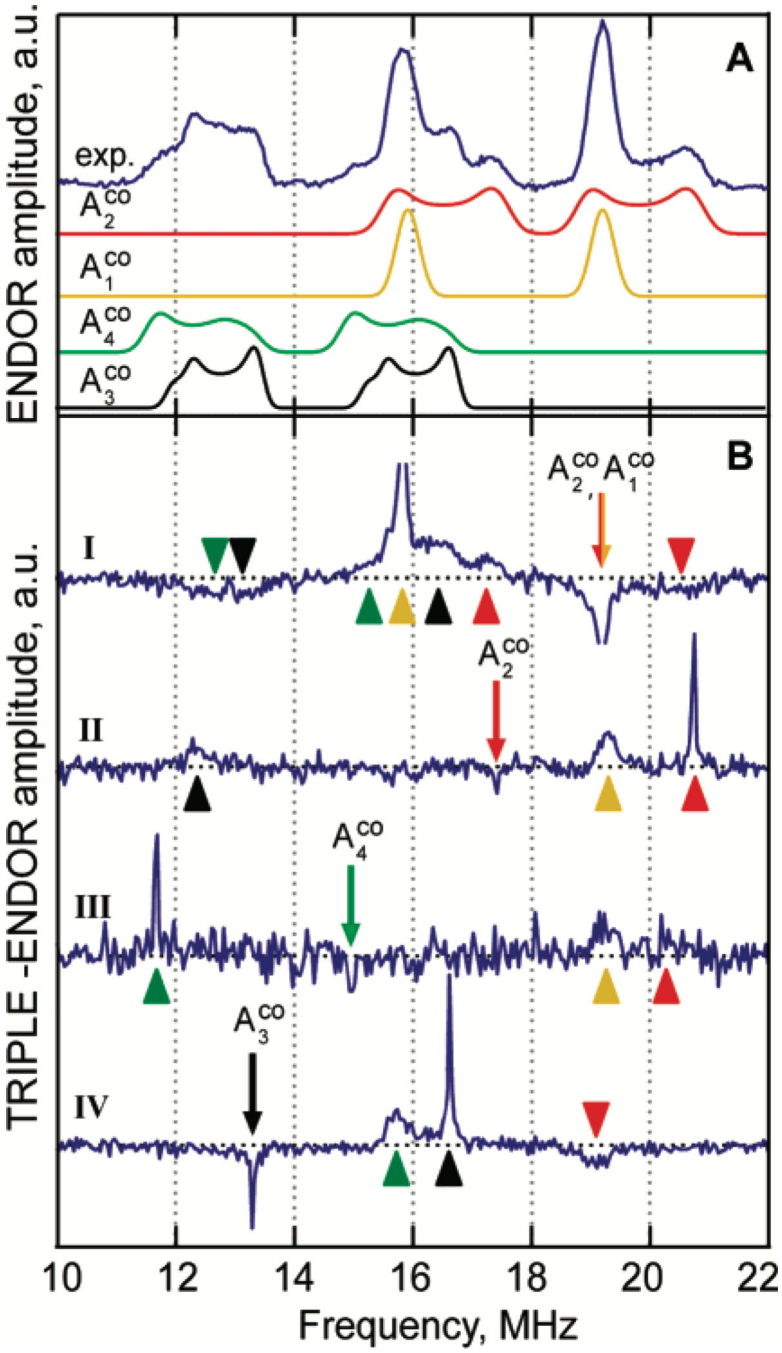

Figure 8.

Q-band TRIPLE spectra of the ^{57}Fe-enriched H-cluster of the [FeFe] hydrogenase in the H_{ox}-CO state (where an exogenous CO ligand is bound). (**A**) Reference ^{57}Fe ENDOR spectrum with simulated components A_1^{CO}, A_2^{CO}, A_3^{CO}, A_4^{CO} of the cuboidal [4Fe4S] cluster. (**B**) Difference (TRIPLE ENDOR) Q-band spectra for various pump frequencies (second RF pulse) at frequencies indicated by arrows, with color of the arrows corresponds to the HFI components of the ENDOR spectrum (panel **A**), which were predominantly excited. The triangles in **B** assign the peaks in the difference TRIPLE spectra to the

hyperfine couplings of the ENDOR spectrum using the same color code as in **A**. Reprinted with permission from Silakov, et al. [41] Copyright 2007 American Chemical Society.

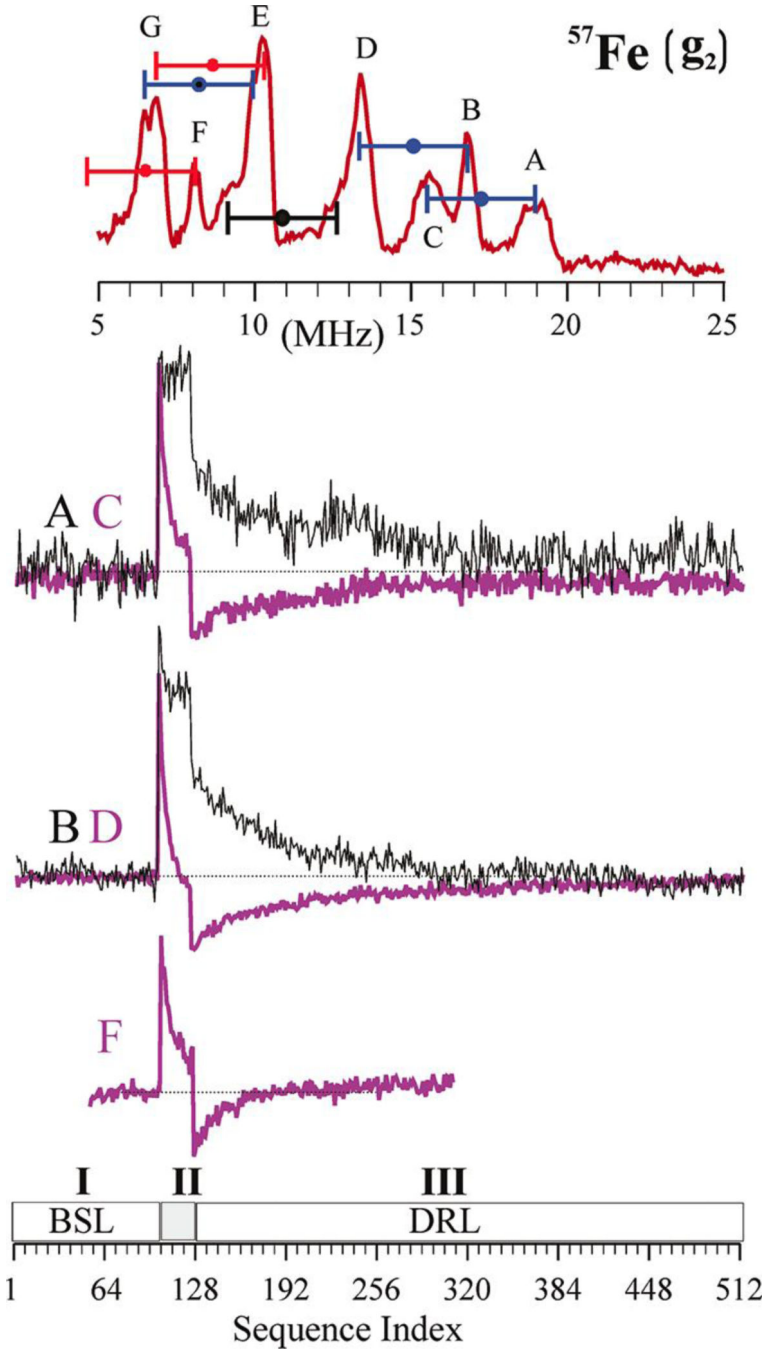

Figure 9.

Determination of signs of hyperfine couplings at g_2 by PESTRE technique at Q-band. Top: Davies ENDOR spectrum indicating the ENDOR peaks being interrogated. The goalposts here are color coded to indicate sign of hyperfine coupling: blue, negative; red, positive; black, undetermined. Center: PESTRE traces, presented as the difference between the observed ESE signal and the BSL (**Δ**ESE) recorded at: upper set: peaks A (black trace) and C (purple trace); middle set: B (black trace) and D (purple trace); lower: F (purple trace). Bottom: schematic of the PESTRE protocol showing Stage I (RF off, **BSL**); Stage II (RF on,

ENDOR signal); Stage III (RF off, **DRL**). Reprinted with permission from Doan, et al. [46] Copyright 2011 American Chemical Society.

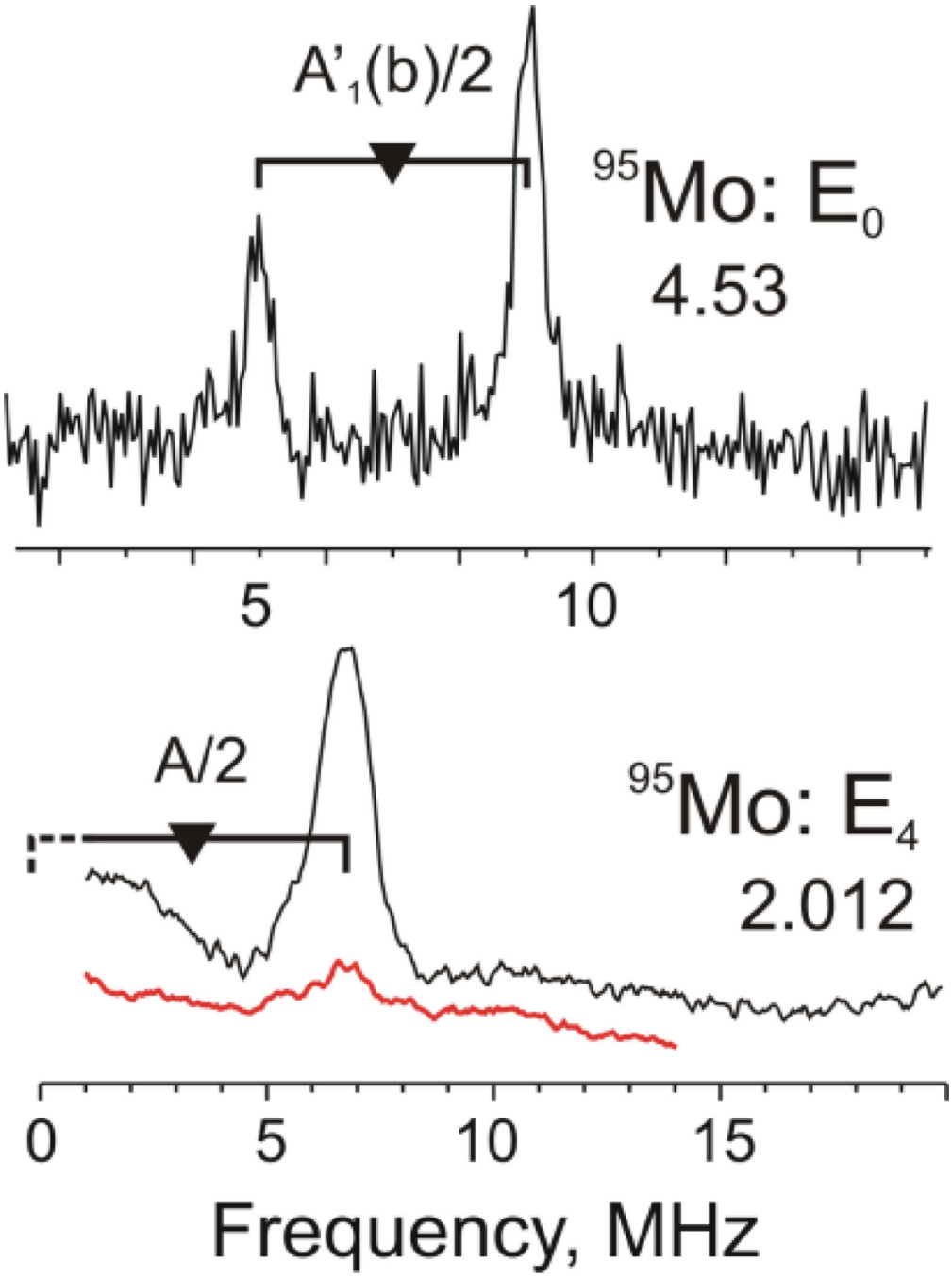

Figure 10.
(top) Davies ^{95}Mo-ENDOR spectra of ^{95}Mo-enriched (black) and natural-abundance (red) α-70^{Ile} MoFe protein: (top) in the resting state. (E_0); (bottom) CW ^{95}Mo ENDOR of trapped intermediate (E_4) state. Reprinted with permission from Lukoyanov, et al. [135] Copyright 2010 American Chemical Society.

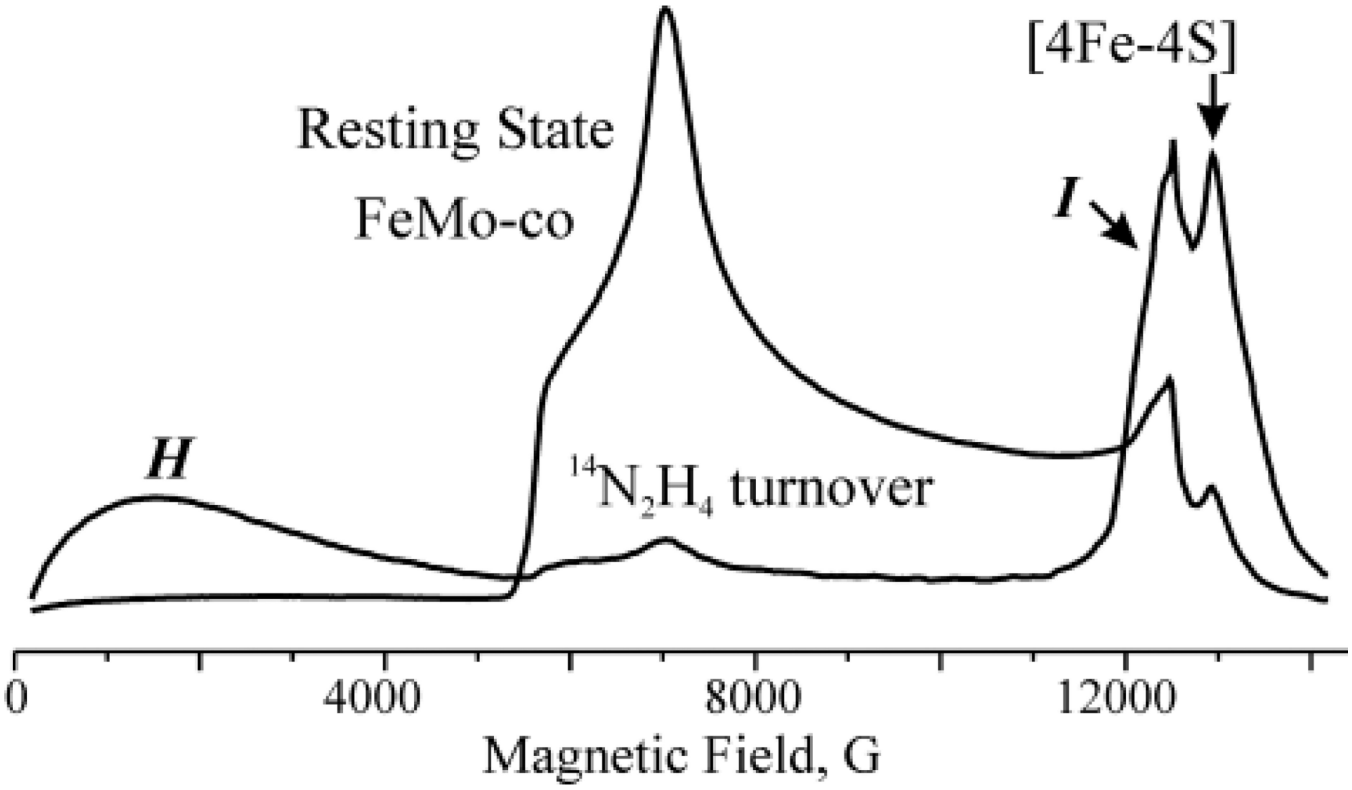

Figure 11.

35 GHz CW EPR spectra (absorption-display) of resting-state FeMo-co and from freeze-trapped turnover intermediates ***H*** and ***I***. Note that resting state FeMo-co has $S = 3/2$ ground state and effective g values of [4.3, 3.64, 2.0] and the ***H*** intermediate has $S = 2$ ground state and very high effective g values (low field transitions).

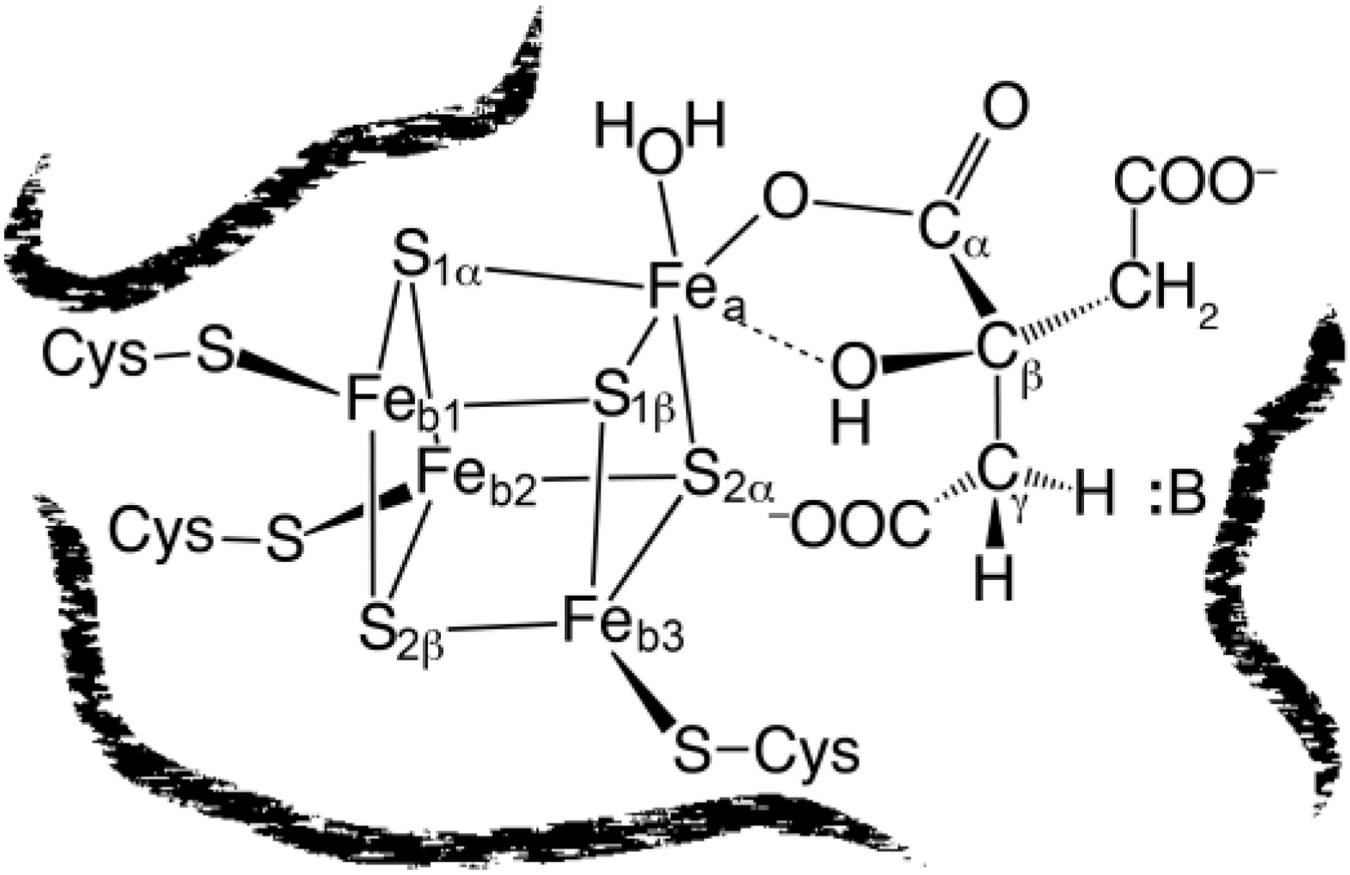

Figure 12.

Aconitase Structure showing disposition of Fe and S ions as deduced from ^{57}Fe ENDOR/ Mossbauer studies and ^{33}S ENDOR studies; structure of citrate bound to the unique Fe_a site of the [4Fe4S] cluster as deduced from ENDOR spectroscopy of substrates, as described below.

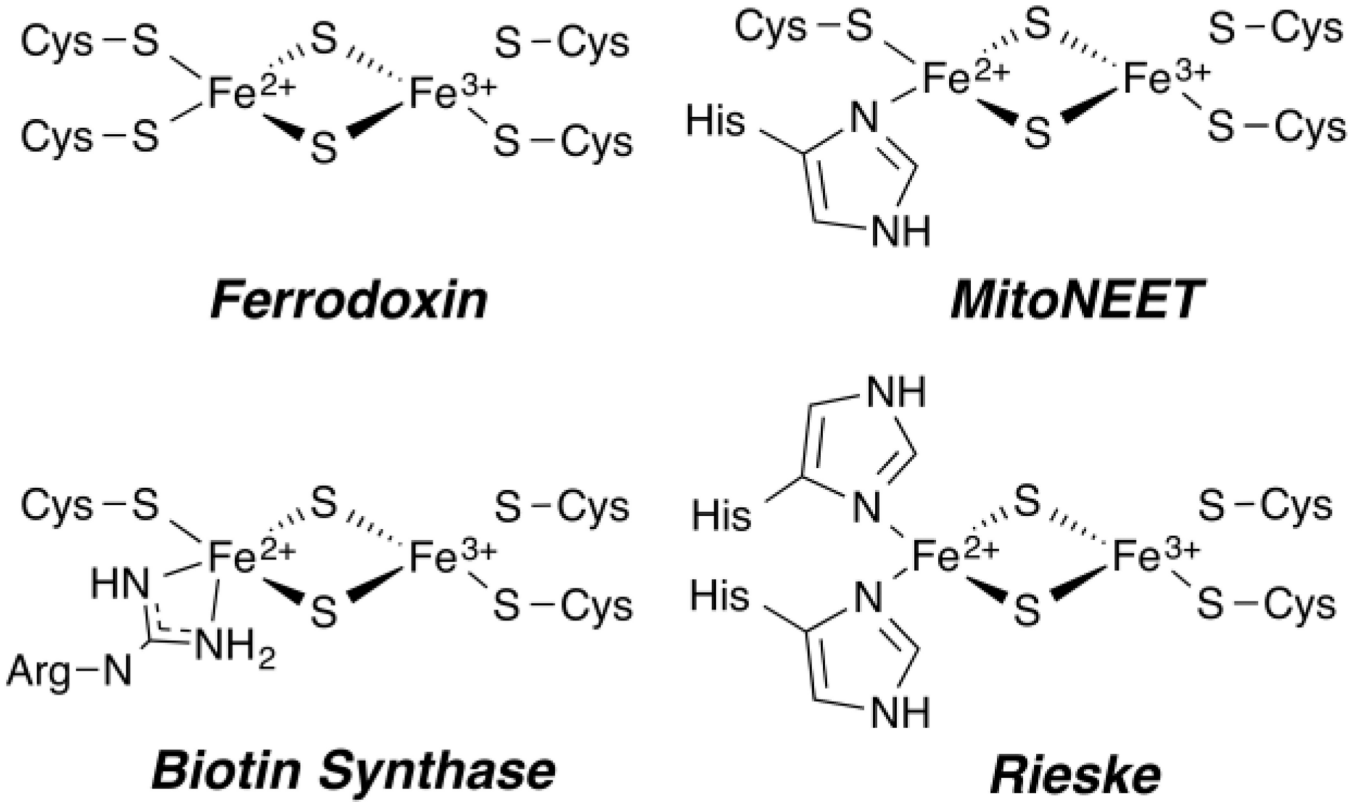

Figure 13.
$[2Fe2S]^{+}$ Coordination in a variety of biological systems as indicated.

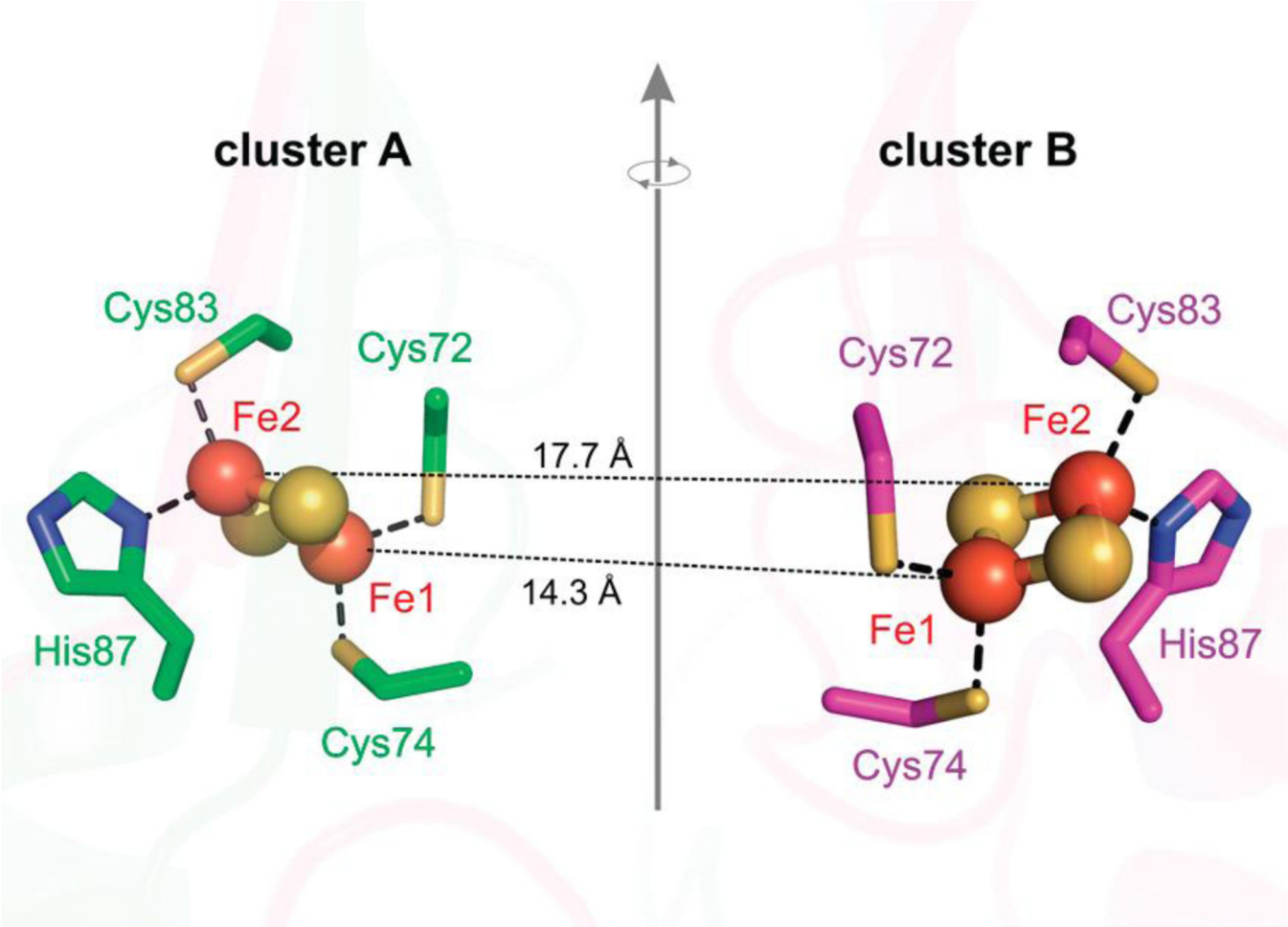

Figure 14.

Two [2Fe2S] clusters, (iron, *orange*, sulfur, *yellow*) of the homodimer human mitoNEET separated by ~16 Å, related by a rotation around a 2-fold symmetry axis between the two monomers (*green* and *pink*). PDB ID 2QH7. Reprinted with permission from Dicus, et al. [78] Copyright 2010 American Chemical Society.

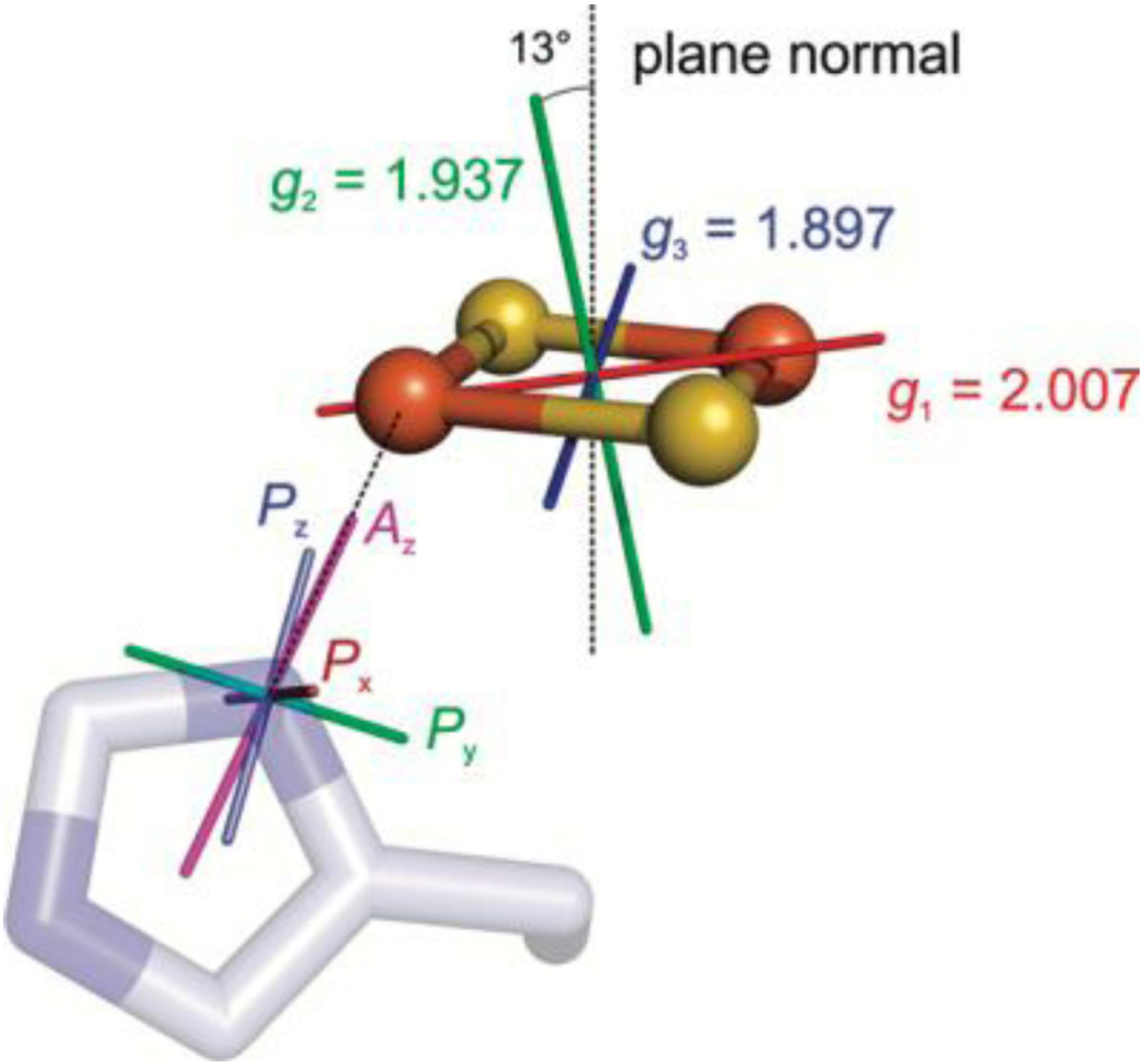

Figure 15.

The assignment shown of A_z aligned with the N-Fe bond and P_x with the imidazole plane normal yields the **g** tensor orientation for mitoNEET protein (**g** = [g_1, g_2, g_3] = [2.007, 1.937, 1.897]). The angle between the g_2 axis and the cluster plane normal is 13°, the g_1 axis is 34° offset from the Fe-Fe vector, and g_3 is 33° offset from the S-S vector. Reprinted with permission from Dicus, et al. [78] Copyright 2010 American Chemical Society.

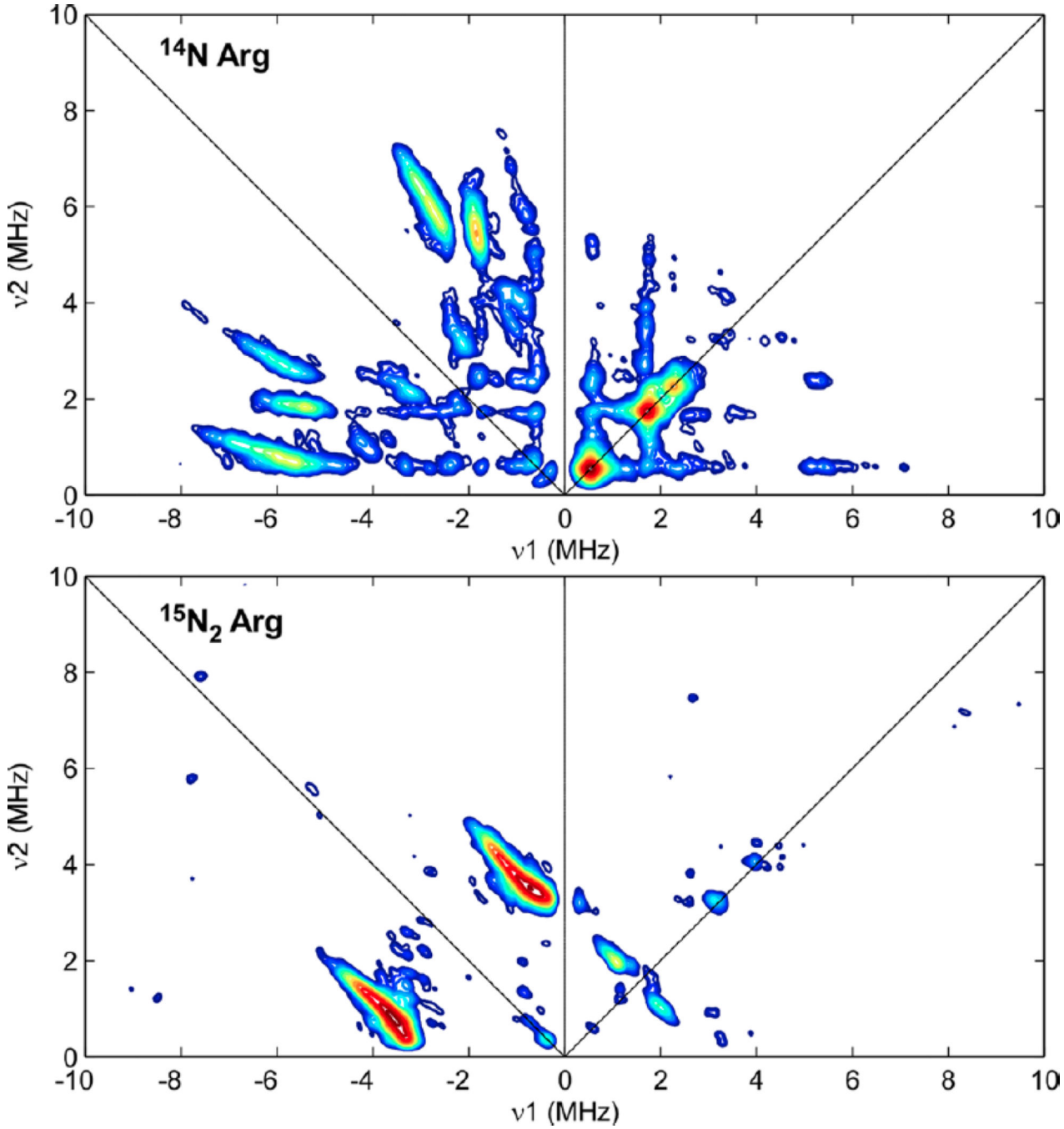

Figure 16.

X-band HYSCORE spectra of biotin synthase paramagnetic intermediate grown in *E. coli* with natural abundance arginine (top) and (*guanidino*-$^{15}N_2$)-L-arginine (bottom). The ^{15}N coupling observed in the bottom HYSCORE spectrum corresponds to ^{15}N labeling of the Arg260 residue. Reprinted with permission from Fugate, et al. [153] Copyright 2012 American Chemical Society.

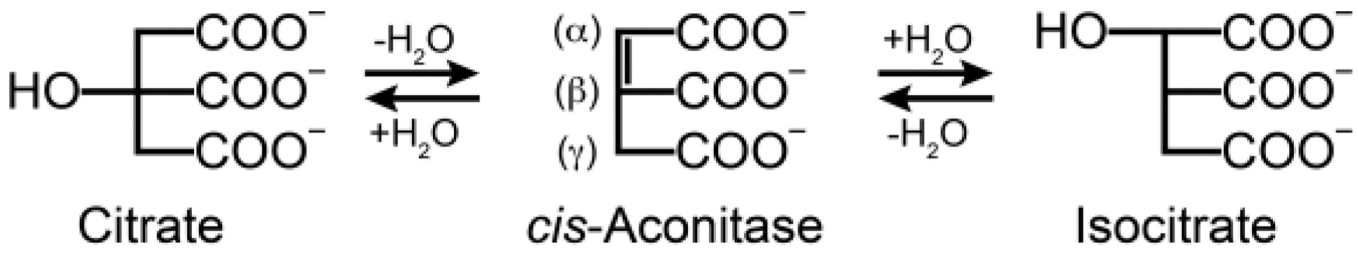

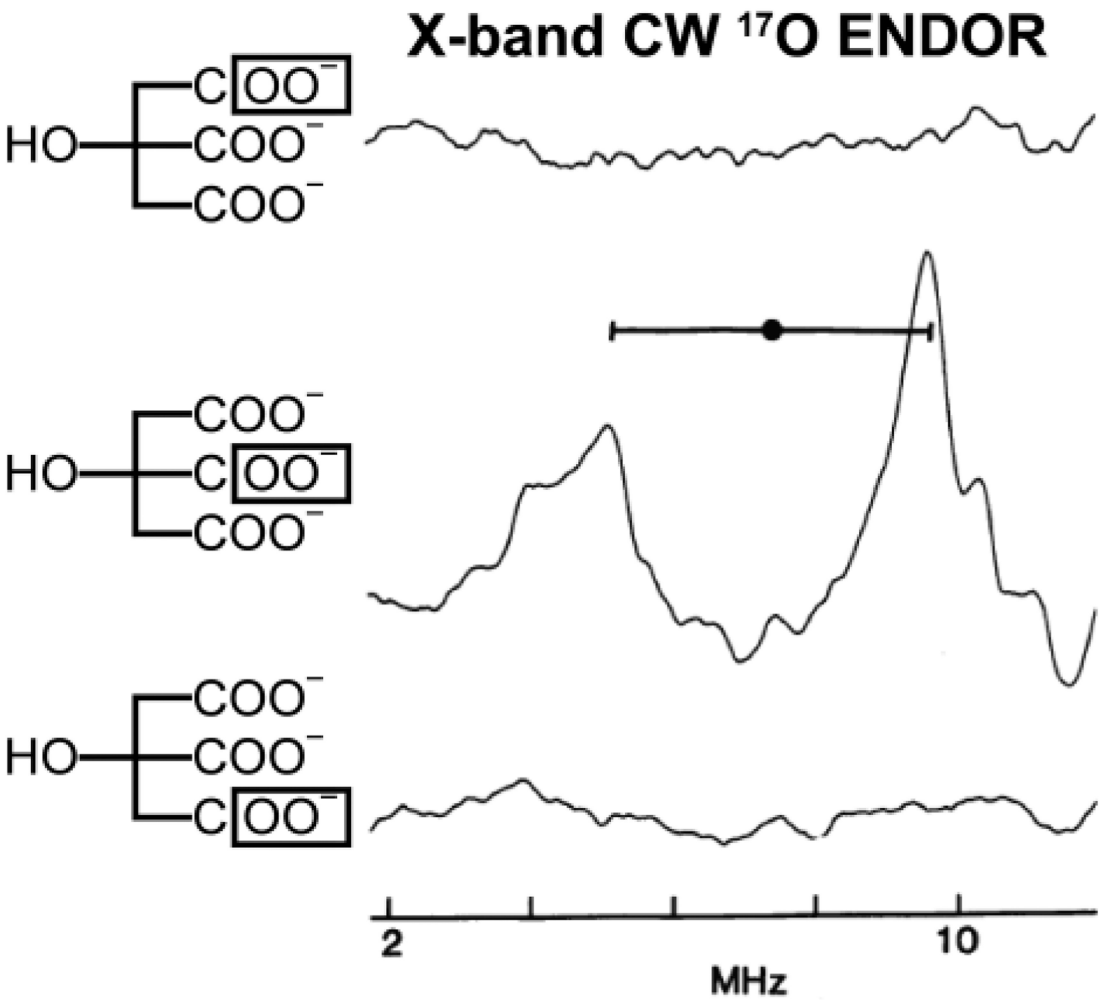

Figure 17.

X-band ^{17}O CW ENDOR of isotopically labeled substrate at the α, β, and γ carboxyl positions as indicated in the figure. A ^{17}O ENDOR response is only observed with labeling of the β carboxyl group. ENDOR spectra reprinted from Kennedy, et al. [162].

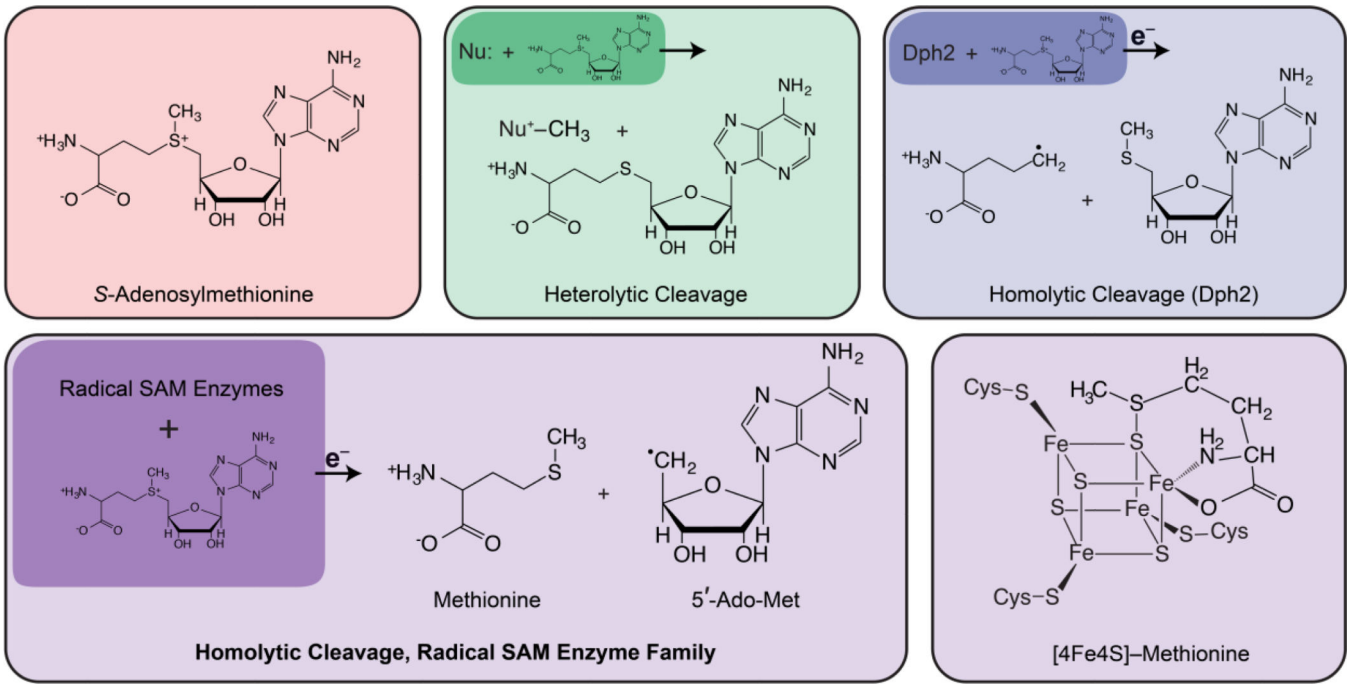

Figure 18.

The various reaction products of the *S*-Adenosylmethionine (SAM) (red) co-substrate. Different reactions, either heterolytic or homolytic cleavage, at the positively charged sulfur atom provide the final products. Heterolytic cleavage by a nucleophilic base (Nu:) results in cleavage of the methyl group by breaking the methyl-sulfur bond, leaving both electrons on the sulfur. Homolytic cleavage of SAM has most commonly been observed in the radical SAM enzyme family, where SAM accepts an electron yielding a methionine and 5'-deoxyadenosyl radical (5'-Ado-Met). Homolytic cleavage (such as in Dph2) may occur uniquely at the opposite 3-amino-3-carboxypropyl group after accepting an electron and results in a different organic radical.

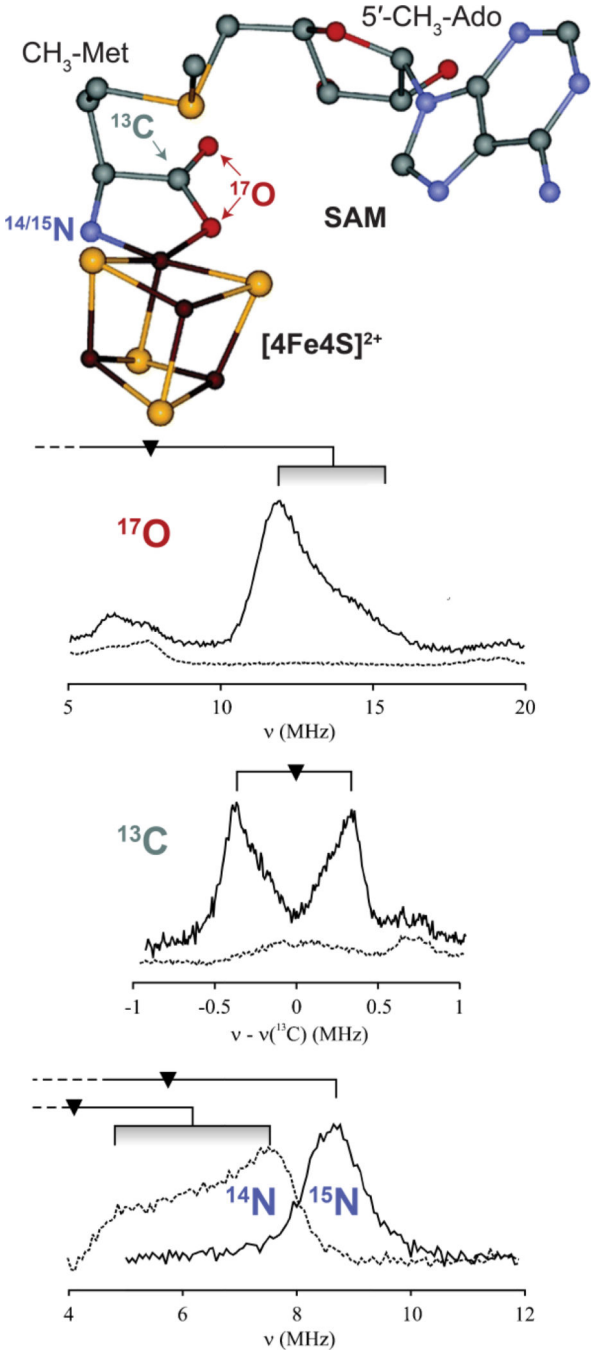

Figure 19.

Arrangement of $[4Fe4S]^{2+}$ and SAM (top) with isotopic labels for corresponding ENDOR spectra below. Q-band Pulsed ENDOR of PF-AE with $H_2{}^{17}O$, ^{13}C carboxylato-labeled and ^{15}N-amino-labeled AdoMet compared with data from an unlabeled sample with triangle representing each nuclei's Larmor frequency. Adapted with permission from Walsby, et al. [169] and Lees, et al. [170] Copyright 2005, 2006 American Chemical Society.

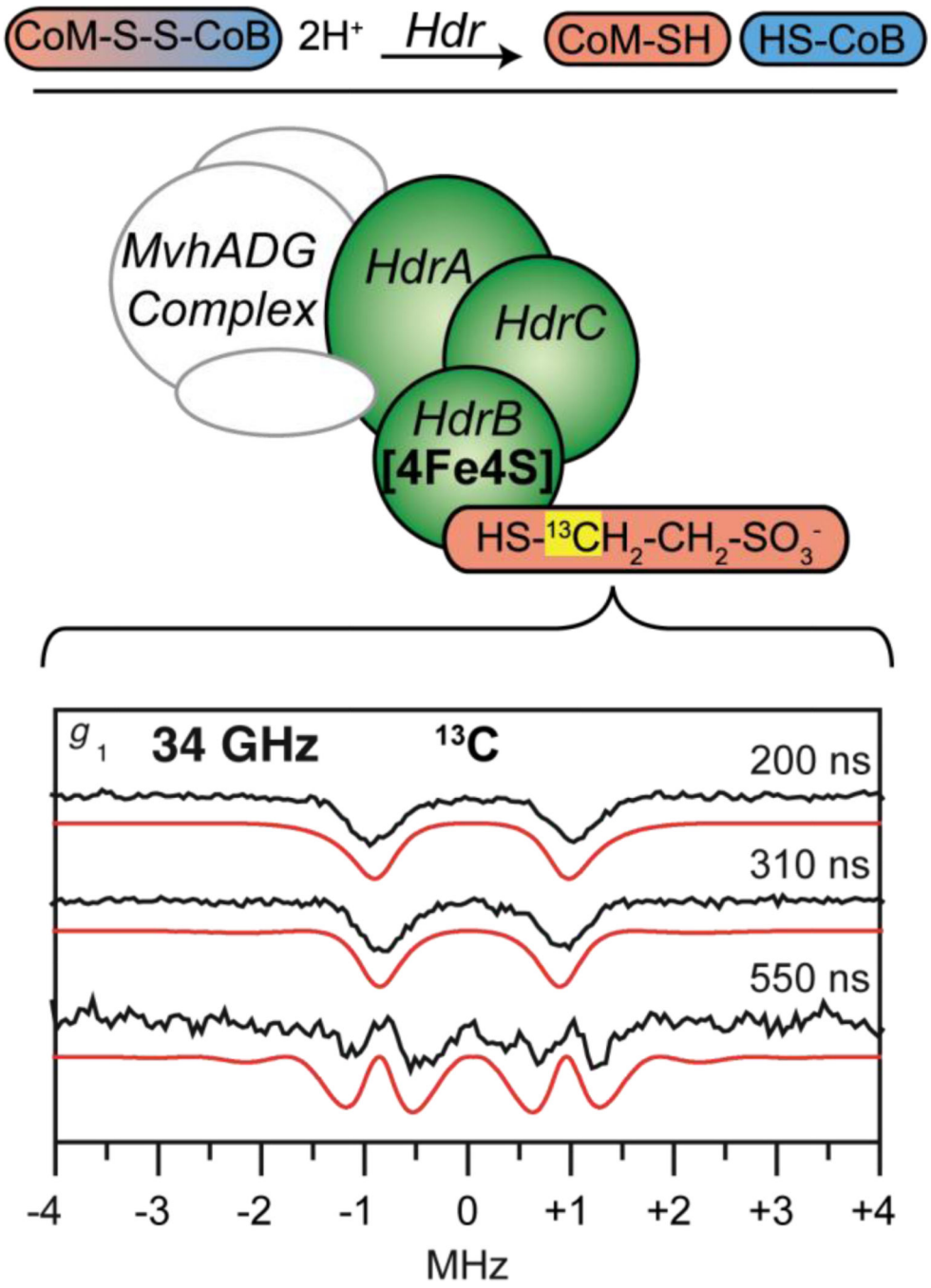

Figure 20.

(*top*) A cartoon reaction of the reduction of CoM-S-S-CoB by Hdr and the cartoon MvhADG-HdrABC protein complex with ^{13}C ENDOR of CoM-HdrABC with ^{13}C labeled CoM ($HS^{13}CH_2{}^{12}CH_2SO_3^-$). (*bottom*) ^{13}C ENDOR adapted and reprinted from Figure 4 of Fielding, et al. [106] with kind permission from Springer Science and Business Media © 2013 SBIC.

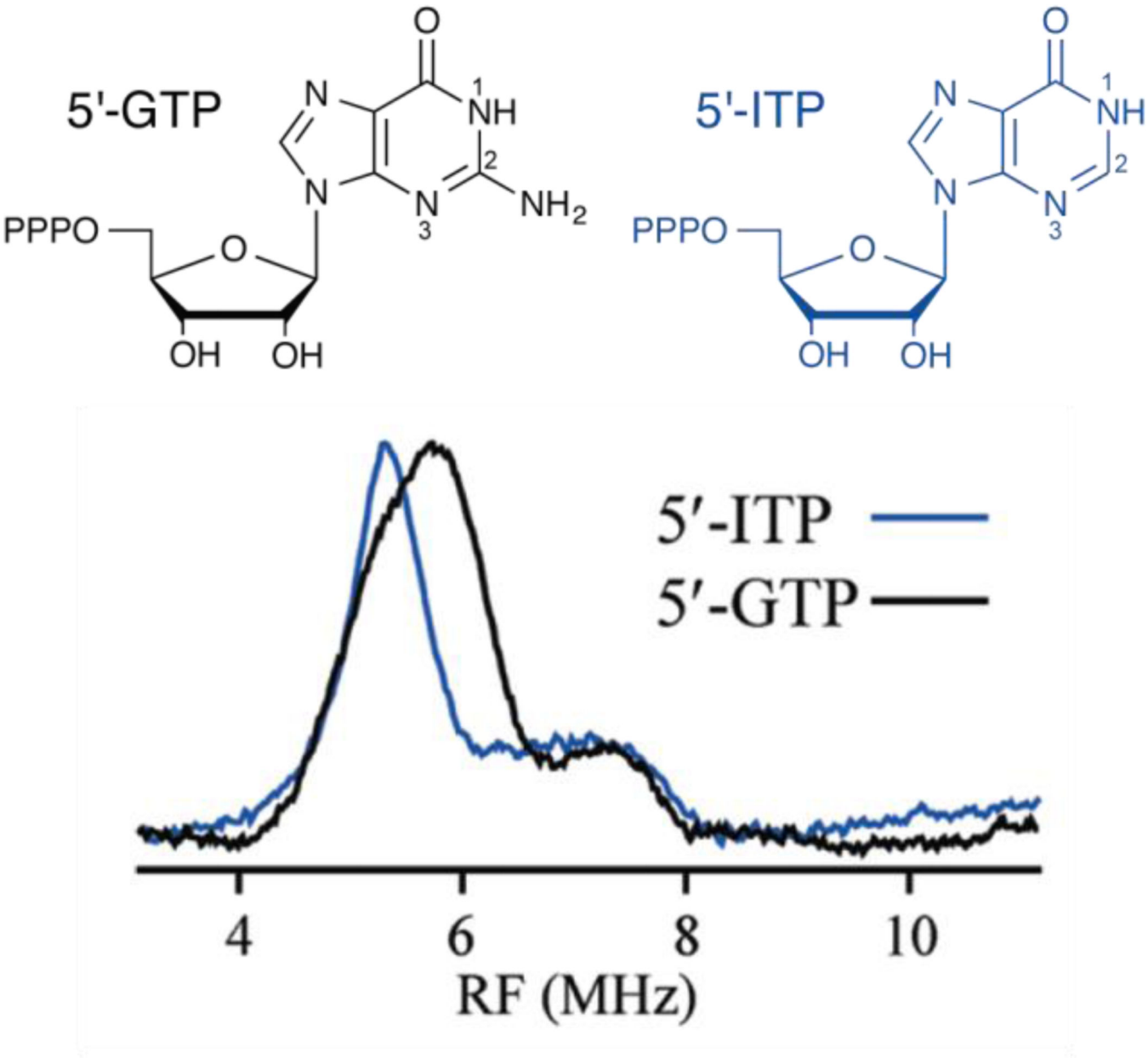

Figure 21.

Chemical schematics of 5′-GTP and 5′-ITP substrates in black and blue, respectively, with corresponding 35 GHz ^{14}N CW-ENDOR of the bound 5'-GTP and 5'-ITP substrates to MoaA $[4Fe4S]^{+}$ cluster in black and blue, respectively. The possible amino group coordination at C2 (N2) to the FeS cluster is eliminated as the ^{14}N ENDOR of 5′-ITP do not differ upon the amino group's removal. Reprinted with permission from Lees, N., et al.. [188] Copyright 2009 American Chemical Society.

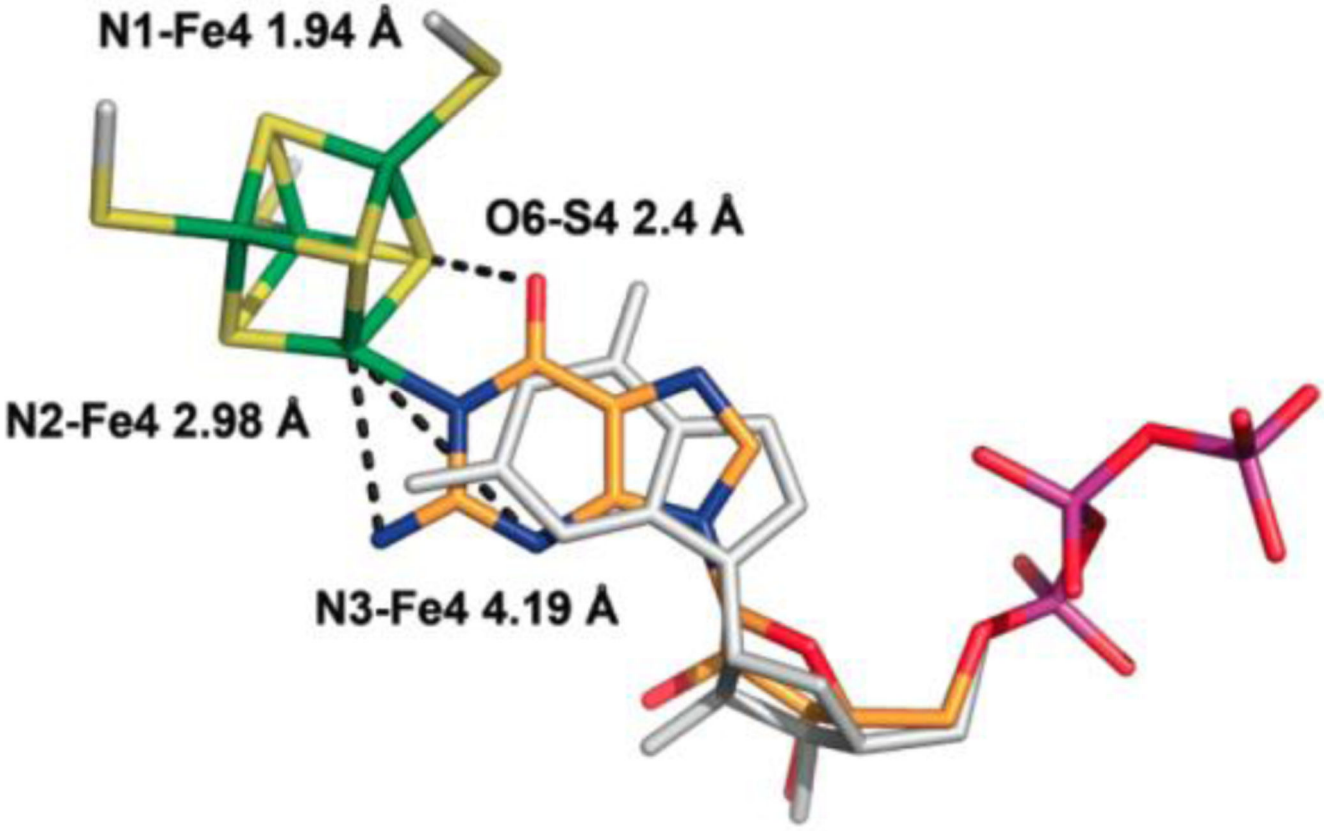

Figure 22.

Proposed model for 5′-GTP binding (C, orange; N, blue; O, red; P, purple) to the Fe4 ion of cluster II (S, yellow; Fe, green). The 5′-GTP model derived by X-ray crystallography (PDB entry 2FB3) is shown in white. Reprinted with permission from Lees, N., et al.. [188] Copyright 2009 American Chemical Society.

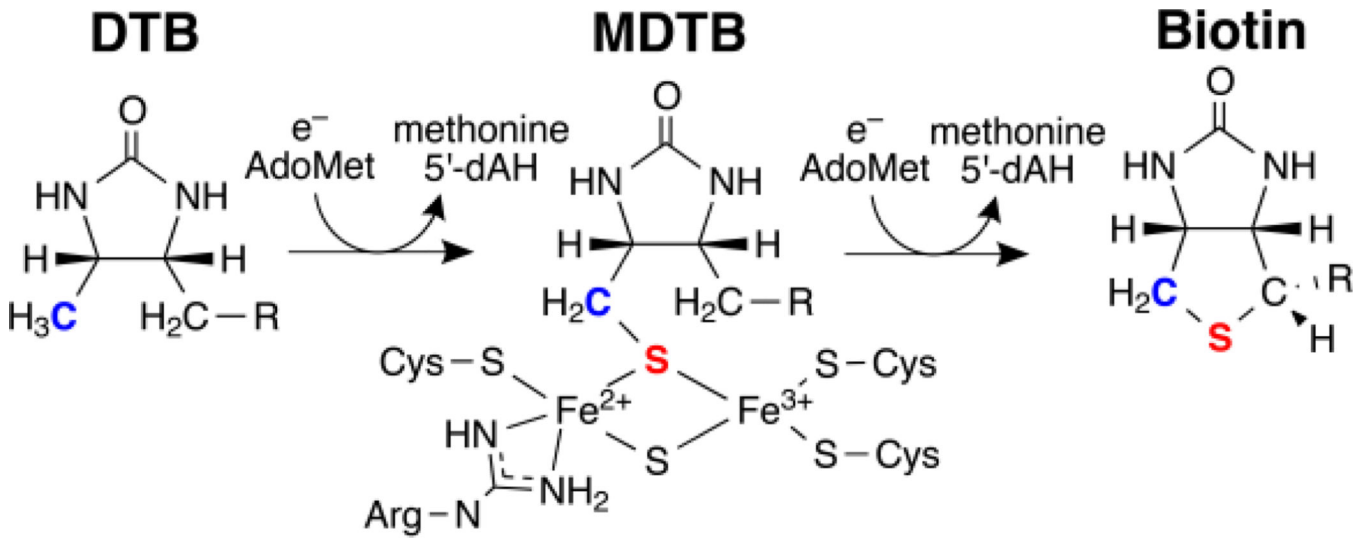

Figure 23.

Formation of biotin from dethiobiotin (DTB) via a two-step reaction with an stable 9-mercaptodethiobiotin MDTB intermediate bound to the sulfur donating $[2Fe2S]^{+}$ cluster.

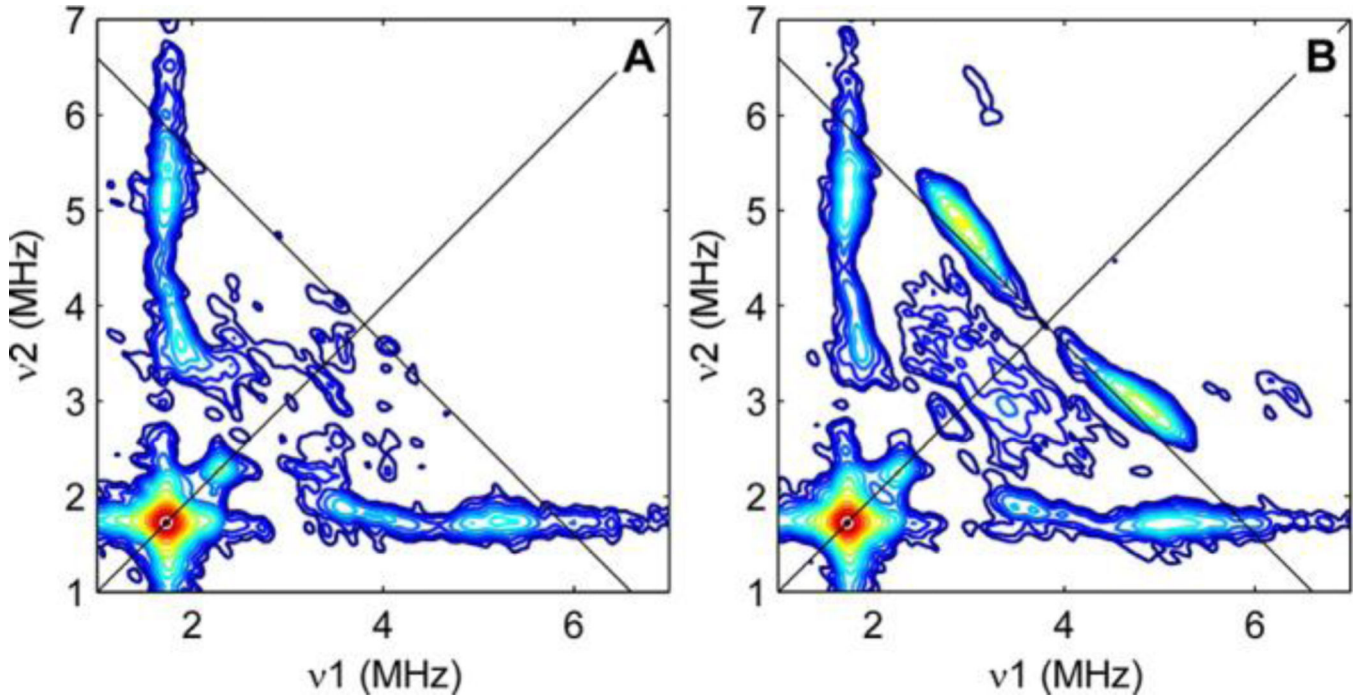

Figure 24.

X-band HYSCORE spectra of the biotin synthase paramagnetic intermediate prepared with (A) natural abundance DTB and (B) (9-methyl-^{13}C)-DTB. The two unique peaks perpendicular to the $\nu_1=\nu_2$ diagonal of B are the ^{13}C response. Reprinted with permission from Fugate, et al. [153] Copyright 2012 American Chemical Society.

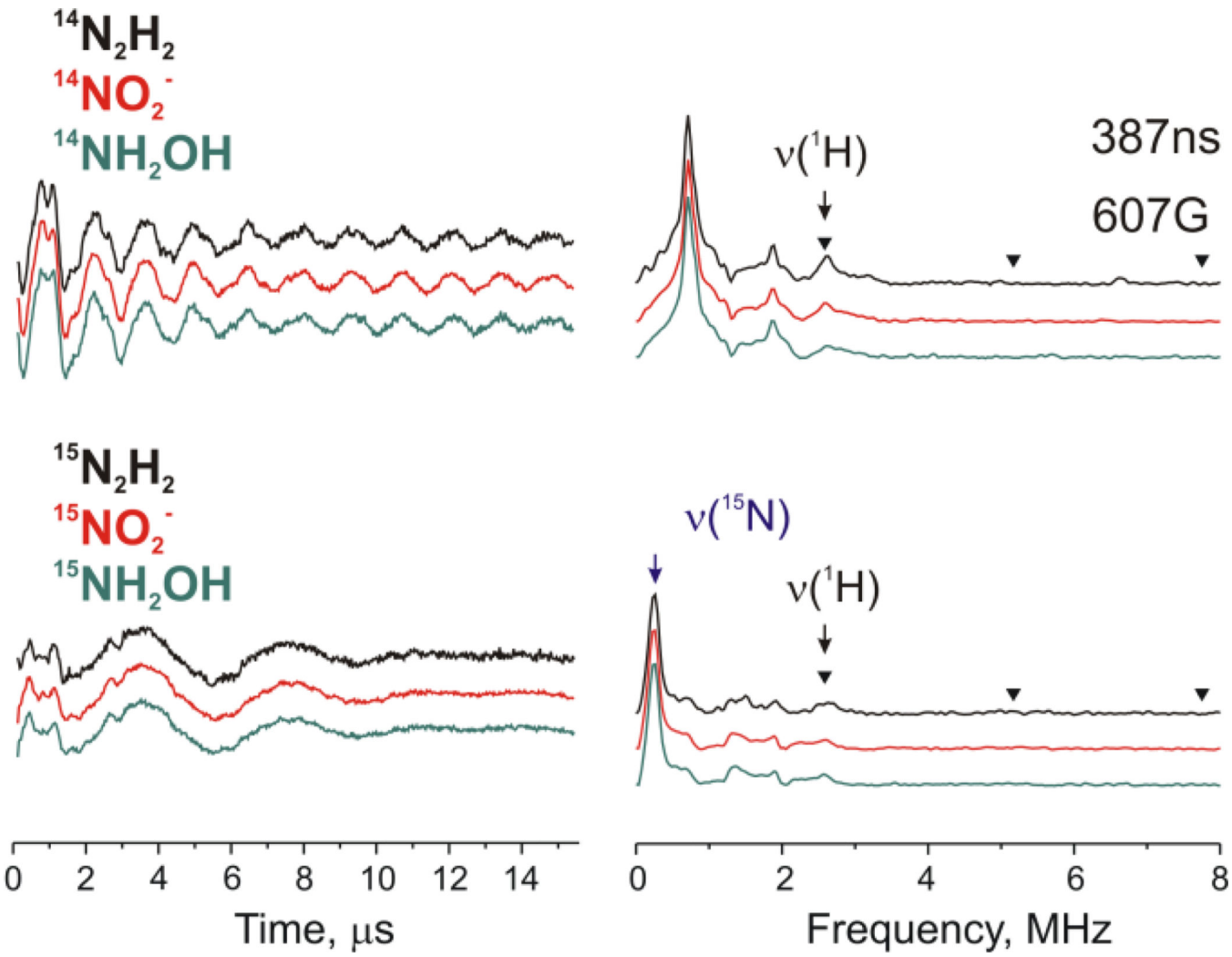

Figure 25.

Q-band NK-ESEEM spectra in time (left) and frequency (right) domains obtained for integer spin intermediates of α-70^{Ala}/ α-195^{Gln} MoFe protein turnover samples prepared with diazene (black), nitrite (red) and hydroxylamine (green). Upper spectra were measured for ^{14}N substrate samples, lower – for samples with ^{15}N labeled substrates. Triangles in the frequency domain spectra represent suppressed frequencies n/τ, n = 1, 2,

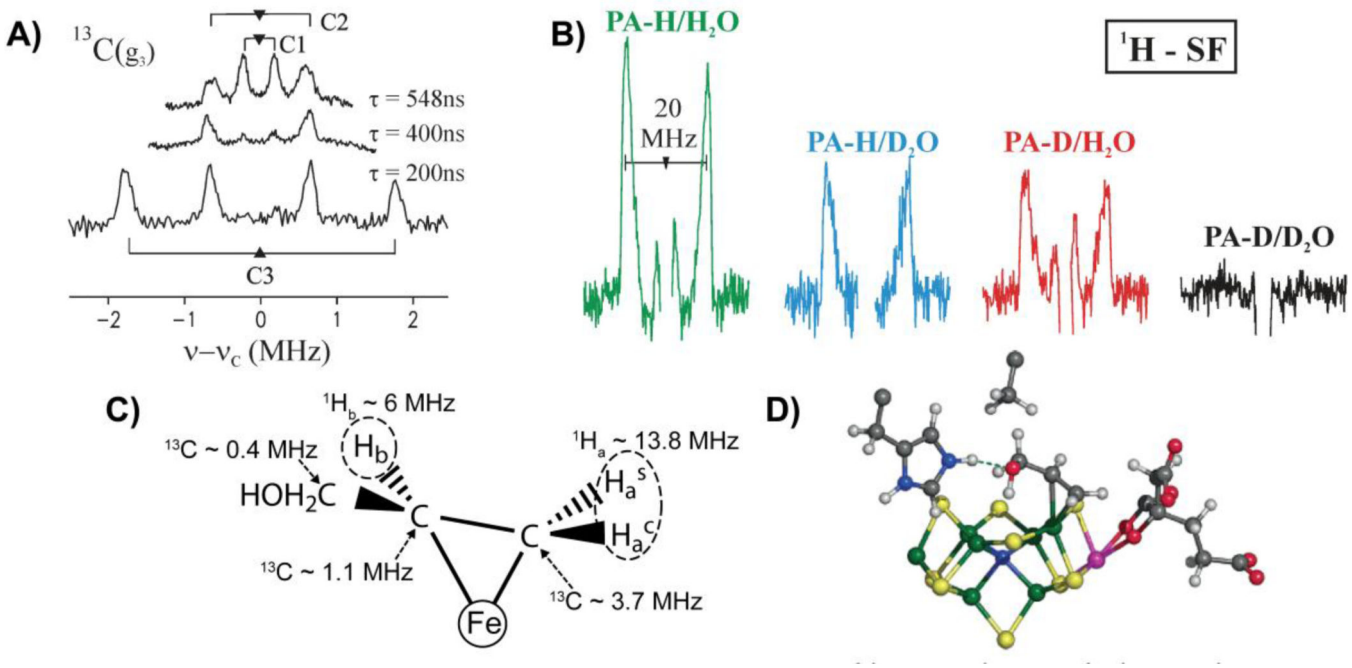

Figure 26.

A) Q-band ReMims and Mims pulsed ^{13}C ENDOR of the FeMo-cofactor of the α-70^{Ala} MoFe protein under turnover with PA(^{13}C). B) Quantitative stochastic field-modulated ENDOR spectra (^{1}H–SF) of the α-Ala^{70} MoFe protein same as A. The deuteration patterns are indicated; spectra are centered at the ^{1}H frequency and split by the hyperfine coupling. Key observation is that the intensity for the nondeuterated sample (green) is halved when either D_2O is used as solvent (blue) or the substrate is deuterated (red) and eliminated when deuterated substrate is used in D_2O (black). These results show that the bound intermediate contains two strongly coupled, magnetically identical protons, one that originates from substrate, the other from solvent. A third, weakly coupled proton is seen in the red and green spectra originating from the solvent. C) Proposed structure of the trapped propargyl alcohol reduction intermediate. D) Proposed structure for the trapped propargyl alcohol reduction intermediate bound to FeMo cofactor. The alkane unit of allyl alcohol is bound to Fe6 of the FeMo cofactor.

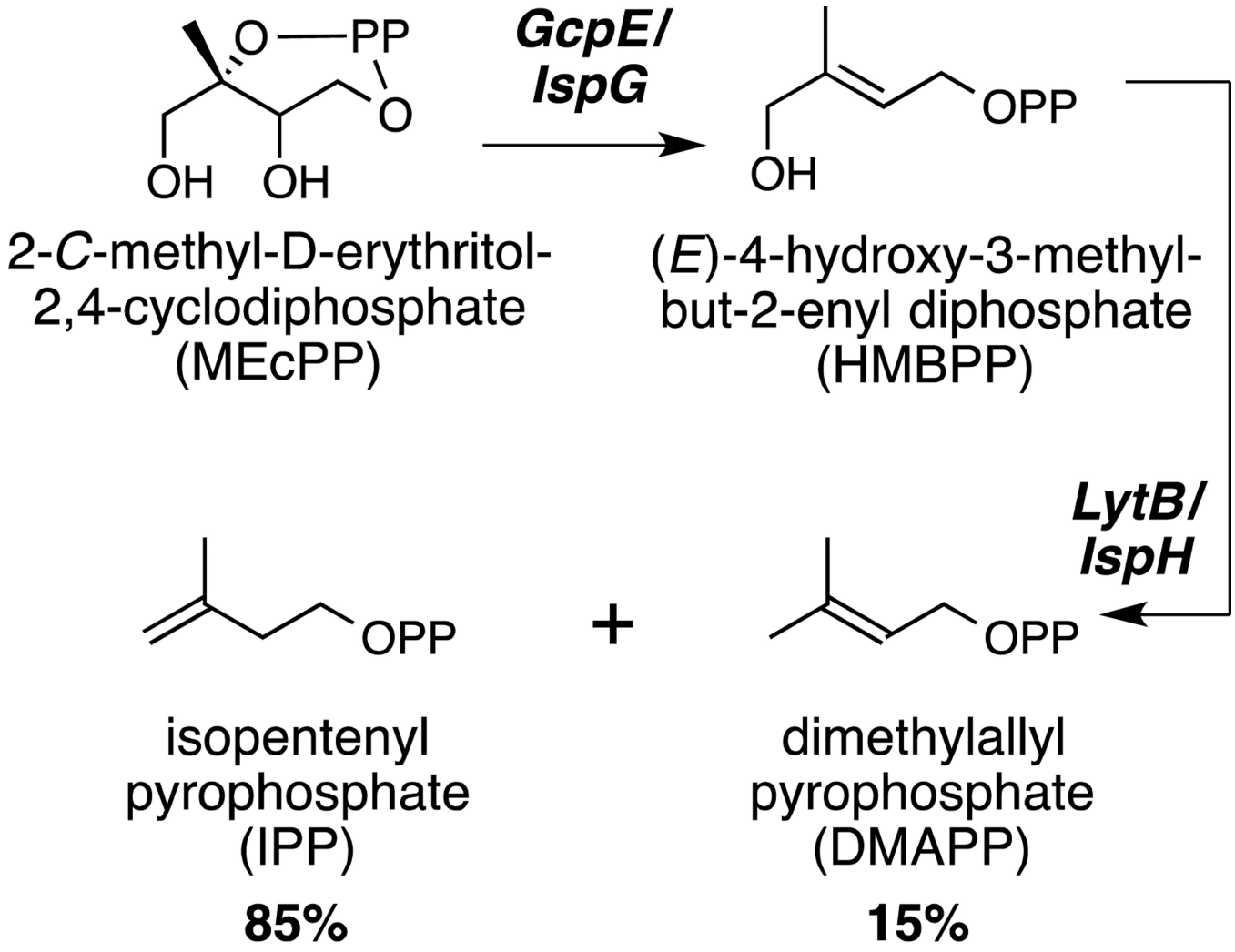

Figure 27.

The conversions of MEcPP to HMBPP by GcpE/IspG and HMBPP to DMAPP or IPP by LytB/IspH as part of the methyl-erythritol phosphate (MEP) pathway.

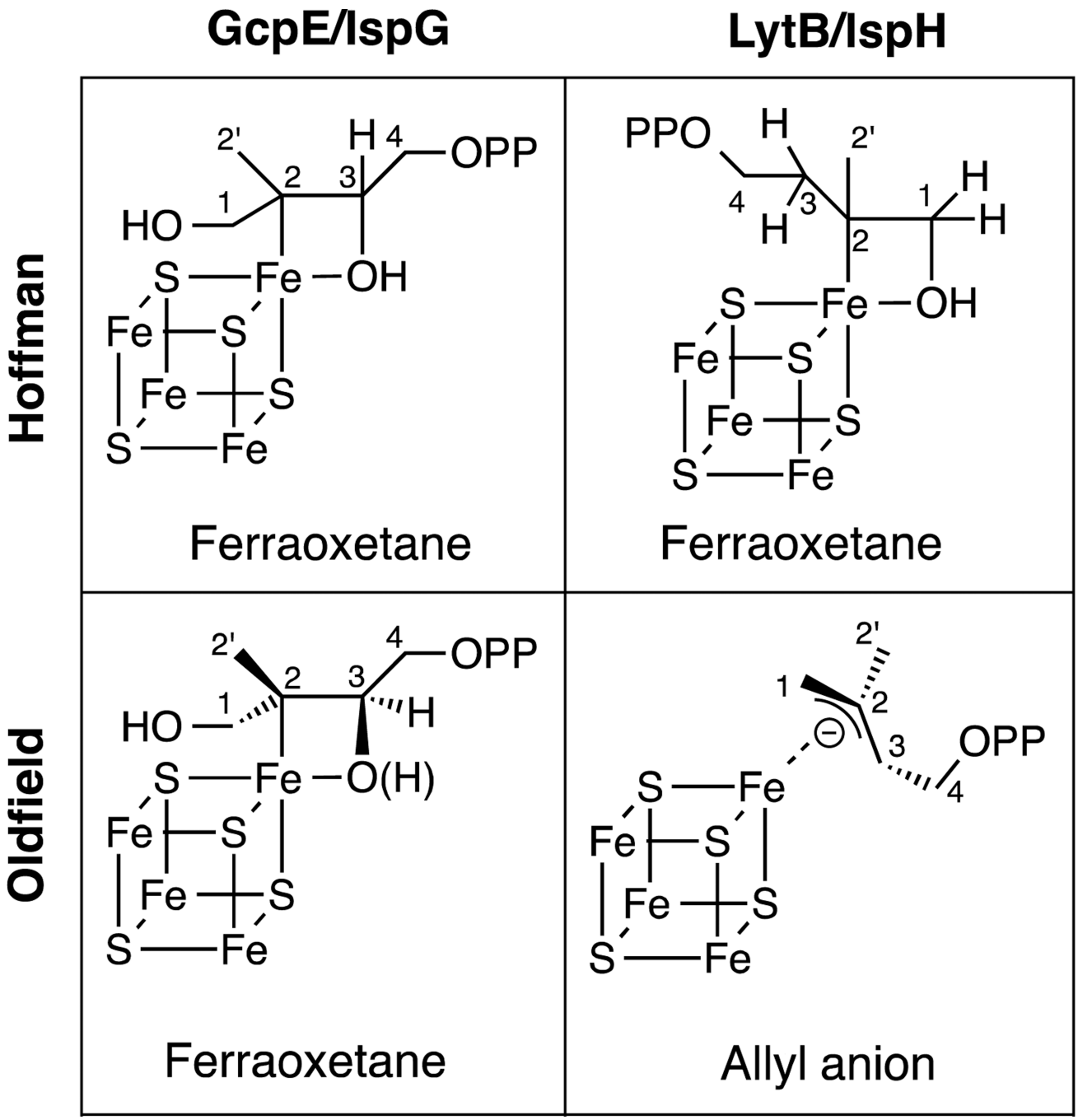

Figure 28.

Proposed intermediate structures of GcpE/IspG (left) and LytB/IspH (right) by Duin and coworkers (top) [210, 214] and Oldfield and coworkers (bottom) [209, 215, 216]. Atom numbering follows that of MEcPP substrate for consistency.